Probing of Dark Energy Properties in the Universe Using Astrophysical Observations

Vanessa Stephanie Emilia Smer Barreto

Doctor of Philosophy
The University of Edinburgh
June 2017

Abstract

The astrophysical data of the last two decades have allowed cosmologists to conclude that the present Universe is accelerating. The research carried out to find the origin of this phenomenon has led to the creation of a vast number of dark energy and modified gravity theories, of which the simplest is the ΛCDM model. The latter is, however, plagued with very difficult problems awaiting a solution. The work here presented seeks to contribute to the discussion of the possible explanation for the Cosmos' acceleration and other important questions in modern cosmology using the newest astrophysical observations available.

This thesis starts by exploring a dark energy model dubbed thawing quintessence which is characterised by allowing a non constant ratio of pressure to density for dark energy that is however still close to -1 for most of the cosmological evolution, shifting away from this value when the domination of the radiation and matter components fades away. The findings are the most up-to-date constraints for which this model gives a viable theory for dark energy, including a bound on the equation of state at present of $w < -0.88$. This exact approach was contrasted with the use of an approximate equation-of-state parametrisation for thawing theories. The analysis also includes different parametrisation choices, and comments on the accuracy of the constraints imposed by CMB anisotropies alone.

Next, the cosmology of hybrid metric-Palatini gravity is presented. This is a type of Modified Gravity theory in which the Lagrangian density for the gravitational action is a function of the Ricci scalars of both the connection and the metric. The background evolution of two models of this kind is examined explicitly showing the recovery of standard General Relativity at late times. The maximum deviation from the gravitational constant G at early times is constrained using a combination of geometrical data, finding it to be around 1%.

A designer scenario, also introduced under the hybrid metric-Palatini formulation, is then used to explore to what extent early modifications of gravity, which become significant after recombination but then decay towards the present, can be constrained by current and future cosmological observations. This model is embedded in the effective field theory description of Horndeski scalar-tensor gravity with an early-time decoupling of the gravitational modification.

Applying cosmological data, the constraints on the early-time deviations from General Relativity are obtained. These are dependent on the redshift at which the oscillations in the slip between the gravitational potentials are turned on. For $z_{\rm on} = 1000$, the deviation from Einstein's theory is $\leq 10^{-2}$ with 95% confidence. An explanation of the effect that these divergences have on the CMB power spectrum are discussed, as well as the effect that future 21 cm survey data will have on this study.

The last part of this work is a move towards inflation, the early epoch of accelerated expansion undergone by the Universe. Here a parametrisation of the acceleration trajectory is investigated with the aim of measuring the rolling of the inflaton corresponding to the value of the tensor-to-scalar ratio r to be compared with future observations.

Considering five $\ln \epsilon$ amplitudes and 14 e-foldings, it was found that the posterior distribution of $(r,\Delta\Phi)$ is in very good agreement with Lyth's bound. The analysis included a histogram depiction of the latter result, from which later a minimum constraint on $\Delta\phi$ for each of the bins was found. These outcomes constitute the intermediate step of this project which will be made more accurate by extending it to ~ 50 e-folds, a larger set of cosmological parameters and observational bounds that are restrictive on small scales.

Declaration

I declare that this thesis was composed by myself, that the work contained herein is my own except where explicitly stated otherwise in the text, and that this work has not been submitted for any other degree or professional qualification except as specified.

Parts of this work have been published in [137].

Parts of this work have been published in [139].

Parts of this work have been published in [205].

(*Vanessa Stephanie Emilia Smer Barreto, June 2017*)

To Jimena, Jessel Adriana and Luis Fernando

Acknowledgements

Dad, thank you for supporting my scientific aspirations from the very start. From that time when I was seven and you took me to meet the biologists at your university, to all the advice you have given me in the last few months. I could not have done it without you. I love you.

Mum, thank you for the trust you put in me, and for supporting my decision to go and to study far from home, even when you knew it would be very hard. I think about you and the rest of the family constantly. Thanks for understanding this is what I wanted to do. I love you too!

Andrew, thank you for your mentorship and for betting on me. Your openness to people, incisiveness in physics and wicked sense of humour are just some of the qualities I most admire in you. Thanks to you I have had the chance to be part of two wonderful scientific communities, which is of course the main reason these acknowledgements are so long.

Fermín, Vero, Sergio, Lucía, and the rest of my uncles and cousins, I could not ask for more supportive relatives. I send each of you a big hug. Nelson, I have had the good fortune of studying my PhD at your side, and of learning so much from you, but must importantly, of developing our friendship. Your dedication to science is a constant inspiration.

Chris, your support in the last months has been invaluable to the completion of this thesis. What is more, you were one of the first friends I made in the UK, for which I count myself lucky. I have a deep admiration for your interest in and acceptance of people from all cultures.

Sam, thanks for being my friend, collaborating with you has been one of the most fun experiences of the PhD. Agnes, I have learnt more physics from our meetings than in all PhD conferences put together. You are just wonderful.

Gemma, Toñito, Casandra, Erika, Emyr, Tali, Raúl, Luis, Alberto, thank you for letting me join the warmest Latin community south of the Scottish Borders, I hope we share many experiences together in the rest of our lives.

Alastair, you are the funniest, kindest officemate anyone could wish for, I will miss you terribly. I hope that outreach job turns up soon because you deserve it. David, Mike, Sheggy, Marco, Cass, Sam, Joey, thank you for being such a supportive group of officemates. I do apologise for keeping the office heating at temperatures more appropriate for the Caribbean than Edinburgh.

Cass, Nat, Rafita, Pau, Delia, Felix, Dany, Jorge, the time spent with you are some of the happiest memories I have of the last three years. I hope we have many more delicious meals together and shared moments in the future to come.

Julio, Genaro, Ricardo, Luis, Ulises, thank you so much for supporting my first steps towards doing research in physics. Your own academic careers and advice were an inspiration, example and point of reference for me every step of the way.

Roger and Einan, thank you for your open advice, and for giving me the opportunity to express myself without judging. Paula, Sadegh, Ken, Andy, Jim, Anette, John, Catherine, Andy, in various different ways, your support was crucial to getting this PhD done. Thank you very much!

Roushan and Lindsay, I owe you more than I can express and have a deep respect for what you do. Alex, Rachel, Clémence, Maria, Johanna and Sheggy, thank you for your constant support and for being such a fun bunch.

Lucas and Shaun, I have huge respect for you and for your ideas. I am so grateful for the chance to collaborate with you. Emma, Paty, Brenda, thank you for your support and friendship over all these years. Marina, Marika, Esther, Anna Lisa and Ami, thank you for sharing with me your experiences and honest advice.

Mary, there are not enough words to express the gratitude I feel to you for these last three years. Thank you, and Lucy, for sharing your home (which is so precious) and food (which is so delicious) so generously with me. I hope we can do the same for you one day.

Jo, thank you for reading this thesis so carefully and for being as kind as you are, in particular for always putting lemons by my plate. And to both you and David, thank you for receiving me into your lovely family.

Patrick, how can I do justice to your love, your time, and your patience. This thesis and many more, I owe to you, because without you I would have gone as far as page 43. You are my partner, with whom I wish to share my life. Thank you for being happy when the codes ran, and for raising my morale when papers got rejected, but more so for being by my side no matter what. I love you!

I want to thank CONACyT for funding this PhD so punctually for the whole of its duration.

Contents

Abstract i

Declaration iii

Acknowledgements v

Contents vii

List of Figures xii

List of Tables xvi

1 Introduction 1

- 1.1 The standard model of cosmology 4
- 1.2 Problems with the standard cosmological model 11
  - 1.2.1 The flatness problem 11
  - 1.2.2 The horizon problem 11
  - 1.2.3 The unwanted relics problem 11
  - 1.2.4 Cosmic coincidence problem 12
  - 1.2.5 Cosmological constant problem 12
- 1.3 The theory of cosmological inflation 14
  - 1.3.1 How inflation solves the flatness, horizon and relic problems 15

1.3.2 Single-field inflation 16

1.4 Modified Matter (MM) and Modified Gravity (MG) 18

1.4.1 Specifying the energy-momentum tensor $T_{\mu\nu}$ 19

1.4.2 Specifying the Einstein tensor $G_{\mu\nu}$ 20

1.4.3 Screening mechanisms 24

1.4.4 Theoretically consistent models of MM/MG 26

1.5 Cosmological perturbation theory 28

1.6 The matter power spectrum 29

1.7 The Markov Chain Monte Carlo method and Bayesian Statistics 31

1.7.1 Bayes' theorem 31

1.7.2 Marginal probability 32

1.7.3 Computational tools and MCMC 32

1.7.4 Burn-in 33

1.7.5 Thinning 34

1.7.6 Parameter estimation 34

1.7.7 Alternatives to MCMC sampling 36

1.8 Cosmological observables 37

1.8.1 SNe Ia luminosity–redshift relation 37

1.8.2 Baryon Acoustic Oscillations (BAO) peak 38

1.8.3 Cosmic Microwave Background (CMB) 40

1.9 Exploring the cosmological parameter space 42

1.10 Outline of chapters 2-6 44

2 *Planck* Satellite Constraints on Pseudo-Nambu–Goldstone Boson Quintessence 46

2.1 Introduction 46

2.2 The cosmology of quintessence 47

  2.2.1 Tracking freezing models 50

  2.2.2 Scaling freezing models 53

  2.2.3 Thawing models 53

2.3 PNGB quintessence 54

  2.3.1 PNGB potential analysis with COSMOMC 56

  2.3.2 Constraints 57

  2.3.3 Thawing quintessence: equation of state parametrisation 61

  2.3.4 Constraints using *Planck* 2015 only 63

  2.3.5 Choice of inverse prior for the PNGB potential width 65

  2.3.6 Comparison with previous results 67

2.4 Conclusions 69

3 Constraints on hybrid metric-Palatini gravity from background evolution 71

3.1 Introduction 71

3.2 Cosmology in the hybrid metric-Palatini gravity 73

  3.2.1 Scalar-tensor representation 75

3.3 Models of hybrid metric-Palatini gravity 77

  3.3.1 The exponential model 78

  3.3.2 The quadratic model 81

3.4 Background Observables ... 82

3.4.1 Observables ... 83

3.4.2 Metropolis - Hastings Algorithm ... 84

3.4.3 Priors ... 85

3.4.4 Constraints ... 86

3.5 Conclusion ... 90

4 Constraints on decaying early modified gravity from cosmological observations 92

4.1 Introduction ... 92

4.2 Designer $f(\mathcal{R})$ Model ... 94

4.3 Linear Perturbations in $f(\mathcal{R})$ Gravity ... 96

4.3.1 Subhorizon Approximation ... 97

4.3.2 Early–Time Corrections ... 100

4.3.3 Embedding in Horndeski Gravity and Effective Field Theory ... 104

4.4 Implementation in MGCAMB ... 106

4.5 Cosmological Observables ... 108

4.5.1 Geometric Probes ... 108

4.5.2 Cosmic Microwave Background ... 109

4.6 Cosmological Constraints ... 111

4.6.1 Datasets ... 111

4.6.2 Constraints ... 112

4.6.3 Outlook: 21 cm and Gravitational Waves ... 113

4.7 Conclusions ... 114

5 Constraints on the field-roll during inflation 116

5.1 Introduction 116

5.2 The shape of the acceleration during the inflationary epoch 119

5.3 The acceleration sampling 121

5.4 Cosmological Constraints 125

5.4.1 Datasets 125

5.4.2 Acceleration trajectories 126

5.4.3 The rolling of the scalar field $\Delta\phi$ 129

5.5 Discussion 131

5.6 Conclusions 132

6 Conclusions 134

Bibliography 140

List of Figures

1.1 The cosmic microwave background through the lens of the COBE, WMAP and *Planck* satellites. Image credit: NASA/JPL-Caltech/ESA. 4

1.2 The Hubble diagram for Jha's compilation of observed type Ia supernovae [110]. The scatter about the line corresponds to statistical distance errors of < 10 per object. The small red region in the lower left marks the span of Hubble's original Hubble diagram from 1929. 5

1.3 *Planck* 2015 CMB spectra, compared with the base CDM fit to PlanckTT+lowP data (red line) [11]. Image credit: Planck Science Team. 41

2.1 The quintessence equation of state w versus a for the potential $M^5\phi^{-1}$ to second (blue) and third (red) order of Eq. (2.27). 52

2.2 The quintessence equation of state w versus a for $\lambda_1 = 9$, $\lambda_2 = 0.9$. Each curve corresponds to: (a) $a_\mathrm{t} = 0.23$, $\tau = 0.33$; (b) $a_\mathrm{t} = 0.17$, $\tau = 0.33$; (c) $a_\mathrm{t} = 0.15$, $\tau = 0.32$. 54

2.3 Equation of state versus scale factor for the PNGB potential with $f = 1.4M_\mathrm{Pl}$, for models leading to present values $w_0 = -0.99$ (red), $w_0 = -0.93$ (blue) and $w_0 = -0.6$ (green). In thawing quintessence, $w \geq -1$. 55

2.4 Density plots for the equation of state w versus scale factor a of the PNGB model. The figure on the left depicts random prior choices from Table 2.1. On the right, a sample of the posterior distribution models obtained from the combined JLA + BAO + HST + *Planck* 2015 datasets is shown. The best-fit model is drawn in red, and a zoom is included to show the detail of the posterior trajectories given their closeness on the original axis range. 59

2.5 2D contours of the combined JLA + BAO + HST + *Planck* 2015 constraints for the PNGB model with potential Eq. (2.30). The individual marginalised posterior probability distributions of each parameter are also shown. 60

2.6 Equation of state versus scale factor for the quintessence field equation of state (solid lines) and Eq. (2.37) (dashed lines) with $\Omega_\phi = 0.68$. The parameter values in each case are (a) $f/M_{\rm Pl} = 2$, $\phi_{\rm i}/f = 1.65$, $K = 0.98$, $w_0 = -0.95$; (b) $f/M_{\rm Pl} = 1.1$, $\phi_{\rm i}/f = 1.52$, $K = 1.02$, $w_0 = -0.84$; (c) $f/M_{\rm Pl} = 0.9$, $\phi_{\rm i}/f = 1.43$, $K = 1.09$, $w_0 = -0.77$; (d) $f/M_{\rm Pl} = 0.5$, $\phi_{\rm i}/f = 0.94$, $K = 1.72$, $w_0 = -0.34$. 62

2.7 The 68% and 95% confidence level regions for (w_0, K) given by Eq. (2.38). 64

2.8 The 2D contours of the *Planck*-only constraints for the PNGB model with potential Eq. (2.30). 65

2.9 The 2D contours of the combined JLA + BAO + HST + *Planck* 2015 constraints for the PNGB model with potential Eq. (2.30) and parametrisation uniform in $M_{\rm Pl}/f$ instead of $f/M_{\rm Pl}$. The rest of the parameter definitions are the same as in Fig. 2.5. 67

3.1 The background evolution predicted by the exponential $f(\mathcal{R})$ model compared to ΛCDM. $\mathcal{R}$ is plotted far into the future ($z \to -1$), to explicitly show that this solution asymptotically tends to the minimum of the potential, $V(\mathcal{R})$, which is also displayed. The deceleration parameter q is also shown. The present-day matter energy density is set to be $\Omega_{\rm m} = 0.30$, and $\mathcal{R}_\star = 1$ is in units of H_0^2. 80

3.2 The same as Fig. 3.1 for the quadratic $f(\mathcal{R})$ model. The matter density parameter has been fixed to $\Omega_{\rm m} = 0.30$. 82

3.3 The 2-d contours of the combined constraints from the background surveys considered for the exponential $f(\mathcal{R})$ model with $f_{\mathcal{R}}(z_{\rm i})$ fixed to 10^{-4}. The individual marginalised posterior probability distributions of each parameter is also plotted. 86

3.4 The 2-d contours of the combined constraints from the background surveys considered for the exponential $f(\mathcal{R})$ model by considering a prior range for $f_{\mathcal{R}}(z_{\rm i})$ between $[1 \times 10^{-6}, 0.1]$. The individual marginalised posterior probability distributions of each parameter is also plotted. 88

3.5 Similar as Figs. 3.3 and 3.4 for the quadratic $f(\mathcal{R})$ model. 89

4.1 Evolution of the absolute value of the additional scalar degree of freedom introduced in $f(\mathcal{R})$ theories, $f_\mathcal{R}$, as a function of the scale factor, a, with $z_\mathrm{i} = 1000$. The density parameter has been fixed to $\Omega_\mathrm{m} = 0.30$. 95

4.2 Relative difference $|\gamma_\mathrm{num} - \gamma_\mathrm{QS}|/\gamma_\mathrm{num}$ between the numerical ratio $\gamma \equiv \Phi/\Psi$ and its quasistatic (QS) approximation given by Eq. (4.14). The redshift considered was $z_\mathrm{i} = 1000$ and the matter density parameter was fixed to $\Omega_\mathrm{m} = 0.30$. 98

4.3 The top panels show the numerical evolution (solid lines) of the perturbation $\delta f_\mathcal{R}$ against the evolution predicted by the analytical approximation (dashed lines) given by Eq. (4.16). The two largest scales have been enhanced by a factor of 100 and 1000 to be noticeable. The bottom panels show the absolute difference between the analytical approximation and the numerical results. The matter density parameter was fixed to $\Omega_\mathrm{m} = 0.30$. 102

4.4 Relative difference between the numerical evolution of $\gamma \equiv \Phi/\Psi$ and the approximation in Eq. (4.32). The top panel shows $|f_{\mathcal{R}\mathrm{i}}| = 10^{-4}$ and the lower panel shows $|f_{\mathcal{R}\mathrm{i}}| = 10^{-2}$. Once more, the matter density parameter was fixed to $\Omega_\mathrm{M} = 0.30$. 107

4.5 The lensed CMB temperature anisotropy power spectrum predicted by the designer hybrid metric-Palatini model for $|f_\mathcal{R}(z_\mathrm{i})| = 5 \times 10^{-2}$ and different values of z_on as well as the prediction for the ΛCDM model (top panel). The lower panel shows the difference to ΛCDM, $\Delta_\mathrm{rel} = \ell(\ell+1)\left(C_\ell^{TT,\mathrm{hybrid}} - C_\ell^{TT,\Lambda}\right)/(2\pi)$. 109

5.1 One-to-one correspondence between the wavenumber k required by CAMB and the e-fold N where each of the amplitudes $\ln\epsilon_\mathrm{i}$ is positioned for the best-fit model found in the MCMC sampling presented in Section 5.4. The approximate positions of the multipoles plus the pivot scales for *Planck* and WMAP are also labelled. 122

5.2 Density plots for a random sample of the prior distribution of $(\delta_1, \delta_2, \epsilon_3, \delta_4, \delta_5)$ on the left. Similar plot with chosen values of the posterior distribution on the right. The best fit $\ln\epsilon_\mathrm{i} = (-7.90, -7.80, -7.91, -7.82, -8.07)$ are depicted in red points. 125

5.3 1D marginalised posterior distributions for the baseline cosmological and derived parameters with priors given in Table 5.1 for data combination *Planck* + BAO. 126

5.4 The 68% and 95% 2D confidence contours depicting the $(\delta_1, \delta_2, \epsilon_3, \delta_4, \delta_5)$ parameter definitions analysed directly from the GETDIST software chains. 127

5.5 The 2D contours of the splined points $\ln \epsilon_{\mathrm{i}}$ as re-defined by Eqs. (5.17) taken from the original values in Fig. 5.4. 128

5.6 The 68% and 95% confidence contour for the tensor-to-scalar ratio r and the rolling of the scalar field $\Delta\phi$ for the same models as in Fig. 5.4. 129

5.7 Histogram representation of the relationship between the tensor-to-scalar ratio r and the rolling of the scalar field $\Delta\phi$ from the smallest to the largest values obtained in the posterior distribution. 130

5.8 The minimum (r,$\Delta\phi$) for each of the 8 bins described in Fig. 5.7. The blue line is the Lyth bound prediction Eq. (5.5). This is the chapter's main result. 132

List of Tables

2.1 Prior ranges for cosmological and PNGB model parameters, the prior being uniform in the parameter quoted. The meaning of the cosmological parameters is as in the *Planck* collaboration papers [8, 11]. The final three parameters listed are derived from the others and inherit non-uniform priors from their relation to them. 58

3.1 Inverse covariance matrix for the distance information obtained from Planck in the ΛCDM framework. 83

4.1 Current constraints (95% C.L.) on $f_{\mathcal{R}}(z_{\rm i} = 1000)$ from the combination of surveys discussed in Sec. 4.6.1. Note that models with a positive sign of $f_{\mathcal{R}}$ suffer from a ghost instability (see Sec. 4.3.3) and models with $z_{\rm on} = 100$ cannot be constrained within the prior $|f_{\mathcal{R}\rm i}| < 0.1$ required for the viability of the approximations performed in Sec. 4.3.2. However, a constraint of $|f_{\mathcal{R}\rm i}| \lesssim 10^{-3}$ on all models will be achievable with 21 cm intensity mapping (see Sec. 4.6.3). We also present constraints on the value of $f_{\mathcal{R}}$ at the redshift of decoupling, $z_{\rm on}$, and at the present time, $z = 0$. 112

5.1 Prior ranges for amplitudes $\ln \epsilon_{\rm i}$ and baseline parameters. The meaning of the cosmological parameters is as in the *Planck* collaboration papers [8, 11]. The final four parameters listed are derived from the others. 124

Chapter 1

Introduction

In 1915, Einstein's theory of General Relativity (GR) laid down the basis for building a descriptive model for the large-scale Universe. In the decades to follow, the Cosmos's history, from its earliest breath up to the present time, has been studied, and hotly debated.

In 1917, Einstein introduced the idea of a static Universe, the first application of his theory to cosmology. In the same year, de Sitter presented the first dynamical model [202]. Alexander Friedmann originated the general isotropic solution in his papers "On the curvature of space" [83] in 1922, and "On the possibility of a world with constant negative curvature of space" in 1924, where he introduced the idea of negative curvature [84]. Five year later, Edwin Hubble proved Friedmann's prediction of an expanding Universe to be certain. Georges Lemaître, Howard Robertson and Arthur Walker also made very important contributions to this problem.

By the late 1940s, Ralph Alpher and Robert Herman had improved upon Friedmann's work by predicting the existence of a blackbody radiation [14], formed in the very early Universe, when matter and photons existed at a very high energetic state. This primeval effect was to be measured at a temperature of a few Kelvin, given that the energy density components of the Universe cool down as the Universe grows. As often happens in science, this young imprint was discovered by accident in 1965, and given the name of the Cosmic Microwave Background (CMB) Radiation. With this discovery, Arno Penzias and Robert Wilson of the Bell Telephone laboratories provided the most compelling evidence for the Big Bang theory [172].

By this point, Friedmann's model had been established as a highly successful theory, but it still suffered from severe shortcomings. For instance, the question of how the Universe came to be remained unanswered. This problem was partially resolved by inflation, a theory postulated by several authors at the same time in the early 1980s [94, 118, 191, 210].

In 1989, the technology and budget of NASA's Goddard Space Flight Center allowed the launching of the Cosmic Background Explorer (COBE) satellite, a more sophisticated version of Penzias and Wilson's horn antenna, with the purpose of measuring the microwave sky on large angular scales. It was revealed that our Universe, although highly homogeneous and isotropic, has tiny (10^{-5}) temperature anisotropies in the matter distribution. These differences were responsible for the formation of stars, galaxies, clusters, and all large-scale structures known. It is theorised that the origin of these anisotropies are the quantum fluctuations of fundamental fields, which were present in the very early Cosmos [161].

More recently, in 1998, the High-redshift Supernova Search team and the Supernova Cosmology Team, led by Adam Riess [183] and Saul Perlmutter [175] respectively, collected distances for 51 Supernovae Type Ia (SN Ia). At the time this was the largest dataset of its kind. Their analyses concluded that the Universe is undergoing an epoch of accelerated expansion. The name given to the unknown source of this accelerated expansion is Dark Energy (DE).

The findings of surveys carried out after COBE have supported the existence of a cosmological model described by the Big Bang, and complemented by inflation and dark energy. Beginning in 2003, the Wilkinson Microwave Anisotropy Probe (WMAP) provided several releases with ever more accurate measurements of the CMB anisotropies [27, 127, 128, 208, 209], followed by the unprecedented sensitivity and angular resolution of the *Planck* mission [7, 8].

With the information available from these experiments, it is possible to establish a time line of the most important events in the Universe's history. This is:

When our Universe was less than a second old, it underwent a period of accelerated expansion known as inflation. This was followed by an era of attractive gravity, first dominated by radiation, during which helium and deuterium formed. Given the fast redshift rate of the energy density of radiation, this epoch was shortly lived and followed by a matter-dominated era around the redshift $z \simeq 3000$.

The temperature anisotropies measured by COBE happened on the last scattering surface at which electrons were trapped by hydrogen nuclei to form atoms. The photons could then move freely without experiencing Thomson scattering. This decoupling time corresponds to the redshift $z \approx 1090$. According to *Planck* 2015 data [8], the energy density components of the Universe were distributed at this time as

Dark matter - 63.92 %
Radiation from photons - 14.16 %
Radiation from neutrinos - 9.90 %
Baryons - 12.00 %
Dark energy - 1.3146 x 10^{-7} %

During this time, galaxies and clusters started to form. To some extent, baryons also contributed to large-scale structure formation. Compared to DM, the energy density of DE was suppressed to allow the large-scale structure to grow enough [16].

However, the DE energy density eventually caught up with the one from DM. The onset of cosmic acceleration occurred around the redshift $z \approx 1$, ending the long period of gravitational attraction in the Universe. There is a second era in which gravity is effectively repulsive now taking place, as dark energy has started to dominate. Now, at redshift $z = 0$, the most recent *Planck* release [8] tells us the energy distribution of the Universe is

Dark matter - 25.89 %
Radiation from photons - 0.00526 %
Radiation from neutrinos - 0.00367 %
Baryons - 4.86 %
Dark energy - 69.11 %

Understanding the true nature of DE is one of the most interesting problems in cosmology, as this component will shape the future of our Universe.

Theories whose purpose is to contribute to the discussion of the inflationary era and the dark energy domination period, are the focus of this thesis.

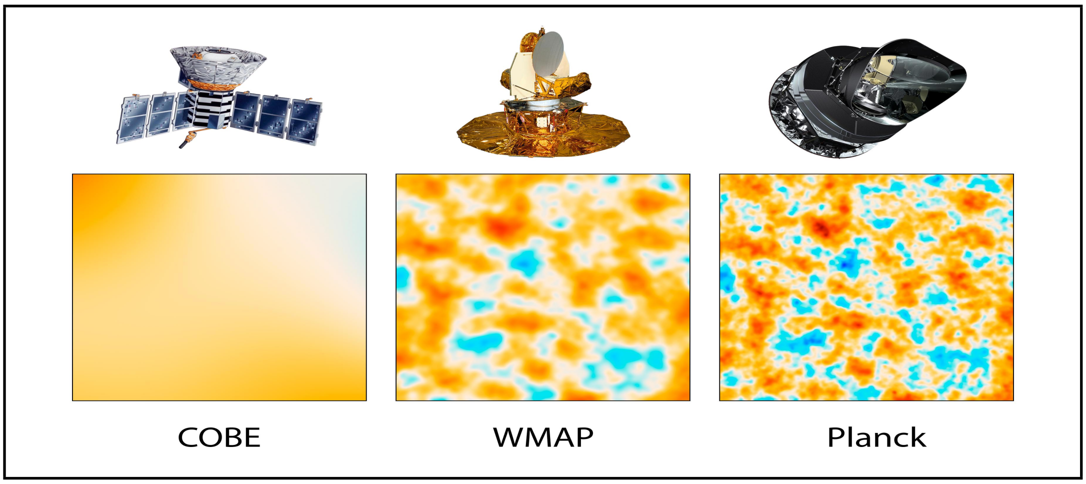

Figure 1.1 *The cosmic microwave background through the lens of the COBE, WMAP and Planck satellites. Image credit: NASA/JPL-Caltech/ESA.*

1.1 The standard model of cosmology

The most fundamental assumption made in cosmology is the Copernican principle:[1]

The large-scale Universe is accurately modelled as spatially homogeneous and isotropic.

This principle is consistent with the early state of the Cosmos, as the CMB exhibits nearly perfect isotropy. Also, on scales of $\simeq$ 100 h^{-1}Mpc, the large-scale distribution of galaxies is very smooth [131, 196, 226]. Figure. 1.1 is a representation of the sensitivity achieved by each generation of satellites in the quest to map the cosmic radiation.

Describing the latest billion years under the Copernican assumption is more of a challenge, as galaxies, voids, and clusters make the late Universe very lumpy on small scales. Because of this observation, it is useful to divide the study of cosmological models between the background, which is exactly homogeneous and isotropic (also called the Friedmann-Robertson-Walker model), and a more realistic description of the effect of small perturbations.

Distance definitions are very important for the study of cosmology. To parametrise the evolution of the Universe, it is useful to introduce the **scale**

---

[1] Throughout this work natural units will be used, such as speed of light $c = 1$.

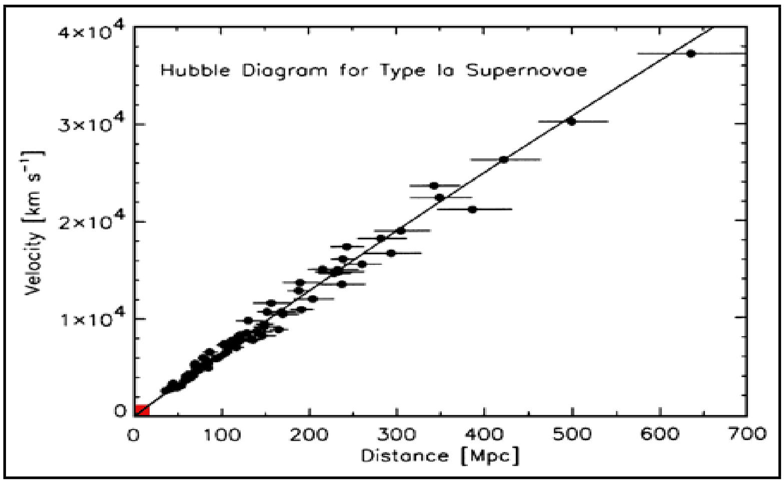

Figure 1.2 *The Hubble diagram for Jha's compilation of observed type Ia supernovae [110]. The scatter about the line corresponds to statistical distance errors of* < 10 *per object. The small red region in the lower left marks the span of Hubble's original Hubble diagram from 1929.*

factor a, which is set to one at present. A **comoving distance** r will measure the difference between coordinate points and it will therefore remain unchanged. On the other hand, the **physical distance** $d = ar$ is proportional to the scale factor, and evolves with time. It is also convenient to define the **conformal time** η, where $dt = ad\eta$. To quantify the change in scale factor and its relation to energy density the Hubble rate is defined [71],

$$H(t) = \frac{\dot{a}}{a}. \tag{1.1}$$

where an overdot represents a derivative with respect to time t. In an expanding Universe, it is therefore expected that galaxies are receding from us. The **Hubble time** H^{-1} and the **Hubble length** cH^{-1} are also important to interpret the Cosmos's evolution. In the case of light, when it is emitted from a receding object its wavelength stretches out, and the distortion is measured by a factor defined as redshift

$$1 + z \equiv \frac{\lambda_{\text{observed}}}{\lambda_{\text{emitted}}} \equiv \frac{1}{a}. \tag{1.2}$$

The observation that at low redshifts, velocity increases linearly with distance with a slope given by the Hubble rate was first made by Hubble in 1929 and it is known as Hubble's law [107]

$$v = H_0 d, \tag{1.3}$$

where H_0 is the present value of H, called the **Hubble constant**. In Fig. 1.2, the redshift scale of Hubble's original measurements is recognisable against a much more recent Supernova type Ia dataset. With these concepts, other distances can be considered in order to explore the different epochs in our Universe [155]:

Horizon is a frontier between events that are observable and those who are not. Two points separated by a distance larger than the horizon at a given time have not yet been able to reach thermal equilibrium or even interact.

Particle horizon is the distance that light could have travelled from the beginning of the Universe until a certain time t.

$$x_{\text{ph}} = \int_0^t \frac{dt}{a}. \tag{1.4}$$

Event horizon is the distance that light can travel from a certain time t into the future.

$$x_{\text{eh}} = \int_t^\infty \frac{dt}{a}. \tag{1.5}$$

Effective horizons are more realistic versions of the previous two definitions. Setting a_2 as the scale factor at the end of inflation, the effective event horizon

$$x_{\text{eh}} = \int_a^{a_2} \frac{da}{Ha^2}, \tag{1.6}$$

is the maximum distance that light can travel during this epoch. Setting a_1 as the scale factor at the start of the Big Bang, the effective particle horizon

$$x_{\text{ph}} = \int_{a_1}^{a} \frac{da}{Ha^2}, \tag{1.7}$$

is the maximum distance that light can have travelled during the Big Bang up to a given time.

For $\eta = 0$ at the beginning of the Big Bang, $\eta = x_{\text{ph}}(a_1, a)$. Its present value η_0 is the definition of the radius of the **observable Universe**.

From these fundamental definitions, it is possible to start describing the cosmological history in a quantitative manner. The spatially homogeneous and isotropic model is called the Friedmann-Lemaître-Robertson-Walker (FLRW or FRW) model, and it describes the background Universe with the line element

$$ds^2 = g_{\mu\nu} dx^\mu dx^\nu = dt^2 - a^2(t) \left[\frac{dr^2}{1 - Kr^2} + r^2 \left(d\theta^2 + \sin^2\theta d\phi^2 \right) \right], \tag{1.8}$$

where $g_{\mu\nu}$ is the metric tensor, $a(t)$ is the scale factor, that determines the overall scale of the Universe, t is the time, r is the comoving or coordinate distance, K is the spatial curvature, and θ and ϕ are spherical coordinates.

There are three possible values for the spatial curvature:

- Closed Universe: The finite-sized spatial sections are spheres and $K > 0$.
- Flat or critical Universe: The unbounded spatial sections are flat and $K = 0$.
- Open Universe: The unbounded spatial sections correspond to hyperboloids and $K < 0$.

The expansion history of the Universe can be described by the time dependence of the free function $a(t)$. The application of the FRW metric to the field equations of the standard cosmological model provides the evolution of the scale factor.

To derive such equations a relativistically invariant action needs to be provided. It is also desirable that such an expression be as simple as possible. To begin with, the volume element $d^{\mathrm{n}}x$ is to be transformed in an invariant manner. To arrive to the desirable transformation it is useful to consider the case of a diagonal metric (such as FLRW) where the line element takes the form

$$ds^2 = g_{11}(dx^1)^2 + g_{22}(dx^2)^2 + ... + g_{\mathrm{nn}}(dx^{\mathrm{n}})^2, \tag{1.9}$$

which is an orthogonal coordinate system. Consider an element of volume in the (x_1,x_2,x_3) surface defined by x^{a} constant for $a = 4, 5, ..., n$. The volume element is defined by the coordinate lengths dx^1, dx^2, dx^3. The proper lengths are $\sqrt{g_{11}}dx^2$, $\sqrt{g_{22}}dx^2$, $\sqrt{g_{33}}dx^3$. Thus the volume element is

$$d^3V = \sqrt{|g_{11}g_{22}g_{33}|}dx^1dx^2dx^3 \tag{1.10}$$

Similarly for an n-dimensional case,

$$d^{\mathrm{n}}V = \sqrt{|g_{11}g_{22}...g_{\mathrm{nn}}|}dx^1dx^2...dx^{\mathrm{n}} \tag{1.11}$$

Let's make a transformation to local Cartesian coordinates $x^{'\mathrm{a}}$ at an arbitrary point P in the manifold. A small n-dimensional region at P will have volume $d^{\mathrm{n}}V = dx^{'1}dx^{'2}...dx^{'\mathrm{n}}$. In any other coordinate system $x^{'\mathrm{a}}$, a volume element $d^{\mathrm{n}}x$

picks up a factor of the Jacobian under change of coordinates

$$dx^{'1}dx^{'2}...dx^{'\mathrm{n}} = \left|\frac{\delta x^{'\mathrm{a}}}{\delta x^{\mathrm{b}}}\right| dx^1dx^2...dx^{\mathrm{n}}. \tag{1.12}$$

Denoting the transformation matrix as $X = \frac{\delta x^{\mathrm{a}}}{\delta x^{'\mathrm{b}}}$ then the Jacobian is $J = \det(X^{-1}) = (\det X)^{-1}$. Now let's define the matrix $G = g_{\mathrm{ab}}(P)$ and $G^{'} = g^{'}_{\mathrm{ab}}(P)$ respectively, then

$$G^{'} = X^TGX. \tag{1.13}$$

Taking determinants on both sides of 1.13 and denoting $g^{'} = \det(G^{'})$ and $g = \det(G)$ then

$$g^{'} = \det(X^2)g = \frac{1}{J^2}g. \tag{1.14}$$

The coordinates $x^{'\mathrm{a}}$ are Cartesian, therefore $G^{'} = \mathrm{diag}(\pm1, \pm1, ... \pm 1)$ implying $g^{'} = \pm1$. Then $g = \pm J^2$ [51].

This invariant transformation of a volume element is a necessity when integrating scalar functions over a n-manifold,

$$I = \int \phi(x)\sqrt{|g|}d^nx \tag{1.15}$$

This brings us to the point where an action for general relativity can be introduced, where the dynamical variable is the metric $g_{\mu\nu}$. Hilbert figured that the simplest choice was the Einstein-Hilbert action [51]

$$\mathcal{S} = \frac{1}{2\kappa}\int d^4x\sqrt{-g}\left[R - 2\Lambda\right] + \int d^4x\sqrt{-g}\mathcal{L}_{\mathrm{M}}\left[g_{\mu\nu}, \Psi\right], \tag{1.16}$$

where $\kappa = 8\pi G$, g is the determinant of the metric tensor, G is the gravitational constant, R is the Ricci scalar, $R \equiv g^{\mu\nu}R_{\mu\nu}$, Λ is the cosmological constant and $\mathcal{L}_{\mathrm{M}}$ is the Lagrangian density of the matter fields Ψ.

The variation of Eq. (1.16) gives the field equations

$$G_{\mu\nu} \equiv R_{\mu\nu} - \frac{1}{2}g_{\mu\nu}R = 8\pi GT_{\mu\nu} + g_{\mu\nu}\Lambda, \tag{1.17}$$

where $G_{\mu\nu}$ is the Einstein tensor, given by a combination of the Ricci tensor

$R_{\mu\nu} = R^{\alpha}_{\mu\alpha\nu}$ and the Ricci scalar, and $T_{\mu\nu}$ is the stress-energy tensor

$$T_{\mu\nu} = \frac{-2}{\sqrt{-g}} \frac{\partial \mathcal{L}_{\mathrm{M}} \sqrt{-g}}{\partial g^{\mu\nu}}. \tag{1.18}$$

The l.h.s. of Eq. (1.17) characterises the geometry of spacetime, whereas the r.h.s. describes the energy and momentum components. Applying the FRW metric, the (00) and (ii) components of Eq. (1.17) give the cosmological field equations

$$H^2 = \left(\frac{\dot{a}}{a}\right)^2 = \frac{8\pi G\rho}{3} - \frac{K}{a^2}, \tag{1.19}$$

$$\frac{\ddot{a}}{a} = -\frac{4\pi G}{3}\left(\rho + 3P\right). \tag{1.20}$$

where H is the Hubble parameter, ρ is the energy density and P is the pressure.

A common way to express Eq. (1.19) is in terms of the density parameter $\Omega = \rho/\rho_{\mathrm{c}}$, where ρ_{c} is the critical density for which the Universe is flat ($K = 0$), defined as

$$\rho_{\mathrm{c}} = \frac{3H^2}{8\pi G}. \tag{1.21}$$

Expressing every matter density and the curvature parameter in terms of Ω, the Friedmann equation becomes

$$1 = \Omega_{\mathrm{r}} + \Omega_{\mathrm{M}} + \Omega_{\mathrm{DE}} + \Omega_{\mathrm{K}}, \tag{1.22}$$

where

$$\Omega_{\mathrm{r}} = \frac{8\pi G\rho_{\mathrm{r}}}{3H^2},\ \Omega_{\mathrm{M}} = \frac{8\pi G\rho_{\mathrm{M}}}{3H^2},\ \Omega_{\mathrm{DE}} = \frac{8\pi G\rho_{\mathrm{DE}}}{3H^2},\ \Omega_{\mathrm{K}} = \frac{-K}{aH^2}. \tag{1.23}$$

The Einstein tensor satisfies the Bianchi identities $\nabla_{\mu} G^{\mu}_{\nu} = 0$. It follows from Eq. (1.17) that $\nabla_{\mu} T^{\mu}_{\nu} = 0$. The time component of this expression is

$$\nabla_{\mu} T^{0}_{\nu} = \dot{\rho} + \Gamma^{\mathrm{i}}_{\mathrm{i}0}(\rho + P) = \dot{\rho} + 3\frac{\dot{a}}{a}(\rho + P) = 0. \tag{1.24}$$

This is called the conservation or continuity equation. The system of equations (1.19), (1.20) and (1.24) implies three unknown variables (a, ρ, P) for three expressions, but they are not linearly independent.

Equation (1.24) can be simply rewritten as $d(\rho a^3) = -P da^3$, which can be interpreted as the first law of thermodynamics, as ρa^3 is proportional to the total energy, and a^3 to the volume. For the simple equation of state $\mathrm{P} = w\rho$ with w constant the solutions for (1.19) and (1.24) are

$$\rho \propto a^{-3(1+w)}, \;\; a \propto (t - t_{\rm i})^{2/3(1+w)}, \tag{1.25}$$

where $t_{\rm i}$ is a constant. When each one of the solutions for the cosmological fluids is combined with the present measured values, the expansion history of the Universe can be determined. The densities are:

Radiation: From statistical mechanics we know this component has an equation of state $w = 1/3$. In this case then, the cosmic evolution during the radiation-dominated epoch is given by

$$\rho \propto a^{-4}, \;\; a \propto (t - t_{\rm i})^{1/2}. \tag{1.26}$$

After the inflationary period, radiation was the dominant component of the Universe, but matter took over quickly, as the radiation density decreases much more rapidly.

Non-relativistic matter: In cosmological scales, matter has negligible pressure, so $w \sim 0$. Then, in this era, the evolution goes as

$$\rho \propto a^{-3}, \;\; a \propto (t - t_{\rm i})^{2/3}. \tag{1.27}$$

Dark energy: In order to produce cosmic acceleration we require $\ddot{a} > 0$ in Eq. (1.19)

$$P < -\frac{\rho}{3} \rightarrow w < -1/3, \tag{1.28}$$

where ρ is assumed positive. When $w = -1$, i.e., $P = -\rho$, it follows from Eq. (1.25) that ρ is a constant. This case corresponds to the cosmological constant, usually called “Λ”. For such a model, the scale factor evolves as $a \sim \exp{(Ht)}$.

The standard model of cosmology is known by the acronym ΛCDM (dark energy in the form of a cosmological constant plus cold dark matter). This theory is the most favoured in modern cosmology, because of its simplicity and its capability of fitting the data very well. [8].

It is important to note that this model is solely constructed on the general relativity formalism, and that Einstein’s theory represents the most general description of a single metric that in four dimensions has field equations with, at most, second order derivatives [60].

1.2 Problems with the standard cosmological model

The conclusions drawn from observational sources clash with the ΛCDM theoretical predictions in different ways. There are five problems which motivate the search for a better cosmological theory.

1.2.1 The flatness problem

The Friedmann equation rewritten with the density parameter Ω as in (1.22), dictates the spatial curvature of the Universe, which according to the observations, is flat. This means the Cosmos will forever remain with null curvature. During the radiation and matter domination epochs, Ω moved away from 1. However, at present, it is observed that this parameter is extremely close to unity, which implies that at very early times (1 s old), it should have been like that as well. But this very fined tuned initial condition is statistically highly unlikely.

1.2.2 The horizon problem

Regressing back in time during the Big Bang, the comoving horizon $1/aH$ becomes every time smaller in comparison to the comoving size of the observable Universe. This means that at early times, the observable Universe was much larger than the particle horizon. However, the CMB tells us the Universe at 300,000 years of age was incredible homogeneous and isotropic. The horizon problem consists of answering how this observation can be possible, when regions too distant from one another in the sky were, supposedly, not in causal contact.

1.2.3 The unwanted relics problem

This issue stems from the fact that many Grand Unified Theories (GUTs) predict the existence of stable exotic particles and topological defects that would have theoretically formed when the Universe was very young and under hot and highly energetic conditions. Such particles would have been produced in great abundance and would persist until today. However, all searches for these early time relics have resulted in failure.

1.2.4 Cosmic coincidence problem

The present dark energy density ($\Omega_{\rm DE} \simeq 0.69$) and the present dark matter density ($\Omega_{\rm DM} \simeq 0.26$) are of the same order of magnitude at the recent epoch. Nonetheless, in the past, their values have been extremely different and, if the measurements of the cosmological constant are true, they will become very different in the future as well. Why at this precise point are these values so similar? This question remains without a satisfactory answer.

1.2.5 Cosmological constant problem

For the cosmological constant to cause the cosmic acceleration observed today, Λ must be of the same order of magnitude as the square of the Hubble parameter at present H_0, i.e., $\Lambda \sim H_0^2 \sim (10^{-42})^2$. This means that the energy density for Λ is

$$\rho_\Lambda = \frac{\Lambda M_{\rm Pl}^2}{8\pi} \sim 10^{-47} {\rm GeV}^4. \tag{1.29}$$

where $M_{\rm Pl} \equiv 1/\sqrt{8\pi G}$ is the reduced Planck mass.

On the other side, if one interprets the origin of the energy density (1.29) to be the vacuum energy of empty space, its value can be predicted from quantum field theory (QFT). The zero point vacuum energy density $\langle 0|\hat{\rho}_{\rm vac}|0\rangle$ obtained by evaluation of the sum of zero-point energies of quantum fields with mass m is given by [126]

$$\langle 0|\hat{\rho}_{\rm vac}|0\rangle = \frac{1}{2}\int \frac{d^3k}{8\pi^3}\sqrt{k^2+m^2}, \tag{1.30}$$

It is well known from observations that the quantum vacuum is Lorentz invariant. Hence, this vacuum energy density must give rise to a stress-energy tensor in Minkowski space time of the form

$$\langle 0|\delta \hat{T}^{\rm vac}_{\mu\mu}|0\rangle = -\langle 0|\hat{\rho}_{\rm vac}|0\rangle \tag{1.31}$$

The expression in Eq. (1.30) is divergent, therefore, a UV cutoff $\Lambda_{\rm UV}$ is introduced to evaluate this integral

$$\begin{aligned}
\langle 0|\hat{\rho}_{\rm vac}|0\rangle &= \frac{1}{2}\int_0^{\Lambda_{\rm UV}} \frac{d^3k}{8\pi^3}\sqrt{k^2+m^2} \\
&= \frac{\Lambda_{\rm UV}^4}{16\pi^2} + \frac{m^2\Lambda_{\rm UV}^2}{16\pi^2} + \frac{m^4}{64\pi^2}\log\frac{m^2\sqrt{e}}{4\Lambda_{\rm UV}^2} + \mathcal{O}(\Lambda_{\rm UV}^{-1}), \qquad (1.32)
\end{aligned}$$

where the integral of the first line is evaluated exactly and only the leading order behavior is considered. The pressure arising from the vacuum contribution is

$$\begin{aligned}
\langle 0|\hat{P}_{\rm vac}|0\rangle &= \frac{1}{3}\int_0^{\Lambda_{\rm UV}} dk\frac{k^2}{4\pi^2}\frac{k^2}{\sqrt{k^2+m^2}} \\
&= \frac{\Lambda_{\rm UV}^4}{48\pi^2} - \frac{m^2\Lambda_{\rm UV}^2}{48\pi^2} - \frac{m^4}{64\pi^2}\log\left[\frac{m^2 e^{7/6}}{4\Lambda_{\rm UV}^2}\right] + \mathcal{O}(\Lambda_{\rm UV}^{-1}), \qquad (1.33)
\end{aligned}$$

The first two terms in both (1.32) and (1.33) break Lorentz invariance and are therefore unphysical. These can be removed by local counter terms. The final, physical result is obtained by sending $\Lambda_{\rm UV} \to \infty$, and absorbing the remaining numerical factors in the logarithm to find

$$\langle 0|\hat{\rho}_{\rm vac}^{\rm ren}|0\rangle = -\langle 0|\hat{P}_{\rm vac}^{\rm ren}|0\rangle = \frac{m^4}{64\pi^2}\log\left[\frac{m^2}{\mu^2}\right]. \qquad (1.34)$$

This is confirmation of the veracity of Eq. (1.31). The remaining logarithmic term is physical because in a Higgs-like setting, where the mass of the field is generated by some other field, the logarithmic term cannot be subtracted by a local counter term.

Using Eq. (1.34) it is possible to estimate the change of the value of the matter contribution to the cosmological constant based on a standard electroweak symmetry breaking scenario, during which the Higgs field develops a non-zero vacuum expectation value. The lower theoretical value of the cosmological constant is

$$\langle 0|\hat{\rho}_{\rm vac}|0\rangle \sim 10^9 {\rm GeV}^4. \qquad (1.35)$$

The geometric contribution to the cosmological constant Λ, which also contains the unknown, constant value of the potential energy of the Higgs field before electroweak symmetry breaking, thus has to be fined-tuned by 56 decimal places [126].

So far all attempts to solve this issue have failed: supersymmetric theories or validating the energy scale of quantum chromodynamics only alleviate the problem slightly and involve deeper theoretical intricacies [188].

1.3 The theory of cosmological inflation

Even though cosmological inflation cannot explain the origin of the Universe, it solves, in a simple and elegant way, some of the problems that ΛCDM suffers. This theory consists of a brief epoch of accelerated expansion that took place in the very Early Universe, before radiation domination occurred. It was first proposed in 1981 by Guth [94] and Sato [192], independently, and a year later, a revised model (”new inflation”) was presented by Linde [140] and Albrecht and Steinhardt [12]. It is worth noting that a specific version of the inflationary scenario was proposed by Starobinsky one year earlier [210]. However, this paper did not point out explicitly the advantages of inflation as in Guth’s work.

In this era, the scale factor is accelerating, that is $\ddot{a} > 0$. Another way to describe this is by saying that the comoving Hubble length is decreasing with time. And a third equivalent manner is expressed as

$$-\frac{\dot{H}}{H^2} < 1, \tag{1.36}$$

because the Hubble parameter H remains almost constant during inflation. The solution will then be an almost exponential expansion, $a \propto \exp{(Ht)}$. Assuming GR, we can now draw a conclusion from inflation related to the energy density of the Cosmos. From the acceleration condition, and Eq. (1.20) it follows that

$$\text{Inflation} \leftrightarrow \rho + 3P < 0. \tag{1.37}$$

Because ρ is always assumed positive, in order to satisfy the latter condition, P must be negative. To achieve almost-exponential inflation, it is required that $P \approx -\rho$, which is a condition that can be satisfied by scalar fields [155].

1.3.1 How inflation solves the flatness, horizon and relic problems

One of Guth's papers of 1986 [141] explained how inflation could solve three of the Big Bang cosmology's uncertainties. This happened a decade before dark energy was first detected, therefore the cosmological constant problem was not known in the same form as nowadays.

Referring to the flatness issue, during inflation, whilst the Cosmos expands, the density parameter is

$$|\Omega - 1| \rightarrow 0. \tag{1.38}$$

This implies that $\Omega = 1$ is now an attractor solution, and for a large enough amount of inflation one obtains a cosmology that is extremely close to flat no matter the initial curvature. This theory therefore naturally provides an explanation for the observed flatness of the present Universe.

Considering the observable Universe to be well inside the horizon at the start of inflation, this model can also solve the horizon dilemma. As the expansion commences, the comoving horizon shrinks such that at the end of this era, the observable Universe lies outside of it. This explains the homogeneity in the CMB photons, as they were in causal contact before, meaning that comoving scales that are observed entering the horizon now were inside it in previous times.

Finally, inflation explains the lack of relic particle detection. The theorised particles were predicted to be formed at extremely high energies. However, if the primeval acceleration ends at a lower energy scale, these relics would have been diluted during the exponential Universe's expansion. This would made them practically impossible to detect today.

An exception to this is the gravitino. This particle is theorised to have been produced abundantly just after inflation happened [157]. Cosmology places severe constraints on gravitino mass density, but the current standard model is still unresolved for them [69].

The solution to these problems is bound to the condition that inflation lasted for at least $50 - 60$ e-folds [155]

1.3.2 Single-field inflation

After a few e-folds, the Universe flattens considerably ($K = 0$). Because the cosmological constant has a negligible effect at early times, during inflation it will be taken as $\Lambda = 0$. The energy density and pressure of the cosmological fluid dominant during this era are theorised to be dominated by scalar fields. These fields need to attain the condition $P < -\rho/3$ in order to achieve an accelerated expansion behaviour.

The simplest solution consists of the variation of a single field ϕ, named the inflaton, with equation of motion

$$\ddot{\phi} + 3H\dot{\phi} + \frac{dV(\phi)}{d\phi} = 0, \tag{1.39}$$

where H is the Hubble parameter, $V(\phi)$ is the potential of the scalar field, and a dot denotes a time derivative. The middle term in the equation acts as a friction term that slows the evolution of the scalar field as a result of the Universe's expansion. For this case, the Friedmann equation can be written as

$$H^2 = \frac{1}{3M_{\mathrm{Pl}}} \left(\frac{\dot{\phi}^2}{2} + V(\phi) \right), \tag{1.40}$$

Differentiating this equation and substituting in Eq. (1.39)

$$\dot{H} = \frac{-\dot{\phi}^2}{2M_{\mathrm{Pl}}^2}. \tag{1.41}$$

From the energy-momentum tensor $T_{\mu\nu}$, the inflaton's density and pressure are

$$\rho = \frac{\dot{\phi}}{2} + V(\phi), \quad P = \frac{\dot{\phi}}{2} - V(\phi). \tag{1.42}$$

For the case $V(\phi) > \phi^2/2$, the inflaton will have a negative pressure, ending up with an equation of state $w \approx -1$ for cases when the potential energy dominates over the kinetic contribution.

$$V(\phi) \gg \frac{\dot{\phi}^2}{2}. \tag{1.43}$$

The inflaton would then roll slowly down the potential; however, it is crucial that the kinetic energy is never zero, as this would cause the dragging term of the scalar field equation to disappear and therefore inflation would never end. For this theory to really solve the horizon, relic and flatness problems, the inflaton must accelerate slowly, causing the inflationary period to last long enough

$$\left|\frac{dV(\phi)}{d\phi}\right| \gg \left|\ddot{\phi}\right|. \tag{1.44}$$

This means the scalar field potential is close to flat and presents little variation during inflation. When a potential $V(\phi)$ is provided, with the aim of building an inflationary model, there are two parameters that are required to be small in order to obtain a slow-roll approximation behavior for the inflaton,

$$\epsilon_{\rm V} = \frac{M_{\rm Pl}^2}{2}\left(\frac{V'}{V}\right)^2, \quad \eta_{\rm V} = M_{\rm Pl}^2 \frac{V''}{V}, \tag{1.45}$$

where V' and $V^{''}$ are first and second order derivatives of the potential with respect to the scalar field ϕ.

Eqs. (1.45) are known as the potential-slow-roll (PSR) parameters. When their size is small they are used to justify neglecting the kinetic term in Friedmann Eq. (1.40) and the acceleration term in the inflaton's equation of motion (1.39). However, the attainment of these conditions is not sufficient to guarantee the appropriate dynamics for inflation, as the PSR parameters only bound the form of the potential, not the properties of the inflaton [136].

A way of obtaining more robust slow-roll parameters is by considering $H(\phi)$ as the primary quantity, which leads to the definition of the Hubble-slow-roll (HSR) approximation

$$\epsilon = -\frac{\dot{H}}{H^2}, \quad \eta = \frac{\dot{\epsilon}}{\epsilon H}. \tag{1.46}$$

The latter are much superior choices to the PSR equations. When $\epsilon \ll 1$, it is possible to neglect the kinetic term in Eq. (1.40). When $\eta \ll 1$, the acceleration term in Eq. (1.39) can be discarded. And the condition for inflation to occur is

$$\ddot{a} > 0 \leftrightarrow \epsilon < 1. \tag{1.47}$$

The inflationary period ends exactly when $\epsilon = 1$. When using the PSR parameters, the condition $\epsilon_{\rm V} < 1$ is only approximate [136].

The scalar field keeps running down the slope until it reaches the minimum and starts oscillating around the equilibrium value. At this point, the entire energy density of the Universe is contained in the inflaton. This energy must become free by converting to other types, until the Hot Big Bang commences. This conversion process is known as reheating, and its precise characteristics depend on the precise model, but in each case, it is completed when the inflaton decays into standard model particles, and all of the Universe's energy takes the shape of radiation in thermal equilibrium [122, 123, 142, 201].

Chapter 5 of this thesis is based on an MCMC exploration of the acceleration trajectory ϵ, with the aim of obtaining the minimum distance a single scalar field could have rolled during inflation, that is observationally allowed by CMB data.

1.4 Modified Matter (MM) and Modified Gravity (MG)

Inflation solves three of the five main inconsistencies within the ΛCDM paradigm. What about the fine tuning and cosmological constant problems? These constitute some of the most challenging of the current issues in theoretical physics.

If indeed, as the standard model shows, the cosmological constant is responsible for the present cosmic acceleration, it is necessary to explain why its value is so tiny at present. There have been efforts in this direction from particle physicists [114]. Another school of thought argues that only a vacuum with an energy density of the same order as that of the present Λ can sustain life, and this would explain our low-Λ habitat [215]. But these efforts are both uncertain, and highly controversial [16]. Then maybe we should consider other descriptions of DE different from Λ, a new model able to fit the observations and alleviate the standard case difficulties.

The fundamentals of the standard cosmological model assume GR to be valid in all scales. On one side, this theory has passed every test that has encountered. First, the measurements of the deflection of light by the Sun [199], followed by the explanation of Mercury's perihelion precession [59] and the measuring of the time delays between pulses towards a source and detection of the echoes [28]. Most recently, gravitational waves have finally been directly detected, and the signal produced by them matches the predicted one from Einstein's theory [2]. However, employing GR in cosmology is a huge extrapolation from our limited knowledge of gravity behaviour, as we have only been able to carry out tests in the Solar System scale. A modification of gravity may then be desirable to solve this problem. This is an issue of fundamental origin, where two main approaches have been developed in the last two decades [129].

1.4.1 Specifying the energy-momentum tensor $T_{\mu\nu}$

The first method consists of modifying the r.h.s. of Eq. (1.17) by considering a specific form of the energy momentum tensor $T_{\mu\nu}$ made of a fluid with an equation of state smaller than $w < -1/3$. This approach will be referred to as Modified Matter (MM).

One of the advantages of this procedure in comparison to Λ is that there is much more freedom with the time evolution of w, which means an equation of state that changes with time can be considered. This is the case because observations do not impose restrictions on the past evolution of w. Scalar fields are well suited to this purpose (similarly to the inflation paradigm, where w also evolves). A variety of options for $T_{\mu\nu}$ have been proposed and here a couple of them will be mentioned. A comprehensive review of the subject is Ref. [63].

Quintessence: This theory makes use of scalar fields with slowly-varying potentials minimally coupled to gravity [44]. The action for Quintessence is given by

$$\mathcal{S} = \int d^4x\sqrt{-g}\left[\frac{1}{2\kappa^2}R - \frac{1}{2}g^{\mu\nu}\partial_\mu\phi\partial_\nu\phi - V(\phi)\right] + \int d^4x\sqrt{-g}\mathcal{L}_{\mathrm{M}}\left[g_{\mu\nu}, \Psi\right] , \quad (1.48)$$

where ϕ is the dynamical quintessence field, g is the determinant of the metric $g_{\mu\nu}$, R is the Ricci scalar, and $\mathcal{L}_{\mathrm{M}}$ is the Lagrangian for non-relativistic matter.

Some of quintessence's characteristic potentials have been constructed with a strong base in particle physics [16]. Chapter 2 provides a full introduction to this topic, along with a study of observational constraints on one of its most characteristic cases, the pseudo-Nambu Goldstone Boson (PNGB) potential.

K-essence: Instead of relying on the potential energy, as in the previous case, in these models, the cosmic acceleration is driven by the scalar field's kinetic energy. This idea was first proposed by Armendariz-Picon [20] to explain high-energy inflation, and later on, it was applied by Chiba [56] in the context of late-time acceleration. K-essence is characterised by a scalar field with non-canonical kinetic energy. The most general action for this case is

$$\mathcal{S} = \int d^4x\sqrt{-g}\left[\frac{1}{2\kappa^2}R + P(\phi, X)\right] + \int d^4x\sqrt{-g}\mathcal{L}_{\mathrm{M}}\left[g_{\mu\nu}, \Psi\right] , \tag{1.49}$$

where ϕ is the scalar field, $X = (-1/2)\, g^{\mu\nu}\delta_\mu\phi\delta_\nu\phi$ and the Lagrangian density $P(\phi, X)$ corresponds to a pressure density [63].

Phantom fields: The observational data are consistent with an equation of state more negative than the value of $w = -1$. This region is referred to as being some form of phantom or ghost energy. Several specific models, such as Brans-Dicke gravity [75, 187], inhabit this regime. The most simple way to express this idea is by a scalar field with negative kinetic energy.

$$\mathcal{S} = \int d^4x\sqrt{-g}\left[\frac{1}{2\kappa^2}R + \frac{1}{2}\left(g^{\mu\nu}\delta_\mu\phi\delta_\nu\phi\right)^2 - V(\phi)\right] + \int d^4x\sqrt{-g}\mathcal{L}_{\mathrm{M}}\left[g_{\mu\nu}, \Psi\right] , \tag{1.50}$$

where the sign of the kinetic term is opposite compared to the action for an ordinary scalar field [63].

There are a couple more alternatives to dark energy under this approach; however, the second method offers a much broader array of possibilities.

1.4.2 Specifying the Einstein tensor $G_{\mu\nu}$

In the cosmological constant scenario, the Lagrangian density is $f(R) = R - 2\Lambda$, where R is the Ricci scalar. If a different function is given, the l.h.s. of the Einstein Eq. (1.17) is modified. This approach will be referred as Modified Gravity (MG). However, such alterations are not trivial.

As mentioned at the end of Section 1.1, Einstein's equations are the only second-order local equations of motion for a metric derivable from the Einstein-Hilbert action in 4D [60]. If GR is to be modified, Lovelock's theorem [153, 154] states that at least one of the following four conditions need to occur [129]:

- Extra degrees of freedom
- Higher derivatives
- Higher-dimensional spacetime
- Non-locality

Ref. [129] includes a very complete review of these theories. Here a handful of them will be mentioned, in particular those which are important for the forthcoming chapters.

Brans-Dicke gravity: This is the simplest way to modify GR [35]. This theory includes a scalar field non-minimally coupled to gravity

$$\mathcal{S} = \int d^4x\sqrt{-g}\left(\Psi R - \frac{w_{\rm BD}}{\Psi}(\delta\Psi)^2\right) + \int d^4x\sqrt{-g}\mathcal{L}_{\rm M}, \tag{1.51}$$

where the scalar field perturbation $\Psi = \Psi_0 + \phi$ obeys

$$w_{\rm BD} = -\left(\frac{4\pi G\rho}{\nabla^2\phi} + \frac{3}{2}\right) \tag{1.52}$$

GR is recovered in the large $w_{\rm BD}$ limit. When imposing Solar System constraints, derived from observations of the time delay of radio signals from the Cassini spacecraft as it passed behind the Sun [28], it is found that $w_{\rm BD} > 40,000$ [60], which makes this theory basically indistinguishable from ΛCDM on all scales. This is one of the main problems of modified gravity models: because the Solar System tests are so severe, if they are imposed on the parameters of the model, there is very little room to modify gravity on cosmological scales [129].

$f(R)$ **gravity:** Because of its relative simplicity, this is a very popular theory of gravity which consists of generalising the Einstein-Hilbert Lagrangian to be a function of the Ricci curvature [42, 210]. Even so, it is still a phenomenologically based theory which main purpose is to aid in the understanding of the principles and limitations of modified gravity. Good reviews in the subject are Refs. [66, 167, 207]. There are two variational approaches to derive the field equations in $f(R)$ gravity; and both of them reduce to the Einstein-Hilbert case when $f(R) = R$. However, for more general actions, the two formalisms lead to different equations of motion and therefore, to two versions of $f(R)$ gravity.

- **The metric formalism:** This procedure consists of obtaining the equations of motion by the standard metric variation. In this case the action is

  $$\mathcal{S} = \frac{1}{2\kappa^2}\int d^4x\sqrt{-g}f(R) + \mathcal{S}_{\rm M}(g_{\mu\nu}, \Psi). \tag{1.53}$$

  The action (1.53) is varied with respect to $g_{\mu\nu}$, yielding the field equations

  $$f_R R_{\mu\nu}(g) - \frac{1}{2}f(R)g_{\mu\nu} - \nabla_\mu\nabla_\nu f_R + g_{\mu\nu}\Box f_R = \kappa^2 T_{\mu\nu}, \tag{1.54}$$

where the Ricci scalar is $R = g^{\mu\nu} R_{\mu\nu}$, f_R is the first derivative of the function $f(R)$ and the Ricci tensor $R_{\mu\nu}(g)$ corresponds to the metric connection [145].

The derivation of Eq. (1.54) is similar to the Einstein-Hilbert case; however, the third and fourth term on the l.h.s. of Eq. (1.54) are not present in Eq. (1.17). This has to do with the surface terms that appear in the variation.

For the Einstein-Hilbert case, the surface terms can be gathered into a total variation of a quantity. Then, it is possible to add a total divergence to the action and therefore arrive to a well-defined variational principle. However, the surface terms in the variation of the action (1.53) do not consists of a total variation of some quantity, and the same procedure as in (1.16) is not possible to reproduce. The resulting equations of motion (1.54) are of fourth order, thus, it can be classified as a higher-derivative theory [207].

- **The Palatini formalism:** The term $f(R)$ gravity is used generically for a theory in which the Lagrangian is some function of the Ricci scalar, but that Ricci scalar does not necessarily need to be R. In the Palatini approach, there are two very important things to consider. The first is that the metric and the connection are treated as independent variables and one varies the corresponding action with respect to both of them.

  The Riemann tensor and the Ricci tensor are constructed with the independent connection $\hat{\Gamma}$. Note that the metric is not needed to obtain the latter from the former. The Ricci tensor constructed with this independent connection is labelled as $\mathcal{R}_{\mu\nu}(\hat{\Gamma})$, whilst the corresponding Ricci scalar is $\mathcal{R} = g^{\mu\nu}\mathcal{R}_{\mu\nu}(\hat{\Gamma})$ [207]. The action now takes the form

$$\mathcal{S} = \frac{1}{2\kappa^2}\int d^4x\sqrt{-g}f(\mathcal{R}) + \mathcal{S}_{\mathrm{M}}(g_{\mu\nu}, \Psi). \tag{1.55}$$

  The second consideration that needs to be made in order for a theory to be considered as of Palatini type is that the matter action $\mathcal{S}_{\mathrm{M}}$ depends only on the metric and the matter fields, not on the independent connection, hence

$$\frac{\delta \mathcal{S}_{\mathrm{M}}}{\delta \hat{\Gamma}^{\lambda}_{\mu\nu}} = 0. \tag{1.56}$$

  This assumption has very deep consequences for the physical meaning of the independent connection [206].

  Whilst the matter Lagrangians for scalar fields do not depend on the connection, there are matter fields (such as fermions) that do depend on it. Therefore, adopting this assumption can lead to two things: either this theory is only valid for certain matter fields or those fields that couple to the connection couple to the metric-associated connection, not the independent one.

The first option is not very desirable, as it would severely restrict the amount of fields where this theory is valid. The second option is more appealing. It would mean, however, that parallel transport and the covariant derivative are associated to the metric connection, in a sense, the metric connection is the real connection, whilst the independent one is an auxiliary field whose introduction adds a scalar degree of freedom.

The fact that the independent connection adds a single degree of freedom to the theory is reminiscent of the Brans-Dicke theory and actually, the action (1.55) is dynamically equivalent to the action of a scalar-tensor theory with Brans-Dicke parameter $w_0 = -3/2$ [48].

Varying the action (1.55) with respect to the metric $g_{\mu\nu}$ and to the independent connection gives the equations of motion

$$f_{\mathcal{R}}\mathcal{R}_{\mu\nu}(\hat{\Gamma}) - \frac{1}{2}f(\mathcal{R})g_{\mu\nu} = \kappa^2 T_{\mu\nu}, \tag{1.57}$$

$$\hat{\nabla}_\lambda\left(\sqrt{-g}f_{\mathcal{R}}\, g^{\mu\nu}\right) = 0, \tag{1.58}$$

where $\hat{\nabla}_\lambda$ denotes the covariant derivative defined with the independent connection.

There exists a third type of $f(R)$ theory, known as metric-affine gravity, that comes about when the assumption of no dependency of $\mathcal{S}_{\mathrm{M}}$ on the independent connection is broken. In such case, the independent connection does have the usual geometrical properties. The resulting equations of motion are similar to (1.57, 1.58) but include extra torsion and matter terms. This formalism is covered in [207].

Hybrid metric-Palatini gravity: This is a hybrid variation of the two $f(R)$ approaches explained before, where the purely metric Einstein-Hilbert action is supplemented with an $f(\mathcal{R})$ Palatini term. The four-dimensional action describing the hybrid metric-Palatini gravity is given by

$$\mathcal{S} = \frac{1}{2\kappa^2}\int d^4x\sqrt{-g}\left[R + f(\mathcal{R})\right] + \int d^4x\sqrt{-g}\mathcal{L}_{\rm M}(g_{\mu\nu}, \Psi), \tag{1.59}$$

where R is the metric Einstein-Hilbert Ricci scalar and $\mathcal{R} = g^{\mu\nu}\mathcal{R}_{\mu\nu}$ is the Palatini curvature.

A more complete study of hybrid metric-Palatini gravity (hybrid $f(\mathcal{R})$) is presented in Chapter 3 of this thesis, including a discussion of some deficiencies present in the metric and Palatini procedures and how this novel model can solve them. After that, an analysis of the background evolution constraints for specific models of this formalism are presented.

Chapter 4 uses this theory to impose observational bounds on early modified gravity effects. For this purpose, the hybrid $f(\mathcal{R})$ linear perturbations were added to the numerical calculation of the previous background analysis.

Horndeski gravity: These are the most general set of theories of a single extra scalar degree of freedom, which have equations of motion with at most second-order derivatives on any background. They were first introduced by Gregory Horndeski in 1973, in a quickly forgotten paper [101], but with the new emphasis on modified gravity his work was revived [52, 67]. The majority of universally coupled dark energy and modified gravity models belong to this class. The action for this case is given in Eq. (4.21) of Ref. [101].

Effective field theory: This description is a generalisation of Horndeski gravity where all single-field models are accepted, regardless of the order of their equations of motion. This unifying formalism is very useful to effectively discern within the ever growing array of MG models [25, 93]. The action for this case is given in Eq. (4) of Ref. [93].

1.4.3 Screening mechanisms

When Einstein gravity is modified, new degrees of freedom are introduced in the gravitational sector. These new particles mediate a fifth force, and consequently the modified theory is in need to employ some type of mechanism to evade local tests of gravity, which as will be seen later, are very constraining. For theories that can be embedded in the scalar-tensor representation, the Solar System constraints are avoidable whilst keeping an interesting phenomenology for the scalar field [113].

The key point of screening mechanisms is that if we consider theories with a non-minimally coupled scalar field, then in the presence of other matter fields these scalars can acquire an effective mass parameter that is environmentally dependent [60]. This makes it possible to engineer situations where the field behaves differently in different environments [113].

The Einstein frame is ideal for the formulation of screening theories, because in this case, the coupling between the scalar curvature and ϕ is minimal, but the scalar field couples non-minimally to matter fields. In many general scalar-tensor theories the scalar field obeys the equation of motion

$$\Box\phi = \frac{dV_{\text{eff}}}{d\phi}; \quad V_{\text{eff}} = V(\phi) + \rho e^{\sqrt{8\pi}\beta\phi}. \tag{1.60}$$

where ρ is the environmental density and β denotes the coupling of ϕ to the matter fields [60].

Screening mechanisms can be classified according to the order of the Newtonian potential Φ_N that are comparable to the value of the cosmological constant Λ. One of the most common cases and one which is of importance to the discussion of chapters 3 and 4 is the **chameleon mechanism**; where the potential and matter coupling are chosen so that the effective mass of the scalar field is

$$m^2_{\text{eff}}(\phi) = \frac{d^2V_{\text{eff}}}{d\phi^2} = \frac{d^2V}{d\phi^2} + \rho\frac{d^2e^{\sqrt{8\pi}\beta\phi}}{d\phi^2}. \tag{1.61}$$

This arrangement has the ability to increase the mass of the field in regions of high density, like the Solar System [113]. The behaviour of scalar fields outside of massive objects, when the chameleon mechanism is present can be shown to be crucially dependent on the difference in the value of the scalar field inside the object, ϕ_{c}, and asymptotically, ϕ_∞, while Φ_{c} is the value of the Newtonian potential at the surface of the object. Therefore, when one satisfies the condition

$$\frac{\sqrt{8\pi}(\phi_\infty - \phi_{\text{c}})}{6\beta\Psi_{\text{c}}} \ll 1 \tag{1.62}$$

the resulting configuration of gravitational fields is found to be one in which ϕ occupies the minimum of the effective potential inside the bulk of the massive object, except for a thin region just below the surface where the value of ϕ rises [60]. This is known as the “thin shell” condition. Khoury and Weltman argue that in order not to violate the weak equivalence principle, and obtain unacceptable deviations from GR in the Solar System, the Earth and other astrophysical bodies should satisfy the thin shell condition [119, 120].

In this context, metric $f(R)$ theories have been widely studied. This is because the only way for these models to overcome the existence of ghosts and instabilities and to pass the gravitational tests is by employing a chameleon mechanism [37]. When $f(R)$ theories are recast in the scalar tensor formalism its equation of motion become of second order. In this case ϕ can be defined by

$$e^{-\frac{2\beta\phi}{M_{\rm Pl}}} = f_R, \tag{1.63}$$

A chameleon theory is essentially just a scalar-tensor theory in which the potential has certain properties. In a general chameleon theory, β, which parametrises the strength of the coupling of ϕ to matter, could take any value, and potentially even be different for distinct matter species. If a chameleon theory is equivalent to a $f(R)$ theory, however, $\beta = \sqrt{1/6}$, and is the same for all types of matter. If a $f(R)$ theory is not equivalent to a chameleon theory it would generally be ruled out by laboratory tests of gravity, and/or result in no detectable deviations from GR over astrophysical scales [37].

1.4.4 Theoretically consistent models of MM/MG

Any prospective MM/MG model needs to comply with several consistency checks. For instance, the solutions need to be stable. This condition can be broken when the scalar field of a theory has a negative mass squared $m^2 < 0$. This is known as a tachyonic instability, and even if it's problematic, it is not fatal as long as its time scale is long enough. A more serious unsteadiness occurs when the kinetic term of the scalar field has a wrong sign, a phenomenon known as ghost instability [129].

Another common problem happens when the scalar field has non-linear interaction terms apart from the kinetic term. These can become important at high scales, which means that theories which present it need to be treated effectively, i.e, they are only valid up to low range.

For a theoretically consistent theory, passing the observational tests is the next challenge. The most stringent are the Solar System constraints obtained from classic GR experiments. One way of obtaining these is by measuring the bending of starlight by the Sun, an analysis that can be performed accurately using very-long-baseline radio interferometry (VLBI). The deflection angle θ of stars due to the Sun is observed to be [199]

$$\Delta\theta = (0.99992 \pm 0.00023) \times 1.7505'', \tag{1.64}$$

where $\Delta\theta = 1.7505''$ corresponds to the GR limit.

Another prediction is found from measuring the time delays between transmission of signals from Earth towards a planet and the detection of the echoes. Because the speed of a light wave depends on the strength of the gravitational potential along its path, the time dilation should increase when the signal passes near the Sun [198]. This measurement has been obtained most recently by the Cassini spacecraft as [28]

$$\Delta t = (1.00001 \pm 0.00001) \times \Delta t_{\mathrm{GR}}. \tag{1.65}$$

Finally, the equation of state for DE is constrained by *Planck* TT + lowP + lensing + JLA Supernovae data to be [8]

$$w_{\mathrm{DE}} = -1.006 \pm 0.045, \tag{1.66}$$

where w_{DE} is assumed constant throughout the whole expansion history. The standard model is in excellent agreement with all these constraints. Any serious MM/MG model should have a background evolution that is very similar to that of Λ, and pass all these tests.

Finally, it is important to note that in the context of GR, both approaches 1.4.1 and 1.4.2 are equivalent. This division is in place more in order to classify the models than anything else. The stress-energy tensor $T_{\mu\nu}$ can always be rewritten by absorbing all the gravity modifications of what is typically included in the l.h.s. of Einstein's equation. When considering only gravitational interactions, GR cannot distinguish between a modified form of matter and modified gravity. However, from the point of view of quantum field theory, this is no longer the case, and the two approaches become distinguishable [16].

1.5 Cosmological perturbation theory

Section 1.1 provided a representation of the evolution of a homogeneous Universe. However, in order to describe the structures observed in the Cosmos today, and to be able to confront cosmological models with observations from the CMB and large scale structure (LSS), it is necessary to perturb Einstein's equations to first order. This is a sufficiently complex approach to account for the small temperature anisotropies of the CMB ($\Delta T/T \sim 10^{-5}$) and to describe the matter distribution at linear regime scales larger than 30 h^{-1}Mpc.

Each individual constituent (the inflaton, baryons, radiation, DE, DM) has an associated density fluctuation. Perturbations of the metric arise from inhomogeneities in the distribution of the Universe's components,

$$g_{\mu\nu} = g^{(0)}_{\mu\nu} + h_{\mu\nu}, \tag{1.67}$$

where $h_{\mu\nu} \ll g_{\mu\nu}$ is the perturbation and $g^{(0)}_{\mu\nu}$ constitutes the background Universe. Vector and tensor perturbations also cause metric modifications; however, the standard model does not predict vectorial contributions, which would cause the metric tensor to have non-zero off-diagonal terms. These type of perturbations would introduce vortex motions in the primordial plasma which are expected to decay rapidly.

Nonetheless, ΛCDM does predict the production of gravitational waves during inflation. A FLRW Universe perturbed by gravitational waves has a metric

$$ds^2 = a(\eta)^2 \left[d\eta^2 - (\delta_{\rm ij} + 2h_{\rm ij}) dx^{\rm i} dx^{\rm j} \right]. \tag{1.68}$$

For gravitational waves $h_{\rm ij}$ is restricted to be trace-free $h^{\rm i}_{\rm i} = 0$ and transverse, $\partial h_{\rm ij} = 0$ so that only two independent components survive, h_+ and h_-. The field equations for h_+ and h_- give equations of motion for each polarisation of the gravitational waves,

$$h''_\pm + 2hh'_\pm + k^2 h_\pm = 0, \tag{1.69}$$

which is the equation of motion of a massless scalar field.

The scalar perturbations to the metric tensor can be modelled with two functions

Φ and Ψ in the FRW metric as

$$ds^2 = a^2(\eta)\left[-(1+2\Psi)d\eta^2 + (1-2\Phi)dx^{\mathrm{i}}dx_{\mathrm{i}}\right], \tag{1.70}$$

where the convention of Ma and Bertschinger has been adopted [158].

The function Φ describes Newton's gravitational field, and Ψ is the perturbation of the space curvature. The above equation is given in the Newtonian conformal gauge, which has the advantage, as its name indicates, of recovering the Newtonian limit. This feature is appealing because it provides a direct interpretation of the functions Ψ and Φ.

An alternative and popular option is the synchronous gauge

$$ds^2 = a^2(\eta)\left[-d\eta^2 + (\delta_{\mathrm{ij}} + h_{\mathrm{ij}})dx^{\mathrm{i}}dx^{\mathrm{j}}\right], \tag{1.71}$$

which is better suited for numerical computations of the anisotropies and inhomogeneities of the Universe. of Fourier coefficients of the fluctuations in density as compared to an unperturbed Universe.

1.6 The matter power spectrum

On large scales, our Universe is extremely homogeneous and isotropic. Nonetheless, at small scales, there exists a great variety of highly-non linear structure. Given the random nature of cosmological perturbations it is necessary to use statistical measures in order to understand them. To this effect, it is useful to work in Fourier space as this makes it easier to separate large from small scales.

In the cases of the CMB and large scale structure, the most important statistc is the **two-point function**, called the **power spectrum** in Fourier space. If the mean density of galaxies is $\bar{n}$, then we can characterize the inhomogeneities with $\delta(\vec{x}) = (n(\vec{x}) - \bar{n})/\bar{n}$, or its Fourier transform $\tilde{\delta}(\vec{k})$. The matter power spectrum is defined through

$$\langle \tilde{\delta}(\vec{k})\tilde{\delta}(\vec{k'})\rangle = (2\pi)^3 \mathcal{P}_\delta(k)\delta^3(\vec{k} - \vec{k'}), \tag{1.72}$$

where the angular brackets denote an average over the whole distribution, $\delta^3()$ is the Dirac delta function which constrains $\vec{k} = \vec{k'}$ and the units are $(\text{length})^3$.

A similar equation as (1.72) exists for any scalar quantity that it is applied to. It indicates that the power spectrum is the spread, or the variance, in the distribution. If the under and overdense regions are abundant, the power spectrum will be large, whereas for the contrary case, the spectrum will be small.

On large scales, the most important observable is the power spectrum of the matter distribution. The simplest way to relate the matter overdensity to the potential Φ at late times is to use Poisson's equation

$$\Phi = -\frac{4\pi G \rho_{\mathrm{M}} a^2 \delta}{k^2} \tag{1.73}$$

Given Eqs. (1.27) and (1.21) this is

$$\Phi = -\frac{3\delta \Omega_{\mathrm{M}} H_0^2}{2ak^2} \tag{1.74}$$

Therefore the power spectrum of the gravitational potential is

$$\mathcal{P}_{\Phi} = \frac{9\Omega_{\mathrm{M}}^2 H_0^4}{4a^2k^4} \mathcal{P}_{\delta} \tag{1.75}$$

In order to express the power spectrum as a dimensionless function, $d^3k\mathcal{P}(k)/(2\pi^3)$ is associated with the excess power in a bin of width dk centered at k. After integrating over all orientations of k, this becomes $(dk/k)\Delta^2(k)$, with

$$\Delta^2(k) = \frac{k^3 \mathcal{P}(k)}{2\pi^2} \tag{1.76}$$

Small Δ corresponds to small inhomogeneities, while large Δ indicates nonlinear perturbations. The dimensionless power spectrum of the potential can be parametrised as

$$\Delta_{\Phi}^2(k) = \frac{k^3}{2\pi^2}\mathcal{P}_{\Phi} = A_{\mathrm{s}} \left(\frac{k}{k_*}\right)^{n_{\mathrm{s}}-1+\frac{1}{2}\alpha_{\mathrm{s}} \ln \frac{k}{k_*}}, \tag{1.77}$$

where A_{s} is the amplitude of the power spectrum, k_* is an arbitrary pivot scale, n_{s} and α_{s} are the spectral index and the running of the spectral index, given by

$$n_{\mathrm{s}} = 1 + \frac{d \ln \Delta_{\Phi}^2}{d \ln k}, \quad \alpha_{\mathrm{s}} = \frac{dn_{\mathrm{s}}}{d \ln k} \tag{1.78}$$

Because this equation is an expansion in $\ln k$, it is only valid for a limited range of scales. The power spectrum is said to be scale invariant if there is zero running and $n_\mathrm{s} = 1$. For the simplest model and a Gaussian distribution, the power spectrum contains all of the statistical information, with higher-order correlation functions depending on the 2-point function [71].

1.7 The Markov Chain Monte Carlo method and Bayesian Statistics

The astrophysical methods and observations have, for several years, provided a large amount of data from a variety of sources [133]. In order to extract as much information as possible from these data, it is convenient to summarise it by estimates of a set of cosmological parameter values. This in turn can help us answer interesting questions about the nature of our Universe. One of the popular tools available to meet this end is Bayesian statistics. This approach is particularly suitable for dark energy research because of its flexibility in combining between various parametrisations [16].

1.7.1 Bayes' theorem

Let $\theta = \theta_1, ..., \theta_\mathrm{p}$ denote a model with p unobserved parameters, D denote the data and H denote the overall hypothesis space. Then Bayes' theorem is stated as

$$P(\theta|D, H) = \frac{P(D|\theta, H)P(\theta|H)}{P(D|H)} \tag{1.79}$$

where:
$P(\theta|D, H)$ is the conditional probability of θ.
$P(D|\theta, H)$ is a data-dependent term which is called the likelihood of θ.
$P(\theta|H)$ is a term that reflects beliefs about dependence structures in θ before evidence is taken into consideration and is called the prior probability.
$P(D|H)$ is the probability of observing the data without regard of θ and is known as the evidence.

The conditional probability $P(\theta|D, H)$ is the probability density function in multiparameter space, and it contains all of the information combining prior knowledge and observations. Bayes' theorem constitutes the basis of Bayesian inference. Written in terms of the quantities' names it is

$$\text{Posterior} \propto \frac{\text{Prior} \times \text{Likelihood}}{\text{Evidence}}. \tag{1.80}$$

Likelihoods are products of the probabilities of many data points, and they tend to be very small. It is easiest to work with log(likelihood), as they add to each other [159].

1.7.2 Marginal probability

In many cases, it is customary to only be interested in the posterior probability of some parameters. This can happen when, having some data, we are interested in a certain parameter and want to take into consideration the effect of other nuisance parameters with non informative priors. This can be achieved by doing integrals over continuous variables. For example, the posterior distribution $P(\theta_\mathrm{i}|D,H)$ for some subset $\theta_\mathrm{i} \,\epsilon\, \theta$ can be expressed as [99]

$$\begin{aligned} P(\theta_\mathrm{i}|D,H) &= \int P(\theta_\mathrm{i}|D,H)d\theta_{-\mathrm{i}} \\ &= \int P(\theta_\mathrm{i}|\theta_{-\mathrm{i}},D,H)P(\theta_{-\mathrm{i}}|D,H)d\theta_{-\mathrm{i}}. \end{aligned} \tag{1.81}$$

1.7.3 Computational tools and MCMC

Calculation of probability densities requires integration over a possibly high dimensional parameter space $\theta \,\epsilon\, \Theta$. In the past, the need to evaluate integrals was a major stumbling block when attempting to use Bayesian methods. Most conveniently, in 1990, Gelfand and Smith [88] published a paper presenting a numerical technique known as Markov Chain Monte Carlo (MCMC), although this technique was already known since the 1950's. The name "Monte Carlo" started as an expression resembling the, in those days, illegal activity of gambling. The MCMC method was developed soon after the apparition of ordinary Monte Carlo, and was well known to statisticians for decades, but Gelfand and Smith made it known to a wider community [41, 133].

A Markov chain is a sequence $\theta_1, \theta_2, ...$ of random elements of some set in which the conditional distribution of $\theta_{\mathrm{M}+1}$ given by $\theta_1, ..., \theta_\mathrm{M}$ depends on $\theta_{\mathrm{M}+1}$ only. A Markov chain has stationary transition probabilities if the conditional distribution of $\theta_{\mathrm{M}+1}$ given θ_{M} does not depend on M. This is the main kind of Markov chain of interest in MCMC [41].

The way MCMC works is by first constructing a Markov chain on the state space $\theta \,\epsilon\, \Theta$, whose steady state distribution is the posterior distribution of interest $P(\theta|D, H)$. MCMC procedures return a collection of M samples $\theta_1, ..., \theta_{\mathrm{M}}$ where each sample can be assumed to be drawn from $P(\theta|D, H)$ [99],

$$P(\theta^{\mathrm{i}} \,\epsilon\, A) = P(\theta \,\epsilon\, A|D, H) \tag{1.82}$$

for any set $A \,\epsilon\, \Theta$, or, $\theta^{\mathrm{i}} \sim P(\theta|D, H)$ for $\mathrm{i} = 1, ..., M$.

1.7.4 Burn-in

Burn-in is a colloquial term borrowed from electronics that describes the practice of throwing away some iterations at the beginning of a MCMC run. This means that from an initial point to a certain number of steps n, all the output of a Markov chain is erased. After point n all the other points are considered normally.

Burn-in is a method to find a good starting point, but the application of this concept is not particularly good. In electronics, many components fail quickly, and those that do not are a more reliable subset. Hence, a factory performs a burn-in to eliminate the worst ones. However, the failure of a Markov chain is related to its lack of convergence, and is different from electronic component failure. Burn-in can cure the firsts elements of the chain, but other “dead transistors” could occur later on. A Markov chain started anywhere near the center of the equilibrium distribution needs no burn-in. A good rule to follow is to start the next run where the last run ended [41].

Another problem with burn-in is biased estimations. If one could start with a realisation from the equilibrium distribution, then the Markov chain would be stationary and the Monte Carlo approximation would be an unbiased estimator of what it estimates. Burn-in does not produce a realisation from the equilibrium distribution, hence it is biased.

1.7.5 Thinning

The subject of thinning comes about when we are presented with a Markov chain that is strongly autocorrelated. This produces contour plots that tend to clump in certain areas, and that are unrepresentative of the underlying posterior distribution. In order to produce a more precise estimate of the posterior sample, we would like to get rid of the correlation by thinning it, using only every n^{th} step.

This method is useful for processing chains under memory or time constraints. However, thinning a sample also presents downsides. It has been shown that this practice is not usually appropriate to produce precise estimates from a MCMC sample. Instead, producing a longer, unthinned chain yields better estimates of the true posterior distribution. The needed length of the chain would depend on the severity of the autocorrelation. One way of testing for this is to produce several independent chains and assess the produced estimates by checking whether they are comparable or not to each other [144].

1.7.6 Parameter estimation

In order to finally determine the best-fitting parameters (and the errors on them) of a specific model, it is very useful to employ the χ^2 statistic:

$$\chi^2 = \sum_{\mathrm{i}}^{\mathrm{N}} \left(\frac{x_{\mathrm{i}} - \mu_{\mathrm{i}}}{\sigma_{\mathrm{i}}} \right)^2 , \tag{1.83}$$

where N is the number of measurements going from $\mathrm{i} = 1, ..., N$, $x_{\mathrm{i}} \pm \sigma_{\mathrm{i}}$ are the data and μ_{i} is the model. For the data and the model to be consistent with each other, the hypothesis $x_{\mathrm{i}} = \mu_{\mathrm{i}}$ is tested. If this gives a large probability, the model has passed the test. If this probability is low , the model can be ruled out. Assuming that the N variables are Gaussian-distributed the χ^2 probability distribution is given as

$$P(\chi^2) \propto \left(\chi^2\right)^{\frac{\nu-2}{2}} e^{-\frac{\chi^2}{2}} \tag{1.84}$$

where $\nu = N - p$ is the number of degrees of freedom and p is the number of free parameters in the model.

The mean and variance of this distribution are $\bar{\chi}^2 = \nu$, $\mathrm{Var}(\chi^2) = 2\nu$. This mean value makes intuitive sense because it is expected that each data point should lie about $1-\sigma$ from the model. Thus if the model is correct, $\chi^2 \sim \nu \pm \sqrt{2\nu}$ [31].

A model typically contains free parameters. Consider a model with three of these, a, b and c. The best-fit for these parameters is determined by varying them to find the minimum χ^2 statistic of the data, χ^2_{min}.

The joint error distribution of a, b and c can be determined by calculating the values of χ^2 for a parallelepiped of a, b and c values, where the parallelepiped spans a parameter range much wider than the eventual errors in a, b and c. With this 3D parallelepiped we can plot tri-dimensional contours of constant $\chi^2 = \chi^2_{\mathrm{min}} + \Delta\chi^2$. Joint confidence regions of (usually) 68% and 95% confidence for a and b can be defined by the zone in this parameter space that satisfies $\chi^2 < \chi^2_{\mathrm{min}} + \Delta\chi^2$, where $\Delta\chi^2$ is determined by the number of free parameters (three, in this case).

However, a more common and useful representation for the parameter space is using 2D contour plots of two parameters at a time. In order to represent, for instance, a and b, in this manner, it is necessary to consider all possible values for the parameter c, that is, performing the marginalisation procedure mentioned previously. This is carried out using the relation between χ^2 and likelihood that holds for Gaussian variables:

$$\text{Likelihood} \propto e^{-\frac{\chi^2}{2}} \tag{1.85}$$

The process is as follows:

- Convert the χ^2 parallelepiped into a probability 3D surface $P_{\mathrm{3D}}(a,b,c) \propto \exp -\chi^2/2$.
- Normalise the probabilities such that $\sum_{\mathrm{a,b}} P_{\mathrm{3D}}(a,b,c) = 1$.
- Produce the marginalised probability distribution for each individual parameter by summing the probability parallelepiped over all the other parameters, for example $P_{\mathrm{2D}}(a,b) = \sum_{\mathrm{c}} P_{\mathrm{3D}}(a,b,c)$. This would determine the probability distribution of a, b given all possible values of c.
- Obtain the χ^2 for a grid of a and b values from the marginalised probability distribution $P_{\mathrm{2D}}(a,b)$ and plot the contours of constant $\chi^2 = \chi^2_{\mathrm{min}}+\Delta\chi^2$ [31].

1.7.7 Alternatives to MCMC sampling

The advent of MCMC sampling has forever changed the possibilities attainable with Bayesian statistics and its application to a wide variety of problems. Nonetheless, MCMC methods are not without faults – they can be slow to converge and its convergence can be difficult to diagnose [32]. As such, alternatives to this methodology are constantly being explored. Here I mention some of them:

- **Variational inference methods:** These methods are of a deterministic nature. Their basic idea is to formulate the computation of a marginal probability in terms of an optimisation problem [90, 112, 170, 220, 225]. This procedure leads to a simplified optimisation problem that depends on a number of free parameters, known as variational parameters. Solving for those gives an approximation to the marginal probabilities of interest [32].

- **Expectation propagation (EP):** This is also a deterministic method that claims to achieve higher accuracy than both MCMC and variational inference with similar computational cost. EP is an extension of *assumed density filtering* (ADF), a sequential method for computing an approximate posterior distribution where observations are processed one by one, updating the posterior distribution which is later approximated before processing the next observation. However, the method is weak in the sense that it continuously discards information, which may turn out to be important later. Expectation propagation extends ADF by incorporating an interactive refinement of the approximations, in which the information from later observations refines the choices made earlier, so that the most important information is retained [163].

- **Nested sampling:** this method (and several other refined versions of it [76, 164, 200]) has been widely applied to astrophysics since John Skilling first proposed it [203]. It consists of estimating directly how the likelihood function relates to the prior. Here the evidence is the principal result of the computation and is accompanied by an estimate of numerical uncertainty. The method samples within a hard constraint on likelihood value. Progress is measured in terms of the shape of the nested contours of likelihood, not on the likelihood values. Samples of the posterior distribution are a by-product. A multimodal version of this type of sampling is a robust alternative – especially when a model shows a high degree of correlation between its parameters [76].

1.8 Cosmological observables

In order to impose constraints on cosmological models, one needs to employ a computational analysis using observational evidence. These data are obtained by considering distinctive ways to measure gaps between us and other objects in the expanding Universe: the luminosity distance from Supernova type Ia (SNIa); the baryon acoustic oscillations (BAO); the temperature anisotropies and polarisation, shift parameter, acoustic scale and redshift of decoupling from the cosmic microwave background (CMB). These features will be introduced in sections 1.8.1 to 1.8.3 below, and afterwards each chapter will specify how each observable is expected to contribute to the models' constraints, as well as the specific datasets used in each case.

1.8.1 SNe Ia luminosity–redshift relation

Standard candles are very valuable astrophysical objects because of their well known intrinsic luminosity. When Type Ia Supernovae (SNe Ia) started to be used in cosmology, they were praised for their homogeneity properties, which are very useful to determine astrophysical distances. These objects occur when a binary white dwarf accretes mass from its companion. As the gravitational interaction and the electrons degeneracy pressure react, it explodes when it reaches the Chandrasekhar limit, which is of 1.4 Solar masses. The explosion lasts for about a month.

For the supernovae analysis, the luminosity distance, d_{L}, is of the most relevance, and is given by

$$d_{\mathrm{L}}(z,\Theta) = c(1+z)\int_0^z \frac{dz'}{H(z',\Theta)}, \tag{1.86}$$

where c is the speed of light, and Θ holds the parameters of the specific model being constrained and the cosmology dependence of d_{L}.

The expected distance moduli, μ, of the i-th supernovae located at redshift z_{i} is given by

$$\mu^{\rm ex} \equiv m(z_{\rm i}) - M = 5\log_{10}\left[\frac{d_{\rm L}(z_{\rm i},\Theta)}{\rm Mpc}\right] + 25, \tag{1.87}$$

where m and M are the apparent and absolute magnitudes of the SNIa, respectively. Hence, one then obtains the statistical $\chi^2_{\rm SNIa}$ as

$$\chi^2_{\rm SNIa} \equiv \sum_{i=0}^{N_{\rm SNIa}} \frac{\left(\mu^{\rm ex}(z_{\rm i},\Theta) - \mu^{\rm obs}(z_{\rm i})\right)}{\sigma_{\rm i}}, \tag{1.88}$$

where $\mu^{\rm obs}(z_{\rm i})$ is the observationally measured distance moduli of the i-th supernovae, $\sigma_{\rm i}$ is the associated variance, and the sum is over all the available supernova in the dataset.

However, Phillips noted that the use of Type Ia Supernovae as standard candles should be exercised with caution. This is because these objects present a significant intrinsic dispersion in the absolute magnitude at maximum light. To correct this, Phillips used an empirical correlation to measure the decay from peak brightness (which he named the magnitude light curve from maximum light $M_{\rm max}$) to the magnitude 15 days after M-maximum (which he parametrised as Δm_{15}):

$$M_{\rm max}({\rm band}) = a + b\Delta m_{15}({\rm band}) \tag{1.89}$$

where the parameters a and b depend on the band used. Sne Ia that evolve slowly are intrinsically more luminous than those that evolve rapidly [176, 177].

Sne Ia are also correlated with colour, as would be expected if their light were extinguished by dust [177]. Krisciunas parametrised dust reddening by relating the colour excess to the visual band extinction $A_{\rm V}$,

$$A_{\rm V} = R_{\rm V}E(B-V), \tag{1.90}$$

where $E(B-V)$ is the difference of the observed colour and the unreddened colour of the Sne Ia and $R_{\rm V}$ is the ratio of total-to-selective extinction [130]. The value of $R_{\rm V}$ varies according to the galaxy and the line of sight [177].

1.8.2 Baryon Acoustic Oscillations (BAO) peak

Baryon acoustic oscillations are found in the clustering of galaxies, shown as a peak in the two-point correlation function at a comoving separation, $r_{\rm s}$, equal to the sound horizon at the drag epoch, z_{d}, when baryons were released from photons. The drag redshift z_{d} can be estimated using a fitting formula [74]

$$z_{\mathrm{d}} = \frac{1291\left(\Omega_{\mathrm{M}}\right)^{-0.419}}{1+0.659\left(\Omega_{\mathrm{M}}\right)^{0.828}}\left[1+b_1\left(\Omega_{\mathrm{b}}\right)^{b_2}\right], \tag{1.91}$$

where $\Omega_{\mathrm{M}} = \Omega_{\mathrm{DM}} + \Omega_{\mathrm{b}}$ is the sum of the present-day energy densities of dark matter and baryons; b_1 and b_2 are two fitting parameters, given by

$$b_1 = 0.313\left(\Omega_{\mathrm{M}}\right)^{-0.419}\left[1+0.607\left(\Omega_{\mathrm{M}}\right)^{0.674}\right], \tag{1.92}$$

$$b_2 = 0.238\left(\Omega_{\mathrm{M}}\right)^{0.223}. \tag{1.93}$$

The comoving sound horizon at the baryon drag epoch, r_{s}, on the other hand, can be determined by

$$r_{\mathrm{s}}\left(z,\Theta\right) = \frac{1}{\sqrt{3}}\int_0^{a(z)}\frac{dz'}{H\left(z',\Theta\right)\sqrt{1+\frac{3\rho_{\mathrm{b}}}{4\rho_\gamma}}}, \tag{1.94}$$

where $a(z) = 1/\left(1+z\right)$ and ρ_{b} and ρ_γ are, respectively, the baryon and photon energy density. The ratio between their densities is approximated as

$$\frac{3}{4}\frac{\rho_{\mathrm{b}}}{\rho_\gamma} \approx \frac{31500}{1+z}\Omega_{\mathrm{b}}h^2\left(\frac{T_{\mathrm{CMB}}}{2.7\mathrm{K}}\right)^{-4}, \tag{1.95}$$

where $h \equiv H_0/100$. Lastly, since the comoving sound horizon calculation is very sensitive to early time effects, the effect of radiation needs to be considered. Its present-day energy density is defined as

$$\Omega_{\mathrm{r}} = \frac{\Omega_{\mathrm{M}}}{1+z_{\mathrm{eq}}}, \tag{1.96}$$

where z_{eq} is the redshift at matter-radiation equality, which is approximated by

$$z_{\mathrm{eq}} \approx 25000 \times \Omega_{\mathrm{M}}h^2\left(\frac{T_{\mathrm{CMB}}}{2.7\mathrm{K}}\right)^{-4}. \tag{1.97}$$

The peak position is dependent on the ratio of the distance measure, D_{v}, and the sound horizon at the drag epoch, r_{s}. Since the latter is tightly constrained from CMB measurements, the observation of the BAO scales act as a standard ruler, allowing one to constrain the form of D_{v}, which is determined by [74]

$$D_{\mathrm{v}}\left(z,\Theta\right)=\left[\left(\int_0^z\frac{dz'}{H\left(z',\Theta\right)}\right)^2\frac{z}{H\left(z,\Theta\right)}\right]. \tag{1.98}$$

Hence, the expected distance ratio at redshift z is simply given by

$$d_z^{\mathrm{ex}}(\Theta)=\frac{r_{\mathrm{s}}(z_{\mathrm{d}},\Theta)}{D_{\mathrm{v}}\left(z,\Theta\right)}. \tag{1.99}$$

Therefore, having the observed d_{z}, one can easily compute the BAO χ^2 as

$$\chi^2_{\mathrm{BAO}}=\left(d_{z_{\mathrm{i}}}^{\mathrm{ex}}-d_{\mathrm{i}}^{\mathrm{obs}}\right)^t\left(C_{\mathrm{BAO}}^{-1}\right)_{\mathrm{ij}}\left(d_{z_{\mathrm{j}}}^{\mathrm{ex}}-d_{\mathrm{j}}^{\mathrm{obs}}\right), \tag{1.100}$$

where $\left(d_{z_{\mathrm{i}}}^{\mathrm{ex}}\left(\Theta\right)-d_{\mathrm{i}}^{\mathrm{obs}}\right)$ is the vector of the difference between the expected and theoretical values for $d_{z_{\mathrm{i}}}$, while C_{BAO} is the covariance matrix associated to the observations.

1.8.3 Cosmic Microwave Background (CMB)

In order to obtain the CMB anisotropies observed at present, the evolution of perturbations after photons begin to stream freely needs to be taken into consideration. To confront the predicted temperature anisotropies with CMB observations, the temperature perturbation Θ_l is expanded in terms of spherical harmonics [16]:

$$\Theta_l(x,\eta)=\sum_{l=1}^{\infty}\sum_{m=-l}^{l}a_{lm}(x,\eta)Y_{lm}(\hat{n}), \tag{1.101}$$

where the subscripts l and m are conjugate to a real-space unit vector $\hat{n}$ representing the direction of the streaming photons. The variance $\mathcal{C}_l\equiv\langle|a_{lm}^2|\rangle$ can be expressed in terms of the temperature field $\Theta_l(k)$ in Fourier space as

$$\mathcal{C}_l=\frac{2}{\pi}\int_0^{\infty}dk\;k^2|\Theta_l(k)|^2. \tag{1.102}$$

In Fig. 1.3, the predicted CMB temperature anisotropies $\mathcal{D}=l(l+1)\mathcal{C}_l/2\pi$ versus the multipole l together with the *Planck* 2015 dataset are shown [11]. The measured angle θ is related with the monopole l as $\theta=\pi/l$. Hence the larger scales correspond to lower values of l.

To obtain the CMB peak position analysis, it is necessary to compute the acoustic

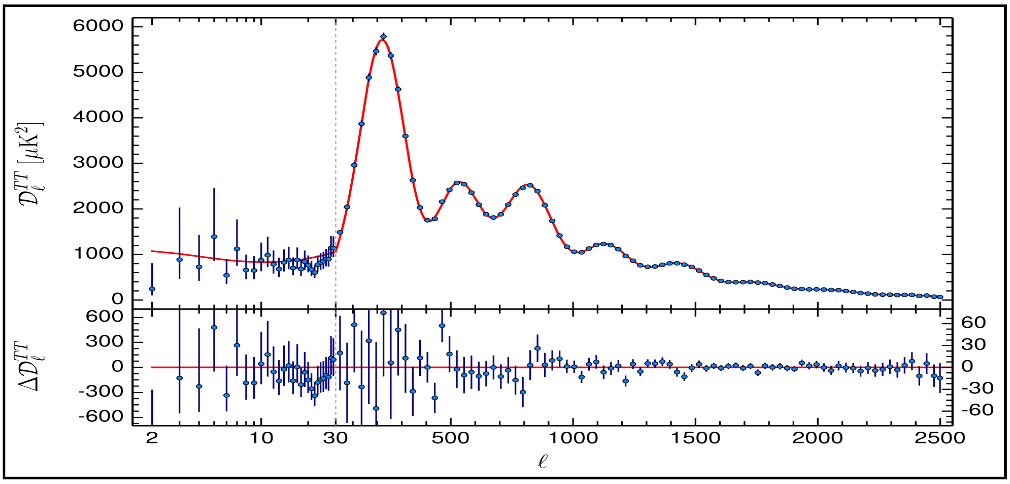

Figure 1.3 *Planck 2015 CMB spectra, compared with the base CDM fit to PlanckTT+lowP data (red line) [11]. Image credit: Planck Science Team.*

scale l_A, the "shift parameter" R, and the redshift at photon decoupling $z_\star$. The first is a measurement of the ratio of the angular diameter distance to the photon-decoupling surface over the comoving sound horizon at decoupling [222]

$$l_A(z_\star) \equiv (1+z_\star)\,\frac{\pi D_A(z_\star)}{r_{\rm s}(z_\star)}, \tag{1.103}$$

where

$$D_A(z) = \frac{1}{1+z}\int_0^z \frac{dz'}{H(z')}, \tag{1.104}$$

is the proper angular–diameter distance, and $r_{\rm s}(z_\star)$ can be calculated using Eq. (1.94). On the other hand, R is a measurement of the angular diameter distance at $z_\star$, and is given by [222]

$$R = \sqrt{\Omega_{\rm M} H_0^2}\,(1+z_\star)\,D_A(z_\star), \tag{1.105}$$

where $\Omega_{\rm M}$ is the present-day density of matter, as defined before. Lastly, the redshift at photon-decoupling can be estimated by the fitting formula [106]

$$z_\star = 1048\left[1+0.00124\left(\Omega_{\rm b}h^2\right)^{-0.738}\right]\left[1+g_1\left(\Omega_{\rm M}h^2\right)^{g_2}\right], \tag{1.106}$$

where

$$g_1 = \frac{0.0783\,(\Omega_{\rm b}h^2)^{-0.238}}{1+39.5\,(\Omega_{\rm b}h^2)^{0.763}}, \tag{1.107}$$

$$g_2 = \frac{0.560}{1+21.1\,(\Omega_{\rm b}h^2)^{1.81}}. \tag{1.108}$$

The CMB distance χ^2 is computed as

$$\chi^2_{\rm CMB} = \left(x_{\rm i}^{\rm exp} - x_i^{\rm obs}\right)^t \left(C^{-1}\right)_{\rm ij} \left(x_{\rm j}^{\rm exp} - x_{\rm j}^{\rm obs}\right), \tag{1.109}$$

where the vector $\left(x_{\rm i}^{\rm exp}(\Theta) - x_{\rm i}^{\rm obs}\right)$ measures the difference between the theoretical expectations and the observed values for the different quantities in analysis.

Numerical simulations are required to derive the complete spectra of temperature and polarisation anisotropies, primarily because the Einstein and Boltzmann equations for photons and other matter components are coupled to each other [16]. Chapters 2,4 and 5 of this thesis use the full CMB power spectrum of temperature anisotropies, whereas chapter 3 applies the measurements of the peak positions only.

1.9 Exploring the cosmological parameter space

We have now established a basic cosmological model, and referred to several of its possible extensions. We know of the existing high-quality data from the CMB, galaxy clusters, Supernovae, and other sources. This evidence allows us to place estimates and error bars on various quantitative cosmological parameters, and consequently, to address fundamental questions about the conditions of the Universe. One of the most popular engines used for this purpose is COSMOMC, a software based on the Markov Chain Monte Carlo (MCMC) technique [133]. It is mainly coded in Fortran 2008, but the attributes for sample analysis are in Python. Chapters two to six of this thesis utilised, to some extent or another, several features of this program.

In this section I describe the way this software works emphasising the features I modified to obtain the results of subsequent chapters.

Features of the tests
The information that COSMOMC will later use to initialise a search is contained

in several files of .ini termination. In them, all the parameters that will be varied are specified, along with their priors. If the user wishes to test a model that adds new variables to the baseline cosmological model they have to be defined here. Also, parameters can be set to a fixed value. This can be desirable in case a test needs to be performed fast, or if for a certain theory a parameter is being replaced by another one.

In these files the user can also choose which datasets will be required for the run. Each of them comes with its own set of nuisance parameters that are added to the existing ones in a straightforward manner by specifying an additional .ini document.

The maximum number of elements per chain to be inspected are specified here too. The test can either run until a certain degree of convergence is reached or until all the elements of every chain have been used.

CAMB

The CAMB code, which stands for Code for Anisotropies in the Microwave Background, is a fast Boltzmann program that computes the theoretical $\mathcal{C}_l$ power spectrum in order to compare CMB data with theoretical models [134]. It can be used separately from COSMOMC.

The core of the physics calculations is contained in the equations.f90 file. The code is in conformal time and the variables are expressed in units of megaparsecs. The background density variables are defined with a factor named grho $= \kappa a^2 \rho$ where $\kappa = 8\pi G$. This software implements the linear equations of the $1+3$ covariant approach to CMB anisotropies in almost-FRW models with open, flat, and closed background geometries. The perturbations are described in the synchronous gauge.

The file equations.f90 is accessed first every time CAMB gets called. As such, it is a convenient place to add any extra information required for a new test. For example, for chapter 2, a module named Quintessence was added to equations.f90 to compute the functions needed to represent dark energy as a scalar field identified by a potential given by the user.

Another important piece of code is contained in the file power_tilt.f90. This document provides the primordial super-horizon power spectrum $\mathcal{P}_{\mathrm{s}}(k)$ in the shape of a running power law. The primordial tensor power spectrum $\mathcal{P}_{\mathrm{t}}(k)$ is also provided. To obtain the results from chapter 5, the functions that specify both $\mathcal{P}_\mathrm{s}(k)$ and $\mathcal{P}_\mathrm{t}(k)$ were modified to instead being calculated using a table obtained from a spline function of the acceleration trajectory during inflation.

All the desired derived parameters of the model are specified in the file modules.f90. These are then passed on to COSMOMC identified with a number.

Connection between CAMB and COSMOMC
The file Calculator_CAMB.f90 inside the source folder of COSMOMC is the main interface between both programs. Any final changes or definitions have to be specified here because afterwards the parameters are sent to CAMB for the $\mathcal{C}_l$ power spectrum calculation.

Data analysis
The COSMOMC engine also includes the code GETDIST, which analyses the chains calculating statistics and outputs files for the requested 1D, 2D and 3D plots. This feature can also be used independently of the rest of the program, as far as the user provides the chains in .txt format and a .paramnames file with the names of all the parameters. The codes that generate the plots can be obtained in python or matlab language. The user can specify the amount of burn-in used in every analysis.

1.10 Outline of chapters 2-6

The main body of this work is composed of four paper-based chapters, themed on topics from the very early, and late Universe, and a conclusion. The format is as follows

- Chapter 2 explores a quintessence model of dark energy using the full CMB power spectrum plus BAO and Supernovae observations. This analysis used an updated version of the CAMB code that allows for a quintessence potential to be added directly. These results were published in the Journal of Cosmology and Astroparticle Physics (JCAP) [205].
- Chapter 3 deals with the background evaluation of the hybrid metric-Palatini model of gravity. The analysis was done in a personal code and GETDIST was used to sample the parameter space. These results were published in the Astrophysical Journal (ApJ) [137].
- Chapter 4 provides observational bounds on the linear perturbation analysis

of the hybrid metric-Palatini theory. The CAMB code was modified to include the sub-horizon and super-horizon approximations of this regime. A paper including these findings has been published in Physical Review D (PRD) [139].

- Chapter 5 is a study of slow-roll inflation that parametrises the acceleration history ϵ, with the aim of obtaining the minimum distance the inflaton could have evolved during this epoch, that is observationally allowed by the full range of CMB data. This is work in progress with the aim of being submitted for publication in February 2017.
- Chapter 6 summarises the main conclusions of the previously described lines of research and indicates directions for future developments.

Chapter 2

Planck Satellite Constraints on Pseudo-Nambu–Goldstone Boson Quintessence

2.1 Introduction

The most accepted cosmological constant model converges to a value of $w = -1$. However, the astrophysical observations allow a larger degree of variation from Λ's case. Therefore, it is possible that future datasets will converge to a value, close, but not exactly equal to, -1 [193].

Different theories of dark energy have arisen, and as a result, the proposition of models in which the equation of state of dark energy changes in time has been made [63]. These set of models have the added advantage of allowing for a broader phenomenology in the past evolution of DE.

It is important to notice that any new cosmological models must alleviate the coincidence and/or the fine tuning problems, or at least not make them worse, that is, research must be made in a field that can provide the missing energy between the matter and critical densities as well as drive today's cosmic acceleration, without interfering with the thermal history of the Universe [45].

One of these candidates is quintessence, an idea that was first explored in the context of inflation, the other period where the Universe underwent an accelerated expansion, albeit without dark matter sources. In these models, DE arises from a canonical scalar field ϕ minimally coupled to gravity. The slow variation of the scalar field along a potential $V(\phi)$ can lead to the very similar observational results as the cosmological constant, with the advantage of a broader phenomenology and the possibility of a link to fundamental physics models.

The application of quintessence theory to dark energy occurred first during the 1980's [80, 86, 181, 224]. Afterwards, the cosmology of quintessence was further explored, by distinguishing different behaviours and their respective equations of state and characteristic potentials [57, 62, 77, 228]. The most recent review on the subject is Ref. [218]

This chapter presents a general introduction to quintessence in Sec. 2.2, detailing everyone of the most general cases. Section 2.3 focuses on constraining a specific type of quintessence model, one with an equation of state $w \geq -1$ and characterised by a cosine potential. The results of the Bayesian analysis made in COSMOMC are explained in detail here. Previous constraints on this specific model have been performed in Refs. [55, 72, 89, 97, 117, 165]. Section 2.4 ends with some conclusive remarks.

The new results included in this chapter have been accepted for publication in an article under the same name [205]. This work was done in collaboration with my supervisor, Prof. Andrew R. Liddle. The individual and collective original contributions will be highlighted in the relevant sections.

2.2 The cosmology of quintessence

This section presents the standard results of a cosmology with quintessence, which are reproduced here in order to provide a complete introduction to the subject. Section 2.2 and the equations of Sec. 2.3.3 reproduce the work of Ref. [218].

Assuming a spatially-homogeneous quintessence field described by the scalar ϕ and its potential $V(\phi)$, the action is given by

$$S = \int d^4x\sqrt{-g}\left[\frac{1}{2}M_{\mathrm{Pl}}^2 R - \frac{1}{2}g^{\mu\nu}\partial_\mu\phi\partial_\nu\phi - V(\phi)\right] + \int d^4x\sqrt{-g}\mathcal{L}_{\mathrm{M}}, \tag{2.1}$$

where g is the determinant of the metric $g_{\mu\nu}$, R is the Ricci scalar, and $\mathcal{L}_{\mathrm{M}}$ is the Lagrangian for non-relativistic matter. M_{Pl} is the reduced Planck mass.

Varying Eq. (2.1) with respect to $g^{\mu\nu}$, the energy momentum tensor of the field is

$$T_{\mu\nu} = \partial_\mu\phi\partial_\nu\phi - g_{\mu\nu}\left[\frac{1}{2}g^{\alpha\beta}\partial_\alpha\phi\partial_\beta\phi + V(\phi)\right]. \tag{2.2}$$

From Eq. (2.2), the energy and pressure densities of the scalar field are:

$$\rho = -T_0^0 = \frac{1}{2}\dot{\phi}^2 + V(\phi), \tag{2.3}$$

$$P = T_i^i = \frac{1}{2}\dot{\phi}^2 - V(\phi). \tag{2.4}$$

And the dark energy equation of state is

$$w \equiv \frac{P_\phi}{\rho_\phi} = \frac{\dot{\phi}^2/2 - V(\phi)}{\dot{\phi}^2/2 + V(\phi)}. \tag{2.5}$$

For a matter fluid with energy density ρ_{M} and the equation of state w_{M}, the equations of motion derived from the action (2.1) are

$$\begin{aligned} 3H^2M_{\mathrm{Pl}}^2 &= \rho_\phi + \rho_{\mathrm{M}}, & (2.6)\\ 2M_{\mathrm{Pl}}^2\dot{H} &= -[\dot{\phi}^2 + (1+w_{\mathrm{M}})\rho_{\mathrm{M}}], & (2.7)\end{aligned}$$

where $H = \dot{a}/a$ is the Hubble parameter and a dot stands for a derivative with respect to t.

The continuity equation for the matter fluid is $\dot{\rho}_{\mathrm{M}} + 3H\rho_{\mathrm{M}} = 0$ and the evolution of the scalar field is given by

$$\ddot{\phi} + 3H\dot{\phi} + \frac{dV}{d\phi} = 0. \tag{2.8}$$

In order to provide an accelerating expansion, it is required that $\dot{\phi}^2 < V(\phi)$. The mechanism to obtain this condition is similar to slow roll inflation; the difference being that, for dark energy, a fraction $\Omega_{\mathrm{M}} \sim 0.3$ of the current cosmological density is non-relativistic matter, while this is absent for the inflationary case.

In spite of this inconvenience, the slow roll parameters

$$\epsilon = \frac{M_{\mathrm{Pl}}^2}{16\pi}\left(\frac{1}{V}\frac{dV}{d\phi}\right)^2, \tag{2.9}$$

$$\eta = \frac{M_{\rm Pl}^2}{8\pi}\frac{1}{V}\frac{d^2V}{d\phi^2}, \tag{2.10}$$

can still provide a helpful measure to check the existence of an accelerated expansion [188].

To develop the possible dynamical scenarios for this system, the dimensionless variables x and y are used,

$$x \equiv \frac{\dot{\phi}}{\sqrt{6}M_{\rm Pl}H} \quad , \quad y \equiv \sqrt{\frac{V(\phi)}{3}}\frac{1}{M_{\rm Pl}H}. \tag{2.11}$$

Using these expressions, the field density parameter ($\Omega_\phi \equiv \rho_\phi/3M_{\rm Pl}^2H^2$) and Eq. (2.5) can be expressed as

$$\Omega_\phi = x^2 + y^2 \quad , \quad w = \frac{x^2 - y^2}{x^2 + y^2}. \tag{2.12}$$

The effective equation of state is defined as

$$w_{\rm Eff} = -1 - 2\frac{\dot{H}}{3H^2}, \tag{2.13}$$

where the ratio $\frac{\dot{H}}{3H^2}$ is obtained from deriving Eqs. (2.6) and (2.7),

$$\frac{\dot{H}}{H^2} = -3x^2 - \frac{3}{2}(1 + w_{\rm M})(1 - x^2 - y^2). \tag{2.14}$$

Taking the derivatives of x and y with respect to $N \equiv \log a$ and using Eqs. (2.8) and (2.14),

$$\frac{dx}{dN} = -3X + \frac{\sqrt{6}}{2}\lambda y^2 + \frac{3x}{2}\left[(1 - w_{\rm M})x^2 + (1 + w_{\rm M})(1 - y^2)\right], \tag{2.15}$$

$$\frac{dy}{dN} = -\frac{\sqrt{6}}{2}\lambda xy + \frac{3}{2}y\left[(1 - w_{\rm M})x^2 + (1 + w_{\rm M})(1 - y^2)\right], \tag{2.16}$$

where λ is defined as $\lambda \equiv -M_{\rm Pl}V_{,\phi}/V$.

Eqs. (2.14) – (2.16) are useful to derive expressions to study the evolution of w and Ω_ϕ,

$$w^{'} = (w - 1)\left[3(1 + w) - \lambda\sqrt{3(1 + w)\Omega_\phi}\right], \tag{2.17}$$

$$\Omega_\phi' = -3\Omega_\phi(1-\Omega_\phi)(w - w_{\rm M}), \tag{2.18}$$

where a prime represents a derivative with respect to $N \equiv \log a$. Defining Γ as $\Gamma \equiv VV_{,\phi\phi}/V_{,\phi}^2$, the parameter λ is

$$\lambda' = -\lambda^2(\Gamma - 1)\sqrt{3\Omega_\phi(1+w)}. \tag{2.19}$$

The evolution of w varies according to different quintessence potentials and initial conditions. There are three main model possibilities: (i) tracking freezing, (ii) scaling freezing and (iii) thawing.

Here, the three cases will be introduced, but the focus of this chapter is on imposing constraints on thawing quintessence. The choice of these type of models over the freezing and scaling options will be explained throughout the forthcoming sections.

2.2.1 Tracking freezing models

Tracking fields were initially introduced under the claim of avoiding the coincidence problem. These models have an equation of motion with attractor-like solutions in which a very wide range of initial conditions rapidly converge to a common, cosmic evolutionary track [212].

In this framework, the equation of state w_ϕ varies according to the background equation of state $w_{\rm B}$. During radiation domination, $w_{\rm B} = 1/3$, then w_ϕ is less or equal (in some cases, very nearly equal) to 1/3 and the quintessence energy density ρ_ϕ decreases less rapidly than the radiation energy density. When the Universe is being dominated by matter, $w_{\rm B} = 0$, then w_ϕ is less than zero and ρ_ϕ decreases less rapidly than the matter density. Eventually, ρ_ϕ surpasses the matter density and becomes the dominant component. At this point, $w_\phi \to -1$ as $\Omega_\phi \to 1$ and the Universe is driven into an accelerated phase [212].

Although tracking is a useful form of quintessece, this concept, as introduced by Steinhardt et al. does not ensure the physical viability of quintessence in the observable Universe. It provides no control over the slow roll-down of the field, therefore, the transition to the scalar field dominated phase may take place much later than observed. Because of it, the more up-to-date tracking freezing models described by Tsujikawa et al. will be explored from now on in this text [180].

In freezing models the potential tends to be shallow at late times, resulting in the decrease of w. For the field density parameter satisfying the relation

$$\Omega_\phi = \frac{3(1+w)}{\lambda^2}, \tag{2.20}$$

w is constant from Eq. (2.17). In the matter dominated epoch, Ω_ϕ is constant in Eq. (2.18) and hence λ is constant [218]. However, if λ decreases with time the universe enters a period of cosmic acceleration. This statement implies, from Eq. (2.19)

$$\Gamma > 1. \tag{2.21}$$

The solution (2.20) in accordance to condition (2.21) is called a tracker, causing Ω_ϕ to increase and therefore $w < w_{\rm M}$ [212]. Using Eqs. (2.18) and (2.19) and neglecting the contribution of Ω_ϕ, the constant equation of state along the tracker is

$$w = w_0 \equiv \frac{w_{\rm M} - 2(\Gamma - 1)}{2\Gamma - 1}. \tag{2.22}$$

An illustrative example is the inverse power law potential [78]:

$$V(\phi) = M^{4+p}\phi^{-p}, \tag{2.23}$$

where M and $p > 0$ are constants. For this case

$$\Gamma = 1 + \frac{1}{p} \quad , \quad w_0 = \frac{-2}{2+p}, \tag{2.24}$$

satisfying the condition (2.21). The growth of Ω_ϕ implies the decrease of w_0. Hence the tracker belongs to the class of freezing models.

The solution (2.22) was obtained by considering $\Omega_\phi \ll 1$. To take into account the variation of w, the perturbation to the $0-th$ order solution is used [54], by dealing with Eqs. (2.20) and (2.22)

$$a^2\frac{d^2\delta w}{da^2} + a\frac{5-6w_0}{2}\frac{d\delta w}{da} + \frac{9}{2}\delta w(1-w_0) - \frac{9}{2}w_0\Omega_\phi(a)(1-w_0^2) = 0, \tag{2.25}$$

where Γ was assumed constant. For $\Omega_\phi(a)$ the $0-th$ order solution is

$$\Omega_\phi(a) = \frac{\Omega_\phi a^{-3w_0}}{\Omega_\phi a^{-3w_0} + 1 - \Omega_\phi}, \tag{2.26}$$

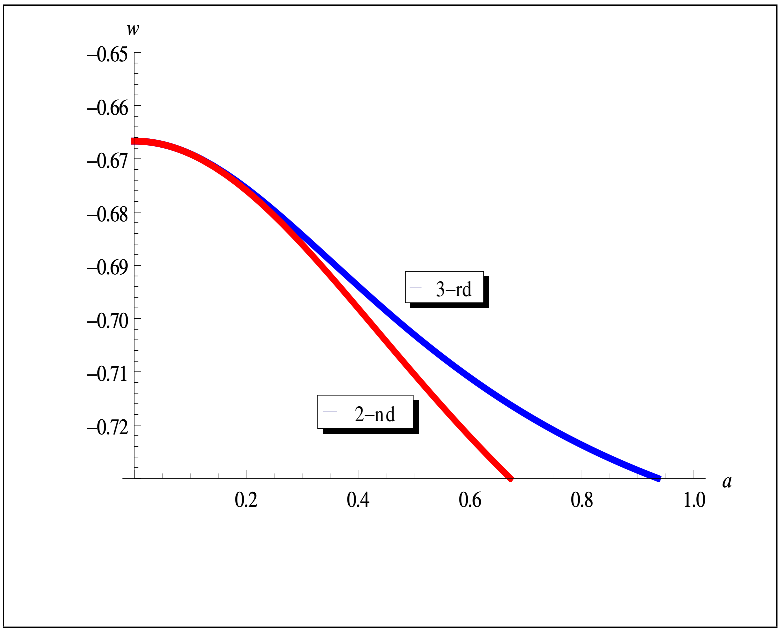

Figure 2.1 *The quintessence equation of state* w *versus* a *for the potential* $M^5\phi^{-1}$ *to second (blue) and third (red) order of Eq. (2.27).*

Substituting Eq. (2.26) into Eq. (2.25) the integrated solution is [54]

$$w(a) = w_0 + \Sigma_{n+1}^{\infty}\left[\frac{(-1)^{n-1}w_0(1-w_0^2)}{1-(n+1)w_0+2nw_0^2(n+1)}\frac{\Omega_\phi(a)}{1-\Omega_\phi(a)}\right]^2. \qquad (2.27)$$

In Fig. 2.1 the numerical evolution of w versus a for the potential (2.23) with $p = 1$ is plotted. The observational constraints for this model have been analysed in Refs. [55, 221], using data from the joint analysis of Union 2.1 [216] for Supernovae, the cosmic microwave background anisotropies from WMAP7 [214], baryon acoustic oscillations data from BAO SDSS7 [173] and BOSS [115], indicating that the tracker equation of state during the matter era is constrained to be $w_0 < -0.964$ (95% CL) under the prior $w_0 > -1$. For the potential (2.23) this translates as $p < 0.075$.

By setting a prior $w_0 > -1$, Ref. [221] found the best-fit model to be $w_0 = -1$. When tests are carried out without this prior, the data favour the value $w_0 = -1.097$. This is one of the reasons why the project on which this chapter is based on did not consider updating the constraints on a model resulting Eq. 2.23 or another of similar tracking properties. If the condition $w < -1$ is violated, the model is not considered to be quintessence any more.

2.2.2 Scaling freezing models

These models can be considered as a special case of the tracker along which $\Omega_\phi = 3(1+w)/\lambda^2$ is constant [62, 77]. They are characterised by double exponential potentials [24]

$$V(\phi) = V_1 e^{-\lambda_1 \phi / M_{\rm Pl}} + V_2 e^{-\lambda_2 \phi / M_{\rm Pl}}, \tag{2.28}$$

where $\lambda_{\rm i}$ and $V_{\rm i}$ are constants. During the radiation era ($w = 1/3$) the constraints give the bound $\Omega_\phi < 0.045$ which translates into $\lambda_1 > 9.4$. The scaling matter era ($w = 0$) is followed by cosmic acceleration, where the dominance comes from the exponential with λ_2 in the argument.

The transition from the scaling matter to the present epoch depends on the parameters λ_1, λ_2, V_1 and V_2. The variation of w can be accommodated by using the parametrisation [143]

$$w(a) = w_{\rm f} + \frac{w_{\rm p} - w_{\rm f}}{1 + \left[\frac{a}{a_t}\right]^{1/\tau}} \tag{2.29}$$

where $w_{\rm p}$ and $w_{\rm f}$ are values of w in the past and future respectively, $a_{\rm t}$ is the scale factor at the transition and τ is the transition width.

In Fig. 2.2 the numerical evolution of w versus a for values of $a_{\rm t}$ and τ within the 95% contour level are plotted. In Ref.[55] the joint analysis of Union 2.1, WMAP7 and BAO (SDSS7, BOSS) was done using $\tau = 0.33$. The constraints founded were $a_{\rm t} < 0.23$ (95% CL), $\lambda_1 > 11.7$ and $\lambda_2 < 0.539$. As explicit from the figure, w needs to approach -1 quite early on in the cosmological evolution. This means the effects of DE would potentially be felt at a much higher redshift, a feature that has not been measured. Also, models with $\lambda_2 \geq 0.5$ cause a very strong deviation from -1.

2.2.3 Thawing models

In this type of quintessence the potential must be able to mimic a nearly-frozen field during the matter-dominated era, caused by Hubble friction, implying w near -1 at early times. Its kinetic energy contribution must be kept small, which means a small mass is required as well as a nearly-flat potential. The

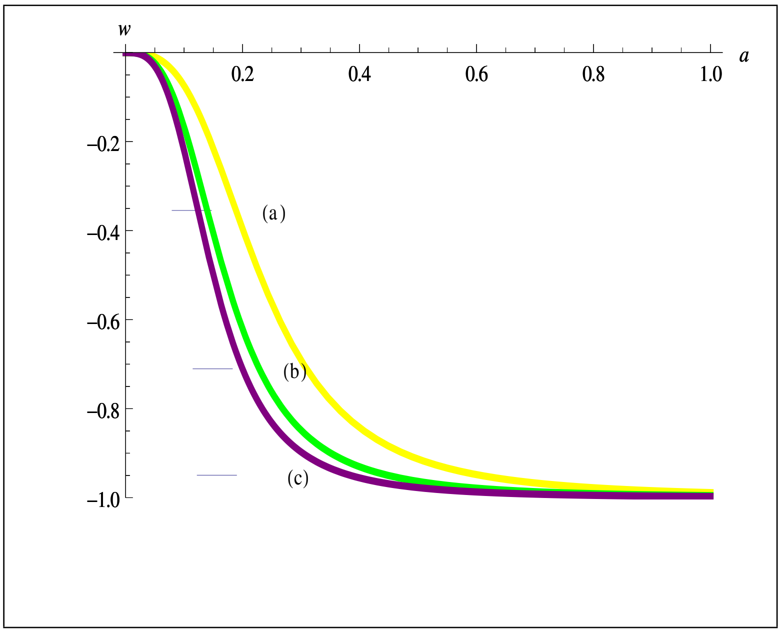

Figure 2.2 *The quintessence equation of state w versus a for $\lambda_1 = 9$, $\lambda_2 = 0.9$. Each curve corresponds to: (a) $a_{\rm t} = 0.23$, $\tau = 0.33$; (b) $a_{\rm t} = 0.17$, $\tau = 0.33$; (c) $a_{\rm t} = 0.15$, $\tau = 0.32$.*

following sections are the main original contribution of this chapter, and in them the constraints for a specific potential of the thawing type are analysed. The results obtained for the free parameters of this model are the most up-to-date observational bounds for this theory.

2.3 PNGB quintessence

The theory described by the pseudo Nambu - Goldstone - Boson potential fits all the conditions of a thawing type quintessence theory [85]. It is characterised by a cosine type equation

$$V(\phi) = V_0 \left[1 + \cos\frac{\phi}{f}\right] , \tag{2.30}$$

where $V_0 = \rho_{\rm c}\, M^4$ and f are the normalisation and the width of the potential, respectively. These two parameters, as well as the initial conditions $\phi_{\rm i}$ and $\dot{\phi}_{\rm i}$ determine the cosmological evolution of this model. This set of variables can be simplified given the rapid early expansion of the Universe, which leads to sharply-decaying field velocity at early times. As a result, $\dot{\phi} = 0$ is the initial condition for the numerical evolution. Figure 2.3 shows some sample evolutions of the equation of state obtained numerically for cases with present density parameter $\Omega_\phi = 0.68$.

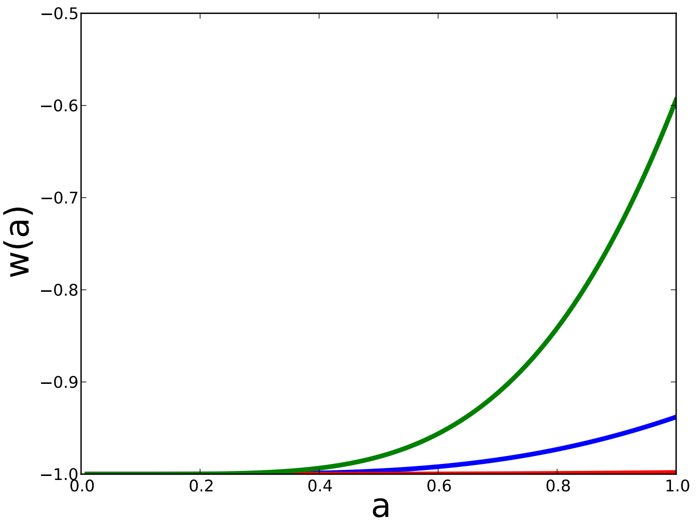

Figure 2.3 *Equation of state versus scale factor for the PNGB potential with* $f = 1.4M_{\rm Pl}$*, for models leading to present values* $w_0 = -0.99$ *(red),* $w_0 = -0.93$ *(blue) and* $w_0 = -0.6$ *(green). In thawing quintessence,* $w \geq -1$*.*

Requiring that at present the quintessence field has a particular density parameter Ω_ϕ allows the use of the density parameter as a variable. In turn, $\phi_{\rm i}$ is treated as a derived parameter. The background evolution is calculated from a scale factor $a = 10^{-9}$.

By definition, thawing models always present $w_0 \geq -1$, a characteristic that makes them very interesting to study, as one needs not to worry about phantom dark energy.

Good quintessence candidates are ideally required to generate a flat potential protected from radiative corrections in a natural way. In this regard, the PNGB axions are successful: these fields have a flat potential as a result of a shift symmetry, that is, the potential is unchanged under the transformation $\phi \rightarrow \phi + \text{constant}$. During the early Universe, the axion rolls along this flat potential for a very long time, in accordance to the expected effect of dark energy during the radiation and matter domination epochs. The shift symmetry is eventually broken to allow DE to roll to a minimum of the potential and generate the accelerating expansion of the Universe [81, 82].

2.3.1 PNGB potential analysis with COSMOMC

It is therefore the aim of this chapter to undertake a MCMC exploration of the parameter space of PNGB quintessence. This study was made using the COSMOMC program, version July 2015 [133]. Within the CAMB program the quintessence module was updated by myself, with support from Prof. Liddle, to be compatible with the CAMB/COSMOMC version of July 2015. Additionally, a modification of the original code was implemented to solve a starting point issue: in order for the evolution to commence, the amplitude of the potential has to be large enough to allow the quintessence density parameter Ω_ϕ to have a value corresponding to the observed dark energy density. The random search nature of the MCMC code (at least at the beginning of the parameter space exploration) caused the program to stop through failing to meet this condition, therefore not allowing the code to calculate a likelihood. Instead of stopping the code after an unsuccessful initial setting, the unsuitable parameters were assigned an improbable negative logarithmic likelihood of 10^{30} (the standard value for the algorithm to deem a set of parameters unlikely) therefore rejecting them but allowing the rest of the estimations to continue.

The choice of prior ranges for the standard cosmological parameters were taken as in the *Planck* collaboration 2015 analysis [8]. These, as well as the added free components that characterise the PNGB model, are displayed in Table 2.1. Additionally, the range imposed on H_0 is $50\,\mathrm{km\,s^{-1}\,Mpc^{-1}} \leq H_0 \leq 80\,\mathrm{km\,s^{-1}\,Mpc^{-1}}$.

When the idea of dark energy began to appear, followed a couple of years later by the idea of quintessence as a specific DE model, string theory seemed the only context where the extremely flat potentials necessary for its realisation were possible. This is because, in string theory, axions appear naturally [70].

It is possible to write down a virtually infinite number of quintessence potentials $V(\phi)$. However, only for few of them the flatness of the potential is not spoiled by radiative corrections. Therefore, a theoretical prejudice in favor of radiatively stable potentials is what motivated the early studies of axion-type models in a dark energy context [72].

Axion like fields, with decay constants f larger than the Planck scale, could give rise to models of natural inflation. Such scenarios can only be studied in a framework where Planck scale physics is under control. This is the case in certain extreme regions of the moduli space of string/M theory [22].

A variety of regions in string moduli space where a large f could arise have been investigated, but no consistent scenario of this type has been found. In some cases, the decay constant can be parametrically larger than the Planck scale but the effective action then contains appreciable harmonics of order $f < M_{\rm Pl}$. As a result, these fields are no better inflaton candidates than Planck scale axions. Therefore, the stand of particle physics is that the axions' decay constant must respect $f < M_{\rm Pl}$ [22]. As will be shown later, models with $f < M_{\rm Pl}$ are not favoured by dark energy. It is rather $f \ll M_{\rm Pl}$ and $f \geq M_{\rm Pl}$ that are.

Previous related works [4, 72] have imposed a hard limit on the width of the potential of $f < M_{\rm Pl}$, citing both computational reasons (avoiding a divergent direction for the MCMC chains to reach convergence) and theoretical ones, such as inaccuracy of the described potential for $f > M_{\rm Pl}$ and motivations from string theory. Referring to the latter, the PNGB potential has been used with the purpose of understanding natural inflation better.

One of the main points of this approach has focused on the different values of the potential's width $f/M_{\rm Pl}$, in the context of supersymmetry/superstring theories. The overall conclusion favours $f < M_{\rm Pl}$ [4, 22]. However, a somewhat weaker prior $f < 2M_{\rm Pl}$ was imposed here, by which time the potential is flat enough that it can commonly generate observables practically indistinguishable from those for ΛCDM. Our motivation to do this is because supersymmetric theories have recently become less compelling, given the lack of evidence in their direction, and moreover the PNGB potential offers a phenomenological description of dark energy that is well behaved, independently of the use of axions during the inflationary epoch. The outcome from choosing alternative priors for f will be studied later.

To obtain the observational bounds the data utilised was the JLA compilation of supernova distances [29], cosmic microwave background temperature anisotropies, lensing and polarisation data from the *Planck* 2015 data release [8, 11], direct constraints on the Hubble constant from Hubble Space Telescope observations [184], and baryon acoustic oscillations data from SDSS [185].

2.3.2 Constraints

The probability distributions results presented in this and the following sections of the chapter were obtained by myself, with the guidance of my supervisor,

Parameter	Prior range
$f/M_{\rm Pl}$	[0.1, 2]
M^4	[0.25, 2]
$\Omega_{\rm b}h^2$	[0.005, 0.1]
$\Omega_{\rm c}h^2$	[0.001, 0.99]
$n_{\rm s}$	[0.8,1.2]
τ	[0.01, 0.8]
$100\theta_{\rm MC}$	[0.5, 10]
$\ln(10^{10}A_{\rm s})$	[2, 4]
w_0	...
Ω_ϕ	...
$\phi_{\rm i}/f$	...

Table 2.1: Prior ranges for cosmological and PNGB model parameters, the prior being uniform in the parameter quoted. The meaning of the cosmological parameters is as in the *Planck* collaboration papers [8, 11]. The final three parameters listed are derived from the others and inherit non-uniform priors from their relation to them.

Andrew Liddle. We then analysed these results together.

The free parameters of this analysis, aside from those standard in any cosmological model, are the width f and the amplitude M^4 of the potential (2.30). The CAMB code uses dimensionless versions of the field and width parameter, but here they will be refer to in their native units of mass. The code's background evolution computation handles all energy–momentum components with a normalisation equivalent to $8\pi G\rho_{\rm crit}/3c^2$ where $\rho_{\rm crit}$ is the present value of the critical density. The matter energy constituents are then multiplied using the standard density parameter definition $\Omega_{\rm i} = \rho_{\rm i}/\rho_{\rm crit}$ where the index i is matter or quintessence. This means that M^4 and $V(\phi)$ are, regarding their units, equivalent to the density parameter for the quintessence field Ω_ϕ.

Figure 2.4 depicts an ensemble of trajectories for the equation of state w versus scale factor a of the PNGB model, drawn from both the prior and posterior distributions. We see a very strong tightening of the posterior distribution with respect to the prior, indicating that the data are significantly constraining the considered set of models.

In Fig. 2.5, a triangular plot with the 68% and 95% confidence contours between the amplitude M^4, the width $f/M_{\rm Pl}$, the field density parameter Ω_ϕ, the present value of the field equation of state w_0 and the initial displacement of the field $\phi_{\rm i}/f$ is displayed. The individual posterior distributions of each parameter are

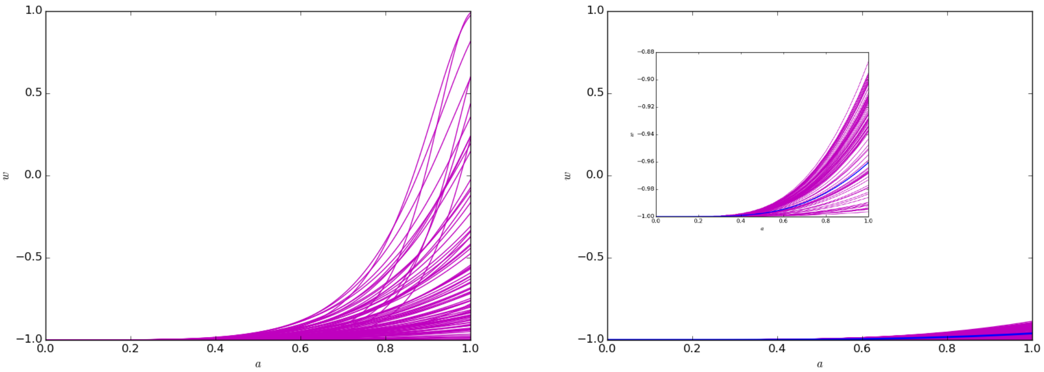

Figure 2.4 *Density plots for the equation of state w versus scale factor a of the PNGB model. The figure on the left depicts random prior choices from Table 2.1. On the right, a sample of the posterior distribution models obtained from the combined JLA + BAO + HST + Planck 2015 datasets is shown. The best-fit model is drawn in red, and a zoom is included to show the detail of the posterior trajectories given their closeness on the original axis range.*

also shown.

The parameter $f/M_{\rm Pl}$ is unconstrained at the upper edge of its prior, and has 68% and 95% confidence lower limits of 1.34 and 0.67 respectively. For M the 68% and 95% confidence ranges are $M = 0.87^{+0.02}_{-0.12}$ and $M = 0.87^{+0.15}_{-0.15}$. These probability distributions are expected. As f grows the potential flattens, returning the cosmological constant case, which makes it impossible to confine this parameter at its upper value, while M^4 is sharply cut off at the lowest value able to sustain an allowable present density parameter, while fitting the data well at that value. Note however that the quoted lower limits on f depend strongly on the assumed *upper* limit of its prior, as models beyond the adopted prior continue to fit the data well. A detailed analysis of prior dependence will be made later on.

The density parameter Ω_ϕ is constrained at 68% and 95% confidence as, $\Omega_\phi = 0.69 \pm 0.01$ and $\Omega_\phi = 0.69^{+0.01}_{-0.02}$ respectively. The 95% upper limit on the present equation of state is $w_0 = -0.88$, whilst the lower cut-off of $w_0 = -1$ reaffirms the cosmological constant limit of this theory. This range is as expected for thawing quintessence; while values of the present equation of state bigger than -1 have been permitted, allowing non-trivial past dynamics for dark energy, the cosmological constant case gives a very good fit to the astronomical data.

Examination of $\phi_{\rm i}/f$ gives a criterion for the slope of the potential at the start of

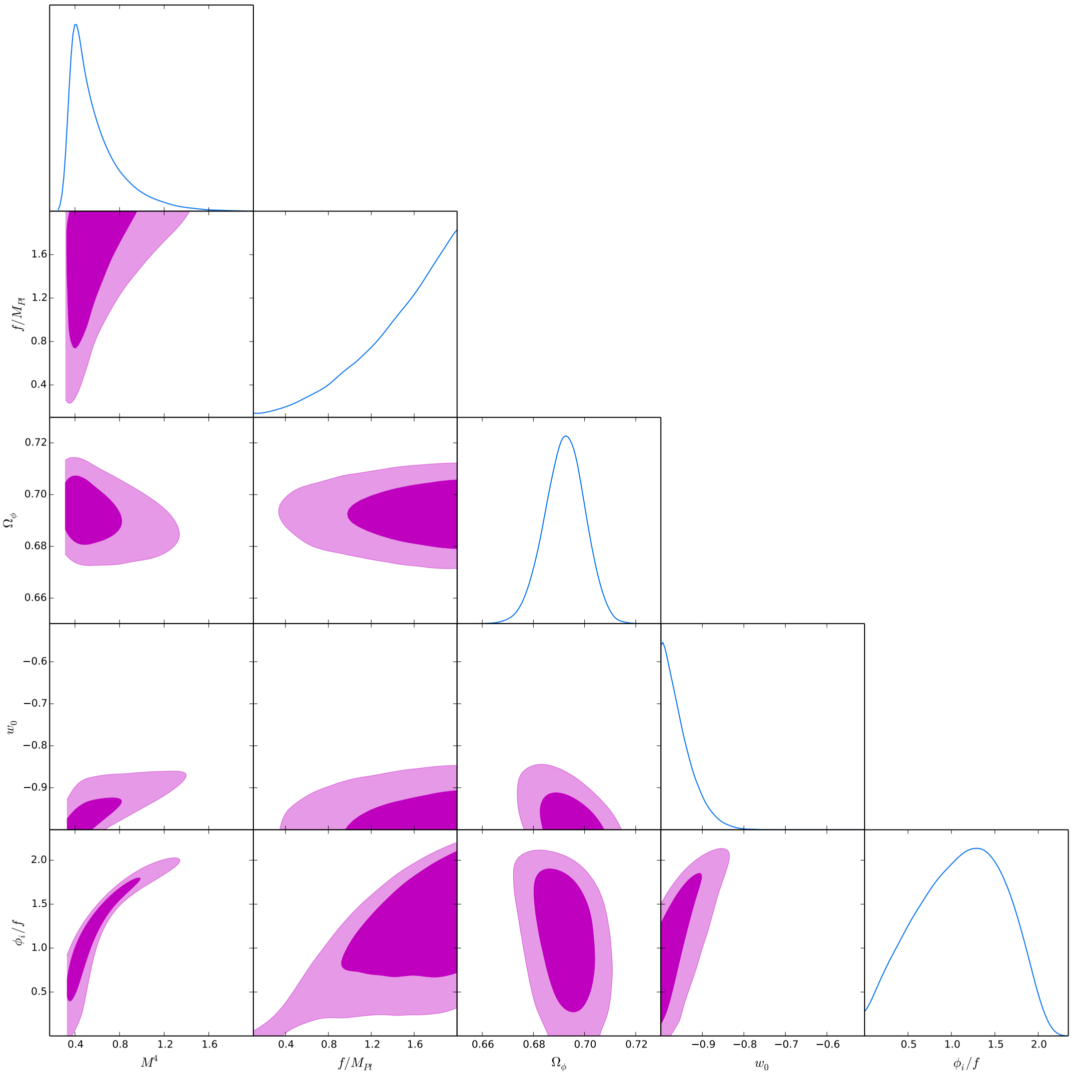

Figure 2.5 *2D contours of the combined JLA + BAO + HST + Planck 2015 constraints for the PNGB model with potential Eq. (2.30). The individual marginalised posterior probability distributions of each parameter are also shown.*

the cosmological evolution. For $\phi_{\rm i}/f \approx 0$ the feature at the bottom left corner of the ($f/M_{\rm Pl}$, $\phi_{\rm i}/f$) duplet shows that only narrow potentials (those corresponding to small f) are allowed. In such a steep regime, a slope slightly different from zero would cause the quintessence field to evolve too quickly, therefore not reproducing a thawing behaviour. Once the slope increases to $\phi_{\rm i}/f \approx 0.3$ most of the f range is enabled. Larger values for $\phi_{\rm i}/f$ are favoured when f is larger. The 95% upper limit of the starting slope is $\phi_{\rm i}/f = 1.9$, while there is no lower limit since $\phi_{\rm i}/f = 0$ reproduces ΛCDM precisely. The upper boundary value shows there is a fair range of models permitted with an evolving scalar field. However this regime is typically not well recovered except for narrow potentials with $f \approx 0$, because in order to attain such it is also necessary for M^4 to be very close to $\Omega_{\rm v}$, meaning only a narrow sliver of prior space is available. The data clearly favour the direction of increasing f.

2.3.3 Thawing quintessence: equation of state parametrisation

In line with the tracking and freezing cases, there exists an approximate equation of state solution for thawing quintessence [53, 73, 218].

Considering the case in which the field initially exists around $\phi = \phi_{\rm i}$, the scalar field is redefined as

$$\phi(t) = \frac{u(t)}{a(t)^{3/2}}. \tag{2.31}$$

Taking the derivatives of (2.31) and using Eqs. (2.6) and (2.7),

$$\ddot{u} + \frac{3}{4} u \rho_\phi + a^{3/2} V' \left(\frac{u}{a^{3/2}} \right) = 0. \tag{2.32}$$

Eq. (2.32) is exact. However, certain approximations can be applied to it; for instance, if $w \sim -1$, this implies $P_\phi \sim \rho_\phi \sim -V(\phi_{\rm i})$. Also if a Taylor expansion is performed on the potential and taken up to second order, Eq. (2.32) can be reinterpreted as

$$\ddot{u} - w^2 u \simeq -a^{3/2} V_{,\phi}(\phi) \tag{2.33}$$

where

$$w = \sqrt{\frac{3}{4} \frac{V(\phi_{\rm i})}{M_{\rm Pl}^2} - V_{,\phi\phi}(\phi_{\rm i})}, \tag{2.34}$$

with solution

$$u = A \sinh(kt) + B \cosh(kt). \tag{2.35}$$

Another consequence of taking $w \simeq -1$ is that the evolution of the scale factor can be approximated as that of the ΛCDM model

$$a(t) = \left(\frac{1 - \Omega_\phi}{\Omega_\phi}^{1/3} \right) \sinh^{1/3} \left[\frac{t}{t_\Lambda} \right] \quad , \quad t_\Lambda = \frac{2 M_{\rm Pl}}{\sqrt{3 V(\phi)}}. \tag{2.36}$$

Applying the last results to the integration of u and and using the dark energy

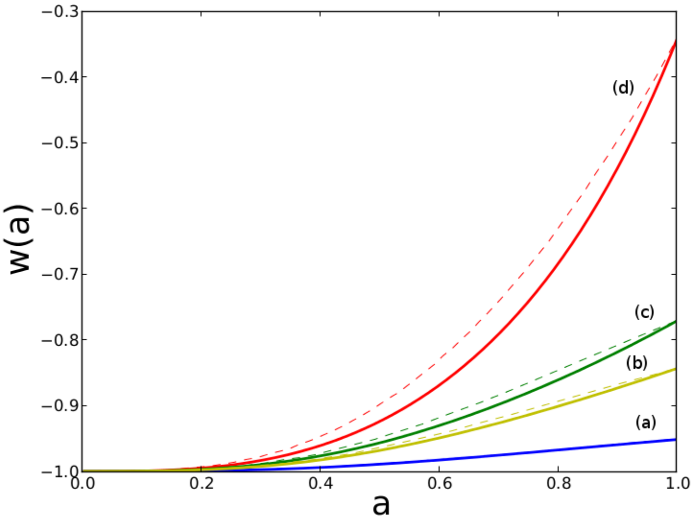

Figure 2.6 *Equation of state versus scale factor for the quintessence field equation of state (solid lines) and Eq. (2.37) (dashed lines) with* $\Omega_\phi = 0.68$*. The parameter values in each case are (a)* $f/M_{\rm Pl} = 2$*,* $\phi_{\rm i}/f = 1.65$*,* $K = 0.98$*,* $w_0 = -0.95$*; (b)* $f/M_{\rm Pl} = 1.1$*,* $\phi_{\rm i}/f = 1.52$*,* $K = 1.02$*,* $w_0 = -0.84$*; (c)* $f/M_{\rm Pl} = 0.9$*,* $\phi_{\rm i}/f = 1.43$*,* $K = 1.09$*,* $w_0 = -0.77$*; (d)* $f/M_{\rm Pl} = 0.5$*,* $\phi_{\rm i}/f = 0.94$*,* $K = 1.72$*,* $w_0 = -0.34$*.*

equation of state with the approximations taken before,

$$\begin{aligned} w(a) &= -1 + \\ &(1+w_0)\, a^{3(K-1)} \left[\frac{(K - F(a))(F(a)+1)^K + (K + F(a))(F(a)-1)^K}{(K - \Omega_\phi^{-1/2})(\Omega_\phi^{-1/2}+1)^K + (K + \Omega_\phi^{-1/2})(\Omega_\phi^{-1/2}-1)^K} \right]^2, \end{aligned} \tag{2.37}$$

where

$$K = \sqrt{1 - \frac{4M_{\rm Pl}^2 V_{,\phi\phi}(\phi_{\rm i})}{3V(\phi_{\rm i})}}, \tag{2.38}$$

$$F(a) = \sqrt{1 + (\Omega_\phi^{-1/2} - 1)a^{-3}}. \tag{2.39}$$

The equation of state (2.37) is expressed in terms of three parameters: Ω_ϕ at present, w_0, and K which measures the curvature of the scalar field potential at its maximum [218]. For K larger than 10 the movement of the field at the start of the evolution is required to be very small to avoid a quick roll down. If the field touches the minimum of the potential and starts oscillating at a scale factor value near today's, numerical simulations establish that Eq. (2.37) is not valid anymore. In addition to this inaccuracy, for an oscillating potential the equation of state would become positive, therefore violating the $w < -1/3$ condition for a dark energy description. For K smaller than 0.5 the field mass becomes very large, implying that the Taylor expansion around $\phi = \phi_\mathrm{i}$ becomes inaccurate because of the rapid variation of the field. This work places a particular focus on finding a confidence range for the curvature of the potential K that is better constrained than in past analyses by making use of the exact results in Sec. 2.3.2.

In Fig. 2.6 the behaviour of the thawing equation of state against the numerical solution provided by the quintessence module of CAMB is compared. The approximation works very well for $w_0 \approx -1$ and $K \approx 1$, but becomes less accurate for larger values of w_0 which in turn correspond to smaller values of K. If instead the curves generated by Eq. (2.37) had been adjusted to the best-fit values of K and w_0, a more varied set of parameters would have possibly been found, which would be able to duplicate a broader set of solutions.

In Fig. 2.7 the confidence contours for the curvature parameter K are shown. The 95% constraint obtained is $K = 1.1 \pm 0.4$, where K was calculated as a derived parameter from the results of Sec. 2.3.2. Given the condition within the CAMB module Quint to attain convergence of Ω_ϕ before allowing the evolution of ϕ_i to commence, the width of the potential dictates the value of the curvature. As discussed in Sec. 2.3.6, the distribution of K values that emerges from simulating the PNGB potential is far from uniform, and hence the present constraints appear very different from those that sample uniformly in w_0 and K such as Ref. [55].

Now the results of Secs. 2.3.2 and 2.3.3 are placed into context by comparing them to results under different choices of datasets and parameter priors. A comparison between these results and those of previous authors in the subject of thawing quintessence is also included.

2.3.4 Constraints using *Planck* 2015 only

The results of the full-mission *Planck* observations of temperature and polarisation anisotropies of the CMB radiation are widely considered to be the most reliable dataset for constraining cosmological models. Moreover, for the standard six-parameter cosmological model they are sufficient on their own to fix all the parameters accurately. Here the aim is to test whether this latter statement

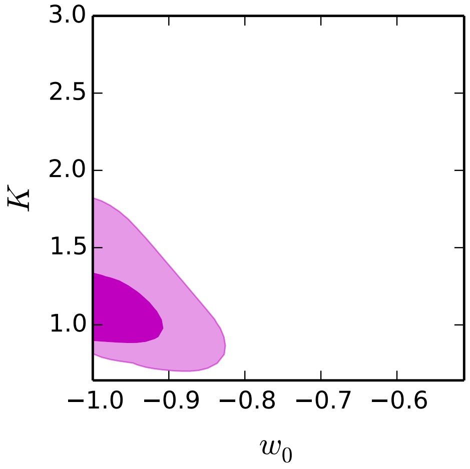

Figure 2.7 *The 68% and 95% confidence level regions for* (w_0, K) *given by Eq. (2.38).*

remains true with the more general dark energy model by comparing results using *Planck* 2015 only with those of the full dataset described earlier. In Fig. 2.8 a triangular plot with the 68% and 95% confidence contours using the *Planck* dataset is shown. The parameters displayed are the same as those of Fig. 2.5, but note that in some cases the axis ranges have had to be extended.

Typically the constraints obtained by this particular analysis are considerably weaker than those of Sec. 2.3.2. The most striking example of this is the width of the potential $f/M_{\rm Pl}$; the *Planck* data alone are unable to constrain this within the prior at a confidence range of 95%. A somewhat better constraint is attained for the amplitude of the potential M, where at 68%, $M = 1.02^{+0.06}_{-0.04}$. This result is linked to the field density parameter limit of $\Omega_\phi = 0.64^{+0.05}_{-0.01}$, because of these two quantities' relation in the convergence of the code as mentioned in Sec. 2.3.1. There is a noticeable drop in the mean value of Ω_ϕ against the full dataset result of $\Omega_\phi = 0.69$; as models with a lower potential amplitude are accepted and the field is allowed to roll for a wider variety of initial conditions.

Most notably, the present value of the equation of state is not well determined, with a 95% confidence upper limit of $w_0 < 0.27$. This result is not very useful for a quintessence scenario, given that it does not even require the condition of $w_0 < -1/3$ for a Universe in accelerated expansion at present. There is also an unexpected portion of model space around $w_0 = +1$, which is not compatible with broader datasets. The conclude is that a CMB-only analysis of the PNGB model is insufficient to distinguish between the permitted parameter combinations, and hence it is necessary to include the geometric data compiled at much lower redshift

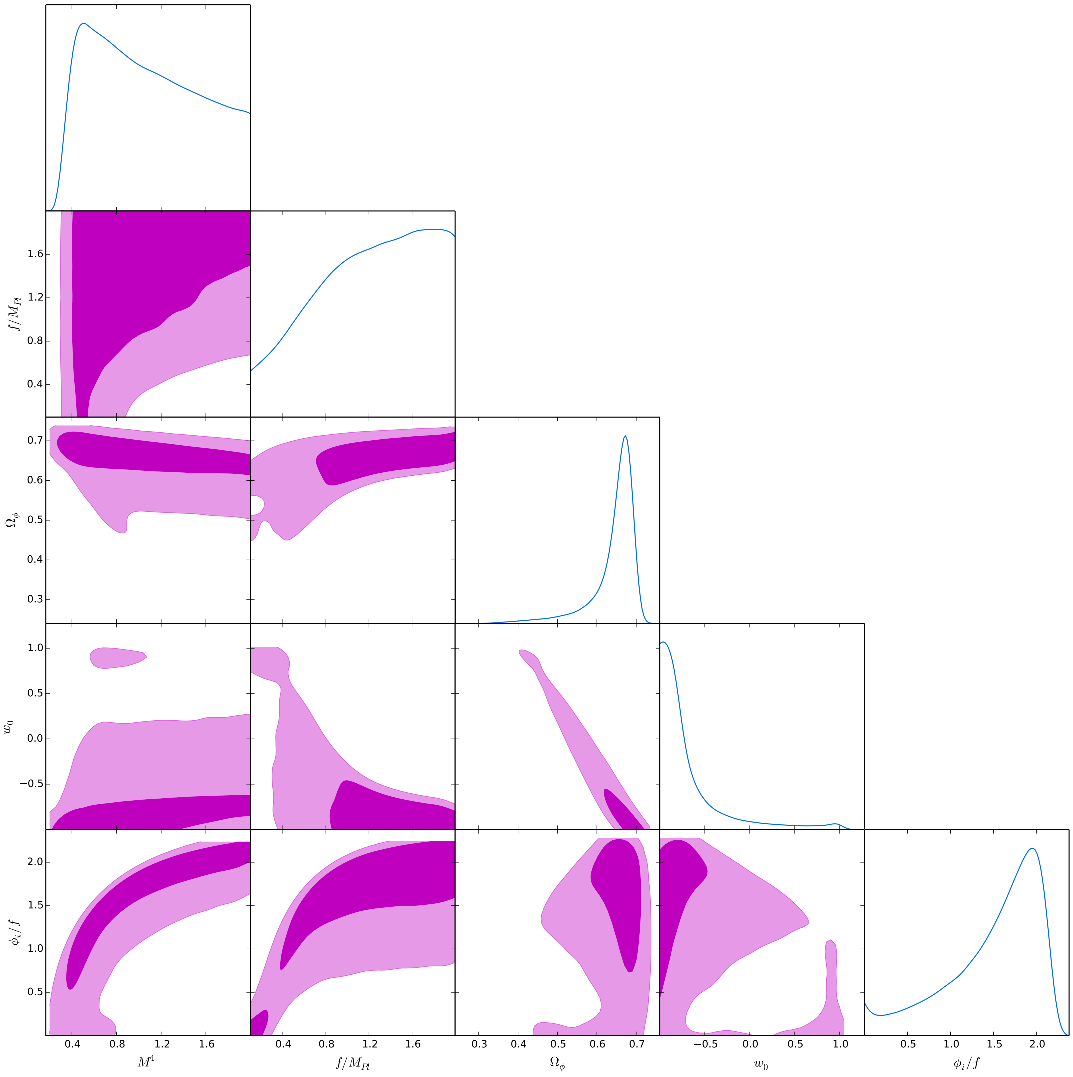

Figure 2.8 *The 2D contours of the Planck-only constraints for the PNGB model with potential Eq. (2.30).*

values. This was found also in Ref. [9] for the (w_0,w_a) parametrisation of dark energy.

2.3.5 Choice of inverse prior for the PNGB potential width

In light of the data's inability to constrain high values of f, the prior dependence of these results was assessed. First, an analysis which simply extended the upper limit of the uniform prior on f to 4 instead of 2 was performed, which just had the effect of admitting extra models at the higher values of f which make predictions very similar to the cosmological constant. As the prior contains more models of this type, constraints on models away from this limit tighten somewhat, which already indicates a significant prior dependence to any constraints which are quoted.

More importantly, however, there is no particular motivation for choosing a prior uniform in f, which did not allow for a clear discrimination between models with a narrow width of $f/M_{\rm Pl} < 1$. In order to explore the parameter with uniform prior was changed from $f/M_{\rm Pl}$ to $1/(f/M_{\rm Pl})$. The new prior choice was $(10^{-4}, 5)$, leaving the rest of the analysis parameters with the same meanings as in Sec. 2.3.2. This then means that the cosmological constant limit occupies a finite region of parameter space near $1/f \simeq 0$, rather than the potentially-infinite region when placing a uniform prior on f.

This choice is equivalent to a logarithmic parametrisation; for instance, the upper end of the uniform prior $\log f = 2.0 = 0.301$, which is similar to the upper end of the present prior. The testing of these different priors was Liddle's idea, in order to strengthen the analysis we had performed previously, with data from the *Planck* 2013 release.

Figure 2.9 shows the results of this new choice of prior, where $1/(f/M_{\rm Pl}) = 2.3$ is the upper limit found at a 95% confidence level. This corresponds to a limit on f which is not very different to the one found in Sec. 2.3.2, though of course the changed prior modifies the overall shape of the posterior. The lower prior limit of 10^{-4} is close to zero, and therefore indistinguishable by the data due to its closeness to the cosmological constant case. In a similar fashion to Fig. 2.5, the model's preference is for becoming indistinguishable from the prior at large f (corresponding to the cosmological constant case), a feature that is only cut out from limiting the prior itself.

The rest of the probability distributions are in good agreement as those of Sec. 2.3.2, indicating that they do not have much sensitivity to the choice of prior. The present equation of state w_0 is a good example of this insensitivity, its limit changing only slightly. However, the potential amplitude M^4 does become less constrained at its upper values. This is because the present alternative prior places less prior weight on models which are very cosmological-constant-like, hence permitting a somewhat wider range of M^4 than the original prior choice.

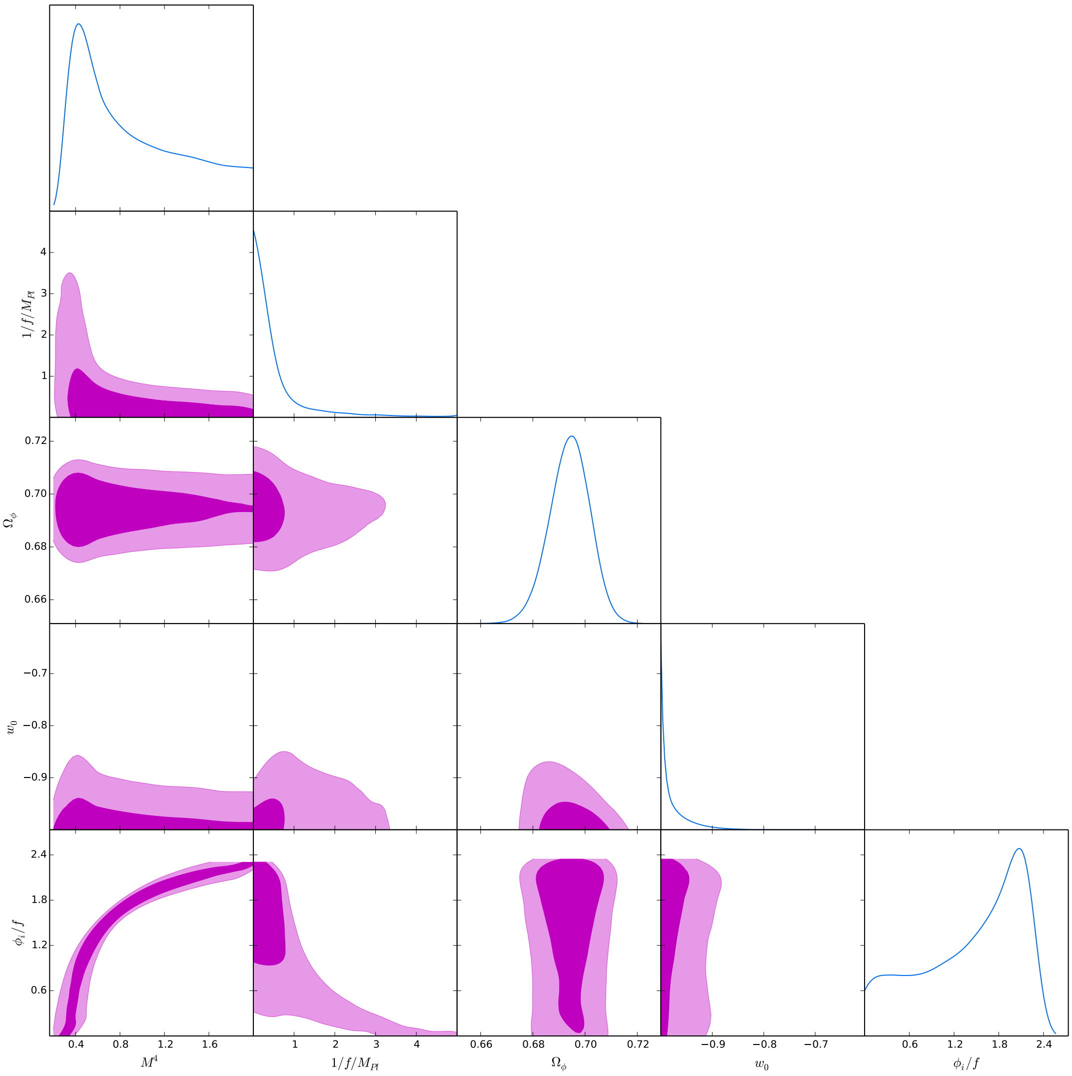

Figure 2.9 *The 2D contours of the combined JLA + BAO + HST + Planck 2015 constraints for the PNGB model with potential Eq. (2.30) and parametrisation uniform in* $M_{\rm Pl}/f$ *instead of* $f/M_{\rm Pl}$*. The rest of the parameter definitions are the same as in Fig. 2.5.*

2.3.6 Comparison with previous results

In this section, the present results are compared to those of previous authors. Similar studies to Fig. 2.5 can be found in Refs. [4, 72, 117, 165] and comparison is straightforward after noting a recurrent difference in the definition of the variable M^4 between those works and the one introduced in this chapter. As a typical example, Fig. 2 in Ref. [72] plots

$$\left[\frac{f}{10^{18}\,\mathrm{GeV}}, \frac{\mu}{\sqrt{h/0.65}\times 10^{-3}\,\mathrm{eV}}\right], \tag{2.40}$$

where μ^4 is the amplitude of the potential, h is the Hubble parameter and f is the width of the potential, same as in our case. This choice arises from the fact that the value of the critical density is $\rho_{\mathrm{crit}} = (3\sqrt{h}\ 10^{-3}\mathrm{eV})^4$. The fixed value of $h = 0.65$ specified by the authors gives $\rho_{\mathrm{crit}} = (2.5 \times 10^{-3}\mathrm{eV})^4$. To translate Eq. (2.40) into the present definition of M^4 requires

$$\mu^4 = \rho_{\mathrm{crit}} M^4 \tag{2.41}$$

where μ is the amplitude of the potential in previous references. This choice makes their $\mu/(\sqrt{h}\ 10^{-3}\,\mathrm{eV}) \approx 2$, which is the minimum amplitude of the potential that would give the observed dark energy density. Therefore, $M^4_{\mathrm{min}} \approx 0.34$ in our Fig. 2.5 is equivalent to $\mu/(\sqrt{h}\ 10^{-3}\,\mathrm{eV}) \approx 2.29$ in Fig. 2 of Ref. [72]. This somewhat larger M^4_{min} is expected, as Ref. [72] imposes a hard limit $\Omega_\phi \geq 0.7$ on its models, whereas the data combination constraints obtained here prefer a smaller Ω_ϕ. A very similar description can be made about the results of the rest of the aforementioned references.

The present analysis results in a significant improvement on the constraint on Ω_ϕ in relation to Ref. [72]; however, the restriction in the same work to $w_0 < -0.965$, citing the inability of the data to provide a better constraint on this parameter, is invalidated as a significantly larger range for the present value of the equation of state is shown in Fig. 2.5. Concerning the slope of the scalar field, the allowed amount of rolling in ϕ_{i}/f is in very good agreement with this reference.

Regarding the results for the equation of state parametrisation scheme, a comparison can be made with Fig. 7 in Ref. [55]. These authors also explore models with $w_0 < -1$; however, because quintessence theories do not extend to the phantom domain, that possibility was excluded in the prior of this parameter space from the start. Another noticeable difference is their use of two datasets and their respective confidence levels; one using BOSS data and one without it. When adding BOSS they obtain a confidence contour that is entirely in the region $w_0 < -1$, but when it is omitted, a small area with $w_0 > -1$ is still allowed.

The shape of the confidence region in Ref. [55] differs greatly from the result displayed in Fig. 2.7. This is because that article adopted uniform priors in the equation of state parameters w_0 and K. Here, instead, these parameters are derived from a sampling based on assumption of the underlying PNGB potential. This induces a prior on those parameters, and particularly on K, which is very far from uniform, i.e. the PNGB model realises a very different model ensemble from that assumed in Ref. [55]. A simple consequence of using an underlying potential is that $w_0 < -1$ is not permitted, but the induced prior on K also leads to a substantially different allowed region. Hence caution is required in using the equation of state approach to assess the viability of explicit thawing quintessence models such as PGNB.

2.4 Conclusions

This chapter is devoted to the idea of quintessence as a viable alternative to the cosmological constant to replace dark energy. The cosmology of this theory, as well as its three main representations were introduced.

Tracking quintessence is characterised by a shallow potential at late times, resulting in an equation of state that decreases from its starting value of w. Observations allow for ghost anomalies in the phenomenology of this case.

The scaling freezing models are a special case of the tracking scenario, in which the potential is characterised by double exponentials. Here the background evolution shifts from $w \approx -1$ very early on, constituting a strange behaviour for a viable representation of DE.

The thawing theory is specified by a potential which mimics an invariable field at early times. When Hubble friction recedes, the field is allowed to roll. These models always present an equation of state that grows positively away from -1, and they are the focus of this investigation.

A probability distribution for the PNGB quintessence model parameters was obtained, which corresponds to the thawing type. The present analysis was carried out using the codes CAMB/COSMOMC, version July 2015. The constraints on the amplitude M^4, initial slope of the field $\phi_{\rm i}/f$, and width $f/M_{\rm Pl}$ of the potential Eq. (2.30) show good agreement with earlier analyses, with some reduction in the permitted range of values as compared to them. These results show the continued viability of the ΛCDM scheme, while showing the extent to which models with a present equation of state value larger than $w_0 = -1$ and a field evolving away from the top of the potential (2.30), corresponding to thawing quintessence, remain acceptable.

Later on, the approximate equation of state (2.37) was revised, which has been applied in Refs. [55, 73]. Under the PNGB assumption, much tighter constraints were found on the curvature parameter K than are found when uniform priors are adopted on the equation of state parameters. This difference highlights a strong ongoing prior dependence from the way thawing dark energy is modelled, which current data are not strong enough to override. The parameter space was explored with different dataset combinations to test their effectiveness. The advantages of a different prior choice were discussed and compared with the standard parametrisation.

The current data are indeed able to meaningfully constrain the PNGB model, and in particular force its behaviour to be close to the cosmological constant limit. However, in detail there remains a significant prior dependence on the constraints obtained, as highlighted by switching the prior from being uniform on f to being uniform on $1/f$. In absence of any clear theoretical guidance on the appropriate form of prior, this dependence needs to be kept in mind in interpreting constraints. Hopefully future data will emerge with sufficient strength to overcome this prior dependence.

Chapter 3

Constraints on hybrid metric-Palatini gravity from background evolution

3.1 Introduction

There exists the possibility of accounting for the self-accelerated cosmic expansion of the Universe without invoking an explicit dark energy source. Instead of assuming quintessence, or another type of matter component, the present cosmological behaviour could be explained by modifying the laws of gravity [16].

As mentioned in Chapter 1, the Einstein-Hilbert action of the theory of General Relativity is expressed in terms of a linear Ricci scalar $R = g^{\mu\nu} R_{\mu\nu}$ [145]. One of the main extensions of GR consists of allowing R to be a general function. The resulting models are known as $f(R)$ gravity, and their phenomenology has been scrutinised in detail [194].

In the metric $f(R)$ formulation, the dynamical scalar field $\phi = df/dR$ satisfies a second-order equation, which does not interact with other types of matter. In order for the resulting theory to be effective at large astrophysical and cosmological scales, the scalar field ϕ must have a light mass.

However, this last requirement produces problematic results, as it is well known that scalars with low masses have a short range impact. Laboratory and Solar

System observations rule out the existence of such a field, unless a screening mechanism is invoked [79].

On the other hand, the $f(R)$ Palatini formulation results in field equations of second order. Nonetheless, this advantage comes at the expense of a scalar field that satisfies an algebraic function of the trace of the matter stress-energy tensor, $\phi = \phi(T)$. This feature of the Palatini representation also presents a challenge, as it may lead to gradient instabilities at various contexts, including cosmological perturbations [48].

The focus of this chapter is a *hybrid* variation of these two approaches, where the purely metric Einstein-Hilbert action is supplemented with metric-affine correction terms constructed in the Palatini formalism. This new idea was born in an effort to establish a consensus between the metric and affine models, with the aim of improving their deficiencies. The concepts presented in this section were taken from Ref. [48], which is the most complete review in the subject.

When it was first introduced, the theory of hybrid metric-Palatini offered the interesting prospect of, not only explaining the late-time cosmic acceleration, but doing so by generating long-range forces without entering into conflict with local tests of gravity and avoiding the need of calling for a screening mechanism [49, 96].

And the outcomes have been extremely encouraging. Like the pure metric and Palatini cases, the hybrid theory has a dynamically equivalent scalar-tensor representation [49, 96]. The authors of those papers have also shown that the scalar field need not be massive in order to pass the stringent Solar System constraints [96], in contrast to the metric $f(R)$ theories, while possibly modifying the cosmological [46] and Galactic [47] dynamics due to its light, long-range interacting nature. The viability of the theory on the smallest scales can be assured as long as the background value of the scalar field remains small [49]. Hence, this theory seems to not need an explicit screening mechanism, even though much work remains to be done on this topic.

The criteria for obtaining cosmic acceleration have already been discussed and introduced in Ref. [46]. Alongside that, several cosmological solutions were derived, depending on the form of the effective scalar field potential, describing both accelerating and decelerating Universes. Lastly, the full set of linearly perturbed Einstein equations was derived for this theory, and the evolution of the metric potentials was shown for a designer model reproducing the ΛCDM background evolution exactly [138].

In Section 3.2, the cosmology of the hybrid metric-Palatini theory is introduced. Afterwards, the dynamics of two models of this kind are specified in Sec. 3.3. Later on, the computational analysis and the observational bounds are presented in Sec. 3.4. Section 3.5 is a summary of the most important points.

The new science included in this chapter is found in a publication of the same name that was co-authored by Nelson Lima and myself. The individual and joint contributions of this work will be highlighted in each segment [137].

3.2 Cosmology in the hybrid metric-Palatini gravity

The four-dimensional action describing the hybrid metric-Palatini gravity is given by

$$\mathcal{S} = \frac{1}{2\kappa^2}\int d^4x\sqrt{-g}\,[R + f(\mathcal{R})] + \int d^4x\sqrt{-g}\mathcal{L}_{\mathrm{M}}(g_{\mu\nu}, \Psi), \tag{3.1}$$

where $\kappa^2 = 8\pi G$ and $c = 1$. $\mathcal{L}_{\mathrm{M}} = \mathcal{L}_{\mathrm{M}}(g^{\mu\nu}, \psi)$ is the standard minimally–coupled matter Lagrangian, R is the metric Einstein-Hilbert Ricci scalar and $\mathcal{R} = g^{\mu\nu}\mathcal{R}_{\mu\nu}$ is the Palatini curvature.

The latter is defined in terms of the metric elements, $g^{\mu\nu}$, and a torsion-less independent connection, $\hat{\Gamma}$, through

$$\mathcal{R} \equiv g^{\mu\nu}\left(\hat{\Gamma}^{\alpha}_{\mu\nu,\alpha} - \hat{\Gamma}^{\alpha}_{\mu\alpha,\nu} + \hat{\Gamma}^{\alpha}_{\alpha\lambda}\hat{\Gamma}^{\lambda}_{\mu\nu} - \hat{\Gamma}^{\alpha}_{\mu\lambda}\hat{\Gamma}^{\lambda}_{\alpha\nu}\right). \tag{3.2}$$

Varying the action (3.1) with respect to the metric,

$$R_{\mu\nu} - \frac{1}{2}g_{\mu\nu}R + f_{\mathcal{R}}\mathcal{R}_{\mu\nu} - \frac{1}{2}f\left(\mathcal{R}\right)g_{\mu\nu} = \kappa^2 T_{\mu\nu}, \tag{3.3}$$

Varying the action with respect to the the independent connection $\hat{\Gamma}^{\alpha}_{\mu\nu}$,

$$\hat{\nabla}^{\alpha}\left(\sqrt{-g}f_{\mathcal{R}}\,g^{\mu\nu}\right) = 0. \tag{3.4}$$

The Palatini Ricci scalar is obtained by tracing Eq. (3.3)

$$R + \kappa^2 T = f_{\mathcal{R}}\mathcal{R} - 2f(\mathcal{R}). \tag{3.5}$$

Equation (3.5) shows that the modifications to Einstein gravity are controlled by the failure of the standard GR trace equation. It would be desirable to write the hybrid metric-Palatini equations of motion in a manner that is independent of the connection $\hat{\Gamma}^{\alpha}_{\mu\nu}$. To do this, let us define a metric conformal to $g_{\mu\nu}$ as $h_{\mu\nu} \equiv f_{\mathcal{R}} g_{\mu\nu}$. It can be shown that

$$\sqrt{-h}h_{\mu\nu} = \sqrt{-g} f_{\mathcal{R}} g_{\mu\nu}, \tag{3.6}$$

which means that Eq. (3.4) is the definition of the Levi-Civita connection of $h_{\mu\nu}$. Solving Eq. (3.4) leads to

$$\begin{aligned} \hat{\Gamma}^{\alpha}_{\mu\nu} &= \frac{1}{2} h^{\lambda\sigma} \left(\partial_\mu h_{\nu\sigma} + \partial_\nu h_{\mu\sigma} - \partial_\sigma h_{\mu\nu} \right) \\ &= \frac{1}{2} \frac{1}{f_{\mathcal{R}}} g^{\lambda\sigma} \left[\partial_\mu (f_{\mathcal{R}} g_{\nu\sigma}) + \partial_\nu (f_{\mathcal{R}} g_{\mu\sigma}) - \partial_\sigma (f_{\mathcal{R}} g_{\mu\nu}) \right] \end{aligned} \tag{3.7}$$

Because Eq. (3.5) relates $\mathcal{R}$ with T and given the explicit expression for $\hat{\Gamma}^{\alpha}_{\mu\nu}$ in Eq. (3.7), the independent connection can be eliminated from the field equations implying that

$$\mathcal{R}_{\mu\nu} = R_{\mu\nu} + \frac{3}{2} \frac{1}{f_{\mathcal{R}}{}^2} f_{\mathcal{R},\mu} f_{\mathcal{R},\nu} - \frac{1}{f_{\mathcal{R}}} \nabla_\mu f_{\mathcal{R},\nu} - \frac{1}{2} \frac{1}{f_{\mathcal{R}}} g_{\mu\nu} \Box f_{\mathcal{R}}. \tag{3.8}$$

For a statistically spatially homogeneous and isotropic universe with Friedmann-Robertson-Walker (FRW) metric, $ds^2 = -dt^2 + a^2(t) d\vec{x}^2$, the modified Einstein equations (3.3) yield the modified Friedmann equations:

$$3H^2 = \frac{1}{1 + f_{\mathcal{R}}} \left[\kappa^2 \rho - 3H \dot{f_{\mathcal{R}}} - \frac{3 \dot{f_{\mathcal{R}}}^2}{4 f_{\mathcal{R}}} + \frac{\mathcal{R} f_{\mathcal{R}} - f(\mathcal{R})}{2} \right], \tag{3.9}$$

and

$$2\dot{H} = \frac{1}{1 + f_{\mathcal{R}}} \left[-\kappa^2 (\rho + p) + H \dot{f_{\mathcal{R}}} - \ddot{f_{\mathcal{R}}} + \frac{3 \dot{f_{\mathcal{R}}}^2}{2 f_{\mathcal{R}}} \right], \tag{3.10}$$

where dots denote a differentiation with respect to physical time, t, and $H = \dot{a}/a$ is the Hubble parameter; ρ and p are the total energy density and pressure of the Universe. An equivalent expression for $\dot{H}$ can be taken from the trace of Eq. 3.3, which gives

$$\dot{H} = \frac{1}{6} \left[f_{\mathcal{R}} \mathcal{R} - 2f(\mathcal{R}) - \kappa^2 T - 12H^2 \right], \tag{3.11}$$

where the condition $R = 6\left(\dot{H} + 2H^2\right)$ has been used.

3.2.1 Scalar-tensor representation

As in the metric and Palatini cases [169], the action (3.1) for the hybrid metric-Palatini theory can be turned into that of a scalar-tensor theory:

$$\mathcal{S} = \frac{1}{2\kappa^2}\int d^4x\sqrt{-g}\left[(\Omega_{\rm A}+\phi)R + \frac{3}{2\phi}\partial_\mu\phi\partial^\mu\phi - V(\phi)\right] + \int d^4x\sqrt{-g}\mathcal{L}_{\rm M}(g_{\mu\nu},\Psi), \tag{3.12}$$

where $\mathcal{R}$ is the auxiliary scalar field, $\Omega_{\mathcal{R}}$ is a coupling constant, $\phi = f_{\mathcal{R}}$ and $V(\phi) = Af_{\mathcal{R}} - f(\mathcal{R})$[49, 96]. In the limit $\Omega_{\rm A} \to 0$, the theory (3.12) recovers the Palatini gravity case; whereas in the limit $\Omega_{\rm A} \to \infty$, the metric $f(R)$ gravity framework is brought back. The hybrid regime corresponds to values of $\Omega_{\rm A}$ between these two limits. The representation (3.12) are in fact massive Brans-Dicke type of theories specified by then non-trivial coupling function

$$\omega_{\rm BD} = \frac{3\phi}{2\phi - 2\Omega_{\rm A}}, \tag{3.13}$$

where $\omega_{\rm BD} = 0$ and $\omega_{\rm BD} = -3/2$ correspond to the scalar tensor representations of the metric $f(R)$ and Palatini formalisms, respectively. Therefore, as in generalised Brans-Dicke theory, perturbative analysis can be performed in order to apply the Parametrised post-Newtonian (PPN) formalism

$$\gamma_{\rm PPN} = \frac{1 - \frac{e^{-m_\phi r}}{2w_{\rm BD}+3}}{1 + \frac{e^{-m_\phi r}}{2w_{\rm BD}+3}} \tag{3.14}$$

$$G_{\rm eff} = \frac{G}{\phi_0}\left[1 + \frac{1}{2w_{\rm BD}+3}e^{-m_\phi r}\right] \tag{3.15}$$

with the rest of the PPN parameters equal to zero [174].

Equation (11) in Ref. [96] is an effective Klein-Gordon equation for the scalar field. Using the FRW metric, it takes the form

$$\ddot{\phi} + 3H\dot{\phi} - \frac{\dot{\phi}^2}{2\phi} + \frac{\phi}{3}\left[2V - (1+\phi)\frac{dV}{d\phi}\right] = \frac{\kappa^2\phi}{3}T. \tag{3.16}$$

Equation (3.16) can be re-expressed as a dynamical expression for the Palatini Ricci scalar, $\mathcal{R}$. From $\phi = f_{\mathcal{R}}$, one can set $\dot{f_{\mathcal{R}}} = \dot{\mathcal{R}}f_{\mathcal{R}\mathcal{R}}$, where $f_{\mathcal{R}\mathcal{R}}$ is the second derivative of $f(\mathcal{R})$ with respect to $\mathcal{R}$. A similar procedure can be done for higher order derivatives, allowing to rewrite Eq. (3.16) as

$$\begin{aligned}
\ddot{\mathcal{R}} &= -\frac{1}{f_{\mathcal{R}\mathcal{R}}}\Bigg[\dot{\mathcal{R}}^2\left(f_{\mathcal{R}\mathcal{R}\mathcal{R}}-\frac{f^2_{\mathcal{R}\mathcal{R}}}{2f_{\mathcal{R}}}\right)+3H\dot{\mathcal{R}}f_{\mathcal{R}\mathcal{R}}+ \\
&+ \frac{f_{\mathcal{R}}}{3}\left[\mathcal{R}\left(f_{\mathcal{R}}-1\right)-2f(\mathcal{R})\right]-\kappa^2\frac{f_{\mathcal{R}}}{3}T\Bigg], \qquad (3.17)
\end{aligned}$$

where Eq. (5) in Ref. [96] has been utilised, and $f_{\mathcal{R}\mathcal{R}\mathcal{R}}$ is the third order derivative of $f(\mathcal{R})$ with respect to $\mathcal{R}$. Eq. (3.17) was obtained by Lima. From this equation, an effective potential where the effective Palatini Ricci scalar will roll, can be defined, since

$$\frac{dV_{\mathrm{Eff}}}{d\mathcal{R}}=\frac{f_{\mathcal{R}}}{3f_{\mathcal{R}\mathcal{R}}}\left[\mathcal{R}\left(f_{\mathcal{R}}-1\right)-2f(\mathcal{R})\right], \qquad (3.18)$$

meaning $V(\mathcal{R})$ will be given by the indefinite integral

$$V(\mathcal{R})=\int^{\mathcal{R}}\frac{f_{\mathcal{R}}}{3f_{\mathcal{R}\mathcal{R}}}\left[\mathcal{R}\left(f_{\mathcal{R}}-1\right)-2f(\mathcal{R})\right]d\mathcal{R}. \qquad (3.19)$$

It was shown that the hybrid metric-Palatini theory reduces to General Relativity with a possible cosmological constant in vacuum, since it shares the property of pure Palatini f (R) theories in Minkowski flat space-time [125]. Furthermore, the fields equation of motion have been analysed as a dynamical system: it was explicitly shown that as long as one provides a suitable $V(f_{\mathcal{R}})$, or equivalently a function $f(\mathcal{R})$ such that the slope of the potential is downwards and its minimum happens for a small value of the scalar field , one should always obtain a natural transition from standard cosmological evolution to accelerated expansion close to the present while also avoiding any conflict with solar-system constraints [96].

Equations (3.9), (3.10) and (3.17) constitute a closed set of differential equations that determines the background evolution for a specified $f(\mathcal{R})$. Note that the standard Friedmann equations of ΛCDM are recovered in the limit $f_{\mathcal{R}} \to 0$.

In the weak-field limit and far from the sources, the scalar field behaves as

$$\phi(r)\sim\phi_0+\frac{2G\phi_0 M}{3r}e^{-m_\phi r}, \qquad (3.20)$$

where the effective mass of the additional scalar degree of freedom is given by [49, 96]

$$m^2_{f_{\mathcal{R}}}=\frac{2V(f_{\mathcal{R}})-V_{f_{\mathcal{R}}}-f_{\mathcal{R}}\left(1+f_{\mathcal{R}}\right)V_{f_{\mathcal{R}}f_{\mathcal{R}}}}{3}. \qquad (3.21)$$

The authors of Refs [49, 96] have also obtained the solutions to the metric perturbations, and found the effective Newton constant, G_{eff}, and the post-Newtonian parameter, γ,

$$\begin{aligned} G_{\text{Eff}} &\equiv \frac{G}{1+\phi_0}\left[1-\frac{\phi_0}{3}e^{-m_\phi r}\right], & (3.22)\\ \gamma_{\text{PPN}} &\equiv \frac{1+\phi_0/3e^{-m_\phi r}}{1-\phi_0/3e^{-m_\phi r}}. & (3.23)\end{aligned}$$

Eqs. (3.22) and (3.23) show that the coupling of the scalar field to the local system depends on ϕ_0. If $\phi_0 \ll 1$, then $G_{\text{eff}} \sim G$ and $\gamma_{\text{PPN}} \sim 1$ regardless of the value of m_ϕ^2. This is contrasting with the general result for metric $f(R)$, where $\beta = \sqrt{1/6}$ and a screening mechanism is mandatory. In hybrid $f(\mathcal{R})$, as long as ϕ_0 is sufficiently small, the theory will pass the Solar System tests, even if the scalar field is very light.

3.3 Models of hybrid metric-Palatini gravity

While the general framework of this theory was derived in Refs. [46, 47, 49, 96], the authors did not write down specific models, nor explore their consequences. This omission presented the opportunity to contribute to the development of hybrid $f(\mathcal{R})$ by analysing the background evolution of models of this kind with specific potentials. These were inspired by theories of $f(R)$ gravity, such as the Starobinsky [211] and the exponential [108] case, but are essentially phenomenological choices to be tested with the background evolution formalism displayed before. The full content of this section was obtained in collaboration between Lima and myself.

In the following analyses, Eqs. (3.11) and (3.17) were used to numerically evolve the background quantities predicted by two specific $f(\mathcal{R})$ models. To set the initial conditions, $f_{\mathcal{R}}$ is fixed to a very small value, at a high redshift, z_{i}, such that the deviation from the Gravitational constant, G, is effectively small [47, 49, 96, 138] in the high curvature regime. Then F can be inverted to find $\mathcal{R}$ at that redshift.

The second initial condition was set to $\dot{\mathcal{R}}_{\text{i}} = 0$, in order to minimise deviations from standard General Relativity and to use Eq. (3.9) to resolve for the Hubble parameter at z_{i}. The Ricci scalar, R, can be computed using the GR relation, $R =$

$6\left(\dot{H}+2H^2\right)$. Even though $\dot{\mathcal{R}}_{\rm i}=0$ is a strong assumption, the models were tested for a fairly broad range of initial velocities, within a slow-roll regime, and it was observed that their qualitative behavior remained unaltered with the late-time evolution tending to an effective Cosmological Constant, and $\mathcal{R}$ asymptotically reaching the equilibrium position predicted by the effective potential defined in Eq. (3.19).

3.3.1 The exponential model

The first scenario is defined by an exponential function, given by

$$f(\mathcal{R})=\Lambda_\star\left(1+e^{-\mathcal{R}/\mathcal{R}_\star}\right), \tag{3.24}$$

where $\Lambda_\star$ and $\mathcal{R}_\star$ are the model's parameters, both of order H_0^2, where H_0 is the present-day value of the Hubble parameter. In order to avoid any divergences, $\mathcal{R}_\star$ is defined as a positive constant, while $\Lambda_\star$ should be a negative constant. This last choice of sign is particularly relevant at late-times where, to recover standard GR with an effective Cosmological Constant, one should have $\Lambda_\star\approx-2\Lambda$. Hence, $\Lambda_\star<0$ allows the effective Cosmological Constant to have the correct sign, which becomes clear, for instance, looking at Eq. (3.5) in vacuum.

The effective potential, $V(\mathcal{R})$, associated to this model, is obtained by doing the indefinite integral defined by Eq. (3.19), which has the simple form

$$\begin{aligned}V(\mathcal{R}) &= \frac{\mathcal{R}_\star}{3}\Bigg[2\Lambda_\star\mathcal{R}+\frac{1}{2}\mathcal{R}^2-2\Lambda_\star\mathcal{R}_\star e^{-\mathcal{R}/\mathcal{R}_\star}\\ &- e^{-\mathcal{R}/\mathcal{R}_\star}\left(\Lambda_\star\mathcal{R}+\Lambda_\star\mathcal{R}_\star\right)\Bigg].\end{aligned} \tag{3.25}$$

Setting the initial conditions at $z_{\rm i}=10^3$ to yield a very small $f_{\mathcal{R}}$ value in order to minimise deviations from the actual gravitational constant in the high curvature regime, the potential will be mostly dominated by its quadratic terms for order unit values of $\mathcal{R}_\star$. The minimum can then be estimated by

$$\mathcal{R}_{\rm min}\approx-2\Lambda_\star. \tag{3.26}$$

The effective cosmological constant value at which the Ricci scalar should sit in vacuum is given by the trace equation

$$\Lambda_{\text{Eff}} = \frac{1}{2}\left[-2\Lambda_\star f_{\mathcal{R}}(-2\Lambda_\star) - 2f(\Lambda_\star)\right] \approx -\Lambda_\star. \tag{3.27}$$

Hence, it is expected to obtain a ΛCDM like evolution in the distant future, if the solution for $\mathcal{R}$ is to settle at the minimum of its potential.

In Fig. 3.1, the background evolution predicted by this model is plotted for a set of parameters as a function of redshift, z. A Brent algorithm (see [39]) is used to find the correct $\Lambda_\star$ value that recovers a flat cosmology. Hence, for this case, the only true free parameter will be $\mathcal{R}_\star$.

As can be seen in Fig. 3.1, the evolution of the Palatini Ricci scalar starts at a position where the potential is tilted and one would expect for it to roll down towards the minimum. However, at early times, the evolution of $\mathcal{R}$ is dominated by the stress–energy tensor trace or, equivalently, by the matter energy density.

Since the ratio $f_{\mathcal{R}}/f_{\mathcal{R}\mathcal{R}}$ is negative throughout the whole evolution, the matter density contribution pushes $\mathcal{R}$ upwards the effective potential, while its slope and the Hubble friction term exert the opposite effect. As matter ceases to dominate close to the present, $\mathcal{R}$ inverts its motion and starts evolving towards the minimum, where it will asymptotically settle in the distant future.

Lastly, Fig. 3.1 presents the evolution of the deceleration parameter q. The exponential case predicts a Universe that will be expanding in an accelerated manner today, transitioning from a matter dominated decelerating phase at a redshift $z \approx 1$, as, for $z = 0$, $q < 0$. This is a general result of this model, as can be inferred from the deceleration parameter equation

$$q = -\frac{\dot{H}}{H^2} - 1, \tag{3.28}$$

where $\dot{H}$ is given by Eq. (3.11). Switching from physical time t to $\ln a$, Eq. (3.28) at $z = 0$ is

$$q = -\frac{1}{6H_0^2}\left[f_{\mathcal{R}}\mathcal{R} - 2f(\mathcal{R}) + 3H_0^2\Omega_{\text{M}} - 12H_0^2\right] - 1. \tag{3.29}$$

As observed in Fig. 3.1, the model evolves towards smaller values of $f_{\mathcal{R}}$ today, as the exponential is suppressed by the larger values of $\mathcal{R}$. Therefore, in Eq. (3.29) the term $(f_{\mathcal{R}}\mathcal{R})$ can be neglected.

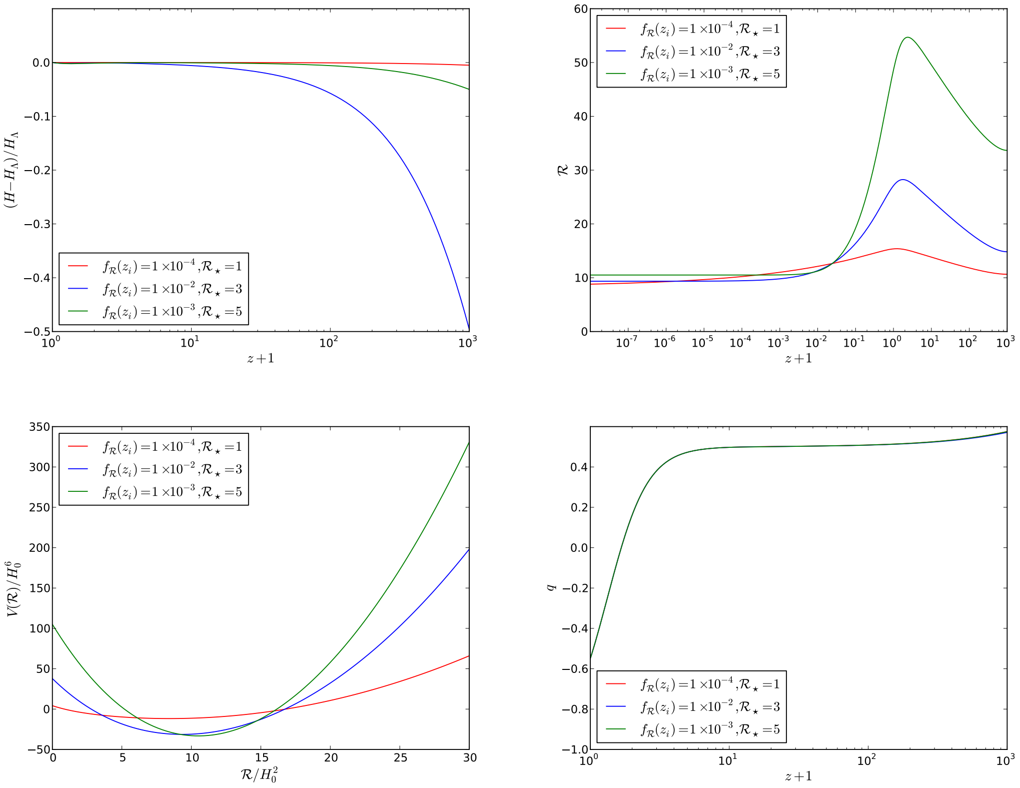

Figure 3.1 *The background evolution predicted by the exponential $f(\mathcal{R})$ model compared to ΛCDM. $\mathcal{R}$ is plotted far into the future ($z \to -1$), to explicitly show that this solution asymptotically tends to the minimum of the potential, $V(\mathcal{R})$, which is also displayed. The deceleration parameter q is also shown. The present-day matter energy density is set to be $\Omega_\mathrm{m} = 0.30$, and $\mathcal{R}_\star = 1$ is in units of H_0^2.*

Then, from Eq. 3.24, it is noticeable that $f(\mathcal{R})$ will be dominated by $\Lambda_\star$. Since this parameter is determined from imposing a flat cosmology, $\Lambda_\star \approx -2\Lambda$, where $\Lambda \approx 2.1H_0^2$ is the actual cosmological constant. In light of these arguments, Eq. (3.29) becomes

$$q \approx -\frac{2\Lambda}{3H_0^2} - \frac{\Omega_\mathrm{M}}{2} + 1 \approx -0.55. \tag{3.30}$$

Fig. 3.1 demonstrates that this prediction matches remarkably well the numerical values obtained for q today for different parameters of the exponential model. Hence, this model should always predict an accelerated expansion today.

3.3.2 The quadratic model

The second model is of quadratic shape, and is defined by the function

$$f(\mathcal{R}) = \Lambda_\star \left(1 + \mathcal{R}^2/\mathcal{R}_\star^2\right), \tag{3.31}$$

where $\Lambda_\star$ and $\mathcal{R}_\star$ are a negative and positive constant of order H_0^2, just like in the previous model. Computing the indefinite integral defined in Eq. (3.19) one can find the associated effective potential:

$$V(\mathcal{R}) = -\frac{1}{3}\Lambda_\star \mathcal{R}^2 - \frac{1}{9}\mathcal{R}^3, \tag{3.32}$$

which clearly has a global minimum at $\mathcal{R} = 0$ and a maximum at $\mathcal{R} = 2\Lambda_\star$. Therefore, the solution for $\mathcal{R}$ is expected to asymptotically settle at the minimum in vacuum, leading to an effective cosmological constant value of

$$\Lambda_{\text{eff}} \equiv \frac{1}{2}\left[-2\Lambda_\star f_{\mathcal{R}}(0) - 2f(0)\right] = -\Lambda_\star. \tag{3.33}$$

In Fig. 3.2, the evolution predicted by the quadratic model for H is shown, compared to ΛCDM's, for different values of $f_{\mathcal{R}}(z_{\text{i}})$ and $\mathcal{R}$. A negative $f_{\mathcal{R}}(z_{\text{i}})$ was chosen as this sets the initial $\mathcal{R}$ to be positive.

In this instance, it is observed that $\mathcal{R}$ rolls down the effective potential towards the minimum from the beginning of the evolution, asymptotically settling there. When compared to the behavior seen for the exponential model in Fig. 3.1, the different dynamics are linked to the ratio $f_{\mathcal{R}}/f_{\mathcal{R}\mathcal{R}}$ multiplying the stress–energy tensor in the dynamical equation for $\mathcal{R}$.

For this particular setting of the quadratic model, this ratio is positive at early times, meaning that $\mathcal{R}$ will be pulled down by the matter energy density term towards the minimum of the potential, asymptotically settling there when the matter contribution becomes negligible.

If a positive value for $\mathcal{R}(z_{\text{i}})$ had been chosen, the behavior wouldn't qualitatively change, with the matter term dictating $\mathcal{R}$ to evolve towards the minimum in a symmetric manner, starting from $\mathcal{R} < 0$.

Also, by setting the initial conditions for $f_{\mathcal{R}}(z_{\text{i}})$ such that deviations from standard GR are kept small, $\mathcal{R}$ starts its evolution already close to the minimum,

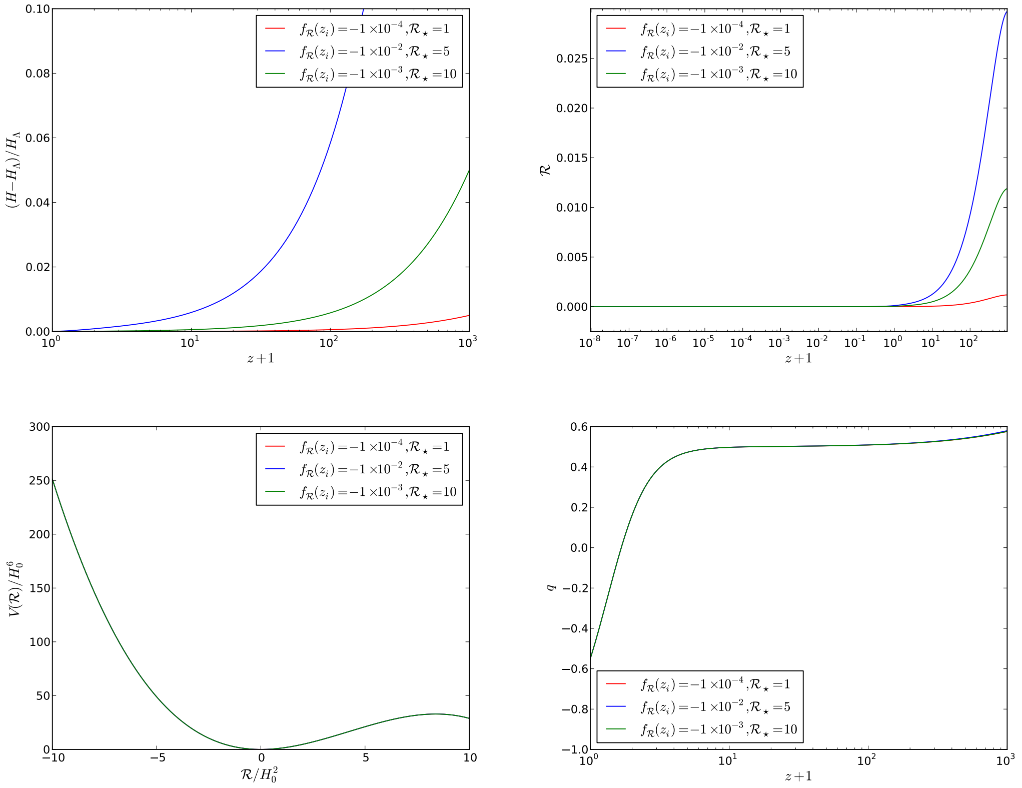

Figure 3.2 *The same as Fig. 3.1 for the quadratic $f(\mathcal{R})$ model. The matter density parameter has been fixed to $\Omega_\mathrm{m} = 0.30$.*

guaranteeing that it settles onto the minimum of the effective potential $V(\mathcal{R})$. Had the evolution started at a point such that the initial value of $\mathcal{R}$ would be beyond the maximum observed for the effective potential in Fig. 3.2, $\mathcal{R}$ would roll indefinitely, jeopardising the late-time achievement of an effective cosmological constant in this model.

3.4 Background Observables

The present chapter discusses the late time effects of hybrid metric-Palatini gravity. As such, it was decided against the need of calculating the full CMB temperature anisotropies using CAMB. Instead, only the peak positions of *Planck* were utilised. This was a motivator to create a different Metropis-Hastings algorithm other than COSMOMC, because using the latter would require adding the changes to the linear perturbations of this model, which would have increased

Table 3.1: Inverse covariance matrix for the distance information obtained from Planck in the ΛCDM framework.

	Planck			
	Best fit	$l_A(z_*)$	$R(z_*)$	z_*
$l_A(z_*)$	301.77	44.077	−383.927	−1.941
$R(z_*)$	1.7477	−383.927	48976.330	−630.791
z_*	1090.25	−1.941	−630.791	12.592

the difficulty of the analysis without much gain at this point. However, the GETDIST code was utilised, as this part of the program works by providing a set of chains and a file specifying the names of all parameters in them, irrespective of how these were obtained.

3.4.1 Observables

To constrain the models parameters, several background-related observables were utilised: the luminosity distance from Supernova type Ia (SNIa); the baryon acoustic oscillations (BAO); the shift parameter, acoustic scale and redshift of decoupling from the cosmic microwave background (CMB). A detailed explanation on the statistics treatment of SNIa, BAO and CMB is detailed in Sec. 1.8.

SNIa luminosity–redshift relation

For the supernovae analysis, the Union 2.1 SNIa catalog from the "Supernova Cosmology Project" (SCP) [216] was utilised. These data set are a compilation of 580 type Ia Supernovae located over the redshift interval $0.623 < z < 1.415$. In the Metropolis-Hastings algorithm, the nuisance parameter H_0 was marginalised using the procedure described in the appendix of Ref. [91].

Baryon Acoustic Oscillations peak

Following the Planck analysis [7], the BAO observations used were the 6dF Galaxy Redshift Survey (6dFGRS) at low redshift, $d^{\mathrm{obs}}(z = 0.106) = 0.336 \pm 0.015$ [30], the Luminous Red Galaxies (LRG) sample of the Sloan Digital Sky Survey (SDSS)

7-year data release at the median redshift, $d^{\rm obs}(z = 0.35) = 0.1126 \pm 0.0022$ [171], and the BAO signal from BOSS CMASS DR9, $d^{\rm obs}(z = 0.57) = 0.0732 \pm 0.0012$ [18].

Cosmic Microwave Background

The Planck distance information for the ΛCDM model was also added to constrain the two potential choices. In Table 3.1 it is possible to read the inverse covariance matrix and best-fit values obtained from Planck [223].

3.4.2 Metropolis - Hastings Algorithm

The calculation of the χ^2 of each observable and the probability distributions of our models' parameters was performed by means of a Metropolis–Hastings algorithm, which is a Markov Chain Monte Carlo method based on a stochastic sampling technique [162]. One of the main advantages of the Metropolis–Hastings algorithm is its treatment of marginalised variables. When considering a subset of the parameters that form a chain, the marginalisation over the remainder of the parameters occurs immediately, therefore making the treatment of the chains a simple process. This algorithm was developed by me, in a module using the Python programming language, where the core steps where:

1. Define the maximum number of samples to have on each chain.
2. Provide a prior range of variation for the parameters considered.
3. Choose a likely value for the free parameters as a starting point for the exploration.
4. Calculate the posterior distribution, X, as the sum of each survey χ^2, $X = \sum \chi^2$, using the starting point defined in the previous step.
5. Define a set of new parameter values from a Gaussian random distribution with center value $\mu = 0$ and an appropriate width, $\sigma_{\rm i}$, individually chosen for each parameter.
6. Verify if the new parameters are within the given prior range. If they are not, this evaluation is rejected and a new one set of parameters is randomly chosen.

7. If the parameters are in range, a new posterior probability distribution $Y = \sum \chi^2$ is calculated based on them.

8. Define the criteria α as the ratio between the new and old posterior probability distributions, i.e. $\alpha = e^{-Y/2} e^{X/2}$.

9. If $\alpha > 1$, the new set of parameters are accepted and can be added to the Markov chain. Otherwise, a random number β is chosen from an uniform distribution: if $\alpha > \beta$, the parameters are also considered towards the chain; if $\alpha < \beta$ the parameters are rejected.

10. Repeat steps $5 - 9$ until the number of samples initially defined for each chain is achieved.

3.4.3 Priors

The two $f(\mathcal{R})$ models share a set of three parameters: the present-day relative energy densities of matter and baryons, Ω_{M} and Ω_{b}, and the present-day value of the Hubble parameter, H_0. The ranges chosen for them are, respectively, $[0.01, 0.99]$, $[0.001, 0.080]$ and $[40.0, 100.0]$.

For both models, $\Lambda_\star$ is determined by the background evolution, assuming the recovery of a flat cosmology today, at $a = 1$. As described in Sec. 3.3.1, this is achieved using a Brent algorithm (see Ref. [39]) which ensures that the present-day value of the numerical Hubble parameter obtained coincides with H_0. The background evolution starts at a redshift of $z_{\mathrm{i}} = 10^8$.

For the exponential model, two situations are studied. In the first case, $f_{\mathcal{R}}$ at z_{i} is fixed to a very small value, 10^{-4}, and $\mathcal{R}_\star$ varies between $[1.0, 10.0]$. This is performed in order to test the data against a definitive modification of gravity where the ΛCDM limit is not explicitly attainable.

In the second case, $f_{\mathcal{R}}(z_{\mathrm{i}})$ varies between $[1 \times 10^{-6}, 0.1]$ and $\mathcal{R}_\star$ between $[0.01, 15.0]$. The case $f_{\mathcal{R}}(z_{\mathrm{i}}) = 0$ cannot be considered due to the way the initial conditions in this model are set, as this would lead to a logarithmic divergence. Therefore, the deviations from standard GR plus ΛCDM at early times can only be asymptotically minimised by taking $f_{\mathcal{R}}(z_i) \to 0^+$. Nevertheless, the possible size of the deviation could possibly be tested by considering an upper limit for $f_{\mathcal{R}}(z_{\mathrm{i}})$ of order 10^{-1}.

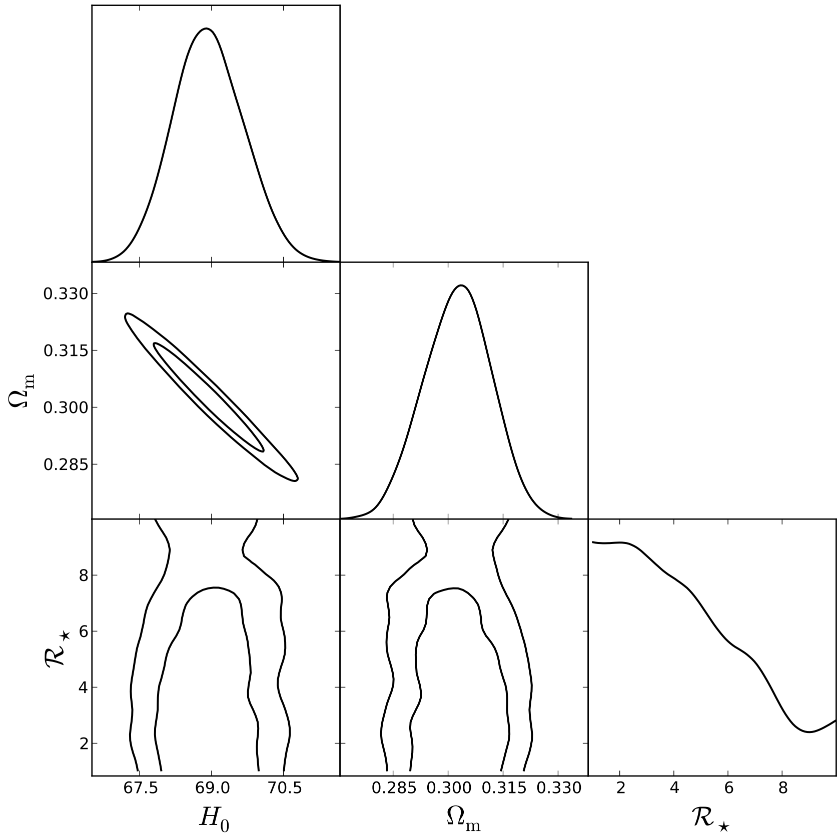

Figure 3.3 *The 2-d contours of the combined constraints from the background surveys considered for the exponential* $f(\mathcal{R})$ *model with* $f_{\mathcal{R}}(z_{\rm i})$ *fixed to* 10^{-4}. *The individual marginalised posterior probability distributions of each parameter is also plotted.*

Lastly, for the quadratic model, $\mathcal{R}_\star$ is fixed to a chosen value and $f_{\mathcal{R}}$ at z_i varies between $[-0.1, 0.1]$. Since the effective potential on which $\mathcal{R}$ evolves is independent of $\mathcal{R}_\star$ in the quadratic model, this parameter is fixed. This independence can be observed in Eq. (3.32).

3.4.4 Constraints

The following results depict the combined constraints of the three background surveys described in Sec. 3.4.1. These figures were obtained in collaboration between Lima and myself, using the plotting functions available in COSMOMC [133].

Figure 3.3 exhibits a triangular plot with the 2-d contours between H_0, $\Omega_{\rm M}$ and $\mathcal{R}_\star$, as well as with the individualised posterior distributions of each parameter for the exponential model considering $f_{\mathcal{R}}(z_{\rm i})$ fixed to 10^{-4}. The value of H_0 obtained is slightly higher than the recent Planck result [7]; this is an expected difference, as the present analysis is limited to background observables.

The density parameter $\Omega_{\rm M}$ also presents a smaller value than in [7], which results from the combination of the different surveys considered, as the Union2.1 and BAO surveys do tend to prefer a slightly smaller $\Omega_{\rm m}$ value than Planck [7, 216]. The 1-σ limits on these parameters are $H_0 = 68.9 \pm 0.7$ and $\Omega_{\rm M} = 0.303 \pm 0.009$.

For the $\mathcal{R}_\star$ parameter the confidence limits cannot be clearly stated, as these are completely prior determined. Interestingly, a preference towards smaller values of $\mathcal{R}_\star$ is observed, possibly extending all the way to 0 had this limit been considered.

The initial conditions are set by imposing a $f_{\mathcal{R}}$ value at the starting redshift $z_{\rm i}$ that is inverted to obtain the corresponding $\mathcal{R}_{\rm i}$. Hence, for this model, $\mathcal{R}_{\rm i} = -\mathcal{R}_\star \ln\left[-f_{\mathcal{R}}(z_{\rm i})\mathcal{R}_\star/\Lambda_\star\right]$. Therefore, it is not possible to have a pure GR plus ΛCDM for the exponential model because neither $f_{\mathcal{R}}(z_{\rm i})$ or $\mathcal{R}_\star$ can be set exactly to zero.

However, the closest this model can get to ΛCDM, for a fixed $f_{\mathcal{R}}(z_{\rm i})$, is when $\mathcal{R}_\star \to 0^+$: in this limit, it is observed that $\mathcal{R}_{\rm i}$ tends to decreasingly smaller values as $\mathcal{R}_\star \to 0^+$, while keeping the $\mathcal{R}/\mathcal{R}_\star$ ratio considerably large such that $f(\mathcal{R}) \to \Lambda_\star$. Hence, an almost ΛCDM like evolution is recovered, which can be understood looking at the trace equation, Eq. (3.5), which tends increasingly closer to the GR plus ΛCDM limit of $R + \kappa^2 T = 4\Lambda$.

Figure 3.4 presents the combined constraints on the exponential model considering the flat prior on $f_{\mathcal{R}}(z_{\rm i})$ between $[1 \times 10^{-6}, 0.1]$. A clear upper limit on $f_{\mathcal{R}}(z_{\rm i})$ of around 10^{-2} can be observed, limiting, therefore, the maximum deviation from the actual gravitational constant G one can have at early times. However, now $\mathcal{R}_\star$ appears even more unconstrained by the data, as larger values of $\mathcal{R}_\star$ are also allowed since these can be compensated by the $f_{\mathcal{R}}(z_{\rm i}) \to 0^+$ values: this limit pushes the model closer to the standard GR plus ΛCDM limit even for large values of $\mathcal{R}_\star$.

It is reinforced that setting the deviation from standard GR exactly to zero would lead to a logarithmic divergence in the initial conditions of this model. However, the lower limit chosen for the $f_{\mathcal{R}}(z_{\rm i})$ prior is much smaller than the current precision with which one can measure early deviations from the gravitational constant [87, 219].

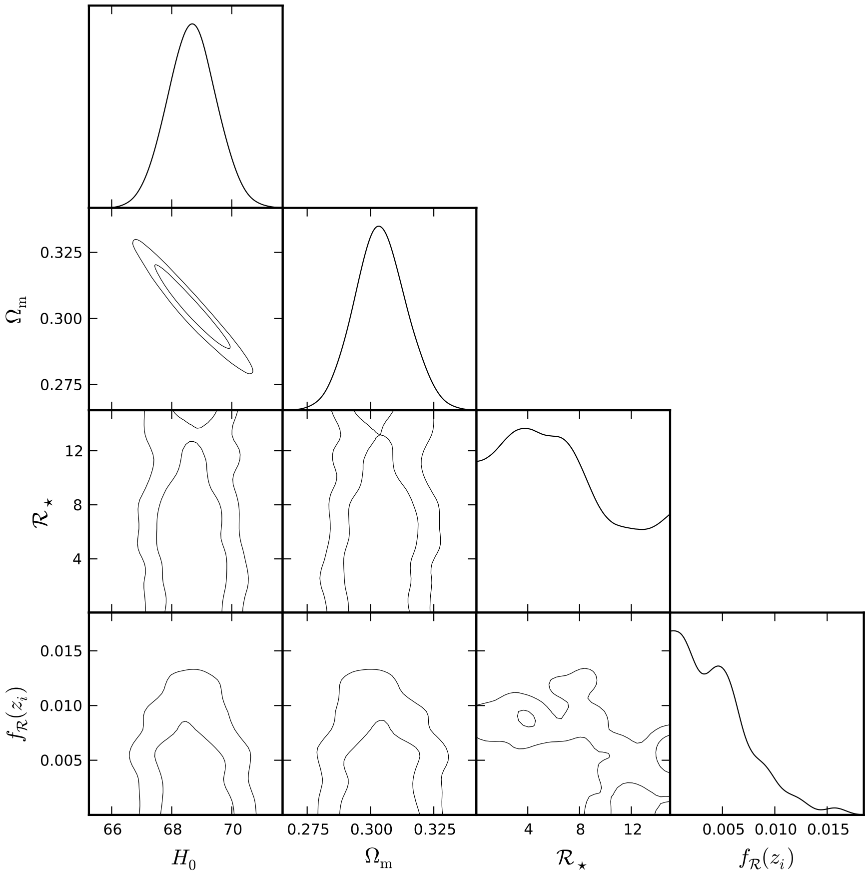

Figure 3.4 *The 2-d contours of the combined constraints from the background surveys considered for the exponential $f(\mathcal{R})$ model by considering a prior range for $f_{\mathcal{R}}(z_{\rm i})$ between $[1 \times 10^{-6}, 0.1]$. The individual marginalised posterior probability distributions of each parameter is also plotted.*

Lastly, in Fig. 3.5 a triangular plot with the confidence contours and 1-d marginalised posterior probability distributions for the $f(\mathcal{R})$ quadratic model is shown. The results obtained are very similar for the standard cosmological parameters H_0 and $\Omega_{\rm m}$ as the ones observed in the exponential model in both situations, with the 1-σ limits on them being $H_0 = 68.9 \pm 0.8$ and $\Omega_{\rm M} = 0.303 \pm 0.010$.

For the quadratic model, $\mathcal{R}_\star$ is kept fixed because it would not have a significant impact on the background evolution predicted by this model since it does not alter the shape of the potential on which $\mathcal{R}$ evolves. Hence, the third parameter that constraints are shown for is the initial value imposed for $f_{\mathcal{R}}$ at the starting redshift, $z_{\rm i}$. This, as detailed before, sets the maximum deviation from the

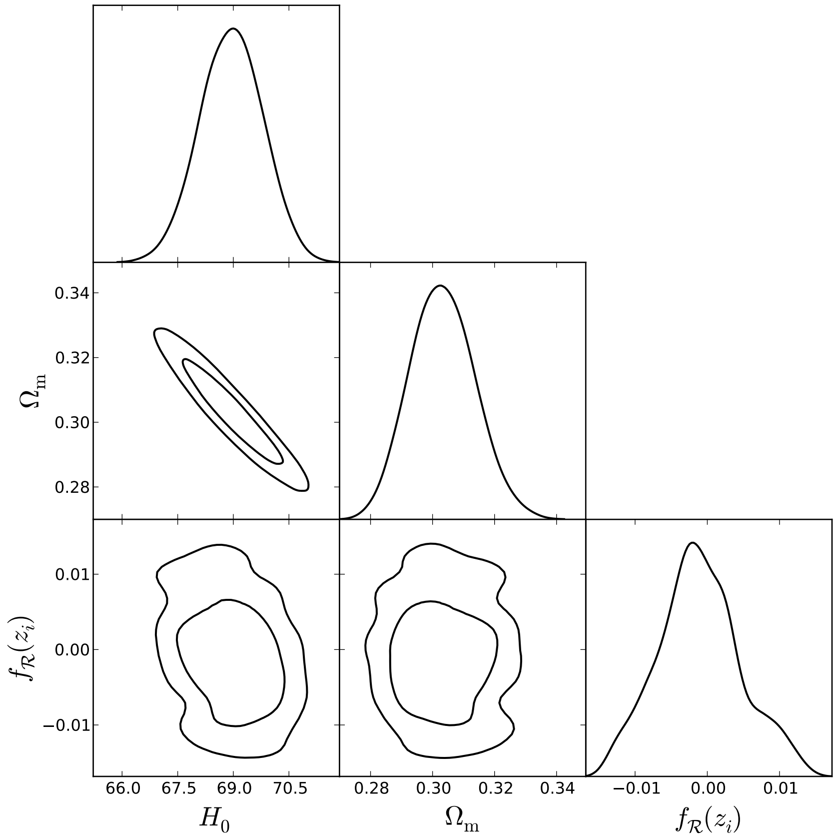

Figure 3.5 *Similar as Figs. 3.3 and 3.4 for the quadratic $f(\mathcal{R})$ model.*

standard gravitational constant G one can have at early times in this model, since $f_{\mathcal{R}}$ evolves asymptotically to 0 from its starting value.

It is clear that as $f_{\mathcal{R}}(z_{\mathrm{i}}) \to 0$ the background description gets closer to a ΛCDM like evolution. Given that it would be numerically hard to evolve the model if $f_{\mathcal{R}}(z_{\mathrm{i}}) = 0$, an approximation was coded into the Metropolis–Hastings algorithm. If the program encountered such value, the resulting evolution will be exactly ΛCDM.

The results obtained show a preference for a standard GR plus ΛCDM scenario, as can be seen in the 1-d posterior probability distribution for $f_{\mathcal{R}}(z_{\mathrm{i}})$ in Fig. 3.5. The corresponding 1-σ confidence limits are $f_{\mathcal{R}}(z_{\mathrm{i}}) = -0.001 \pm 0.006$. A symmetry on the posterior distribution of this parameter is also observed, which could be expected given that the evolution of $\mathcal{R}$ is symmetric under the change of sign of $f_{\mathcal{R}}$, as discussed in Sec. 3.3.2.

In this context, the constraints that affect quintessence models coupled directly to matter are worth mentioning. For the case of the QCD axion, the width of the potential f is only mildly constrained by standard model interactions, leading to a range of allowed masses $10^{-10}\mathrm{eV} \leq M \leq 10^{-3}\mathrm{eV}$, where M is the mass of the PNGB particle given as $M = \mu^2/f$, $\mu^4 \sim m_\mathrm{u}\Lambda^3_\mathrm{QCD}$ and m_u is the u-quark mass.

For a generic axion the parameters μ and f are related by the actual mass of the scalar particle expected to be of the order $\mu^2/f \approx 10^{-22}\mathrm{eV}$. If the condition $f < M_\mathrm{Pl}$ is imposed, the scale of the explicit symmetry breaking is restricted to be less than around a keV to obtain the acceptable mass [68].

3.5 Conclusion

In this chapter, the study of hybrid metric-Palatini gravity is put forward as a powerful alternative to the better known $f(R)$ theory. The main cosmological results were partially re-derived and explained.

The scalar field expression, for the additional degree of freedom introduced by this theory, was rewritten as a dynamical equation for the actual Palatini Ricci scalar $\mathcal{R}$. The initial conditions were defined by imposing the deviation one has from standard GR at early times. Hence, $f_\mathcal{R}(z_\mathrm{i})$ was set to a small value and later was inverted to obtain $\mathcal{R}(z_\mathrm{i})$, while keeping $\dot{\mathcal{R}}(z_\mathrm{i}) = 0$.

An effective potential $V(\mathcal{R})$ is also defined, where the Palatini Ricci scalar evolves. If a minimum exists, $\mathcal{R}$ should asymptotically settle there in vacuum, so that one recovers standard GR plus an effective cosmological constant at late times.

Afterwards, two $f(\mathcal{R})$ models, of exponential and quadratic shape were introduced. The potential $V(\mathcal{R})$ could potentially have a complicated form in this theory, but, for the models introduced here, that is not the case.

It was shown that the background evolution predicted by them does not deviate much from ΛCDM. This could be different, had it been decided to set the deviation from the gravitational constant G in the high-redshift regime to be large. Also, it was explicitly shown that the effective potential $V(\mathcal{R})$ for both models and $\mathcal{R}$ asymptotically tend to its minimum at late times. This is less obvious in the exponential model as the matter term in Eq. (3.16) initially drives the Palatini Ricci scalar up the potential, only for it to later slowly fall down towards the minimum due to the potential slope.

The set combination of background CMB, BAO and Supernovae data were used to constrain the models. Keeping $f_{\mathcal{R}}(z_{\mathrm{i}})$ fixed to 10^{-4} for the exponential scenario, an actual constraint on the $\mathcal{R}_\star$ parameter could not be stated. However, as expected, the data seem to tend towards the ΛCDM limit. If the prior range had not been restricted, in order to have a definitive modification of gravity without the ΛCDM limit, it would be possible to observe the lower range of the confidence contours in Fig. 3.3 tending to 0^+ in $\mathcal{R}_\star$.

Still for the exponential model, when a flat prior on $f_{\mathcal{R}}(z_{\mathrm{i}})$ between $[1 \times 10^{-6}, 0.1]$ was imposed, a clear upper limit of order 10^{-2} was observed. This value marks the maximum deviation one can have at early times from the actual gravitational constant G. Also, the data exhibited a marked tendency towards the lower limit of $f_{\mathcal{R}}(z_{\mathrm{i}})$, as $f_{\mathcal{R}}(z_{\mathrm{i}}) \to 0^+$ minimises the early time deviations from the gravitational constant G, allowing the model to get asymptotically closer to the standard GR+ΛCDM limit.

For the quadratic case, the initial value of $f_{\mathcal{R}}$ is constrained while keeping $\mathcal{R}_\star$ fixed which means that, effectively, the maximum deviation from the gravitational constant at early times is being constrained. As expected, the results indicate a preference towards no deviation at all, as in the standard GR plus Λ limit. The confidence limits for this parameter are $f_{\mathcal{R}}(z_{\mathrm{i}}) = -0.001 \pm 0.006$.

Hence, this work demonstrates that $f_{\mathcal{R}}(z_{\mathrm{i}})$ could play an important role in the constraining of this theory, as it sets the deviation one observes from standard GR at early times. The value obtained for this parameter restricts the maximum variation of the effective gravitational constant G_{eff} to 1% of the Newtonian case, which is in excellent agreement with constraints available from the big bang nucleosynthesis and the CMB [87, 219].

This, combined with the fact that the Newtonian potentials also exhibit a departing behavior from ΛCDM at early times [138], suggests that it would be very interesting to constrain these models using the latest Planck data available by enhancing the formalism developed so far with the inclusion of perturbation observables.

Chapter 4

Constraints on decaying early modified gravity from cosmological observations

4.1 Introduction

Einstein's Theory of General Relativity (GR) has been well tested in the Solar System, where, however, potential large-scale deviations may be suppressed due to screening effects [60, 113, 129]. There is now a complementary effort in obtaining competitive constraints on larger scales, with a surge of surveys that will significantly improve our knowledge of the cosmological regime, such as the Dark Energy Survey (DES) [3], the extended Baryon Oscillation Spectroscopic Survey (eBOSS) [65] and the Euclid survey [132]

Much of the interest in modified gravity theories has arisen in the search for alternative explanations for the observed late-time accelerated expansion of our Universe [15, 111, 175, 183], possibly avoiding the fine-tuning problem of the cosmological constant Λ adopted in the standard model of cosmology ΛCDM.

However, in Ref. [148] it has recently been shown that scalar-tensor theories of gravity such as Brans-Dicke [35], Galileon [166], and $f(R)$ gravity [207], or any other models embedded in the Horndeski action [101] cannot yield an observationally compatible self-acceleration effect due to modified gravity that its genuinely different from Λ or dark energy, unless the cosmological speed of gravitational waves differs substantially from the speed of light. While such a deviation is unlikely [152], modified gravity theories are nevertheless relevant to test gravity and understand how it acts across all scales and epochs in cosmic time.

However, given the original interest in cosmic acceleration, the study of modified gravity has predominantly focused on late-time effects with a recovery of GR at high redshifts.

Hence, early-time modifications have, so far, evaded a thorough investigation and when they have been studied (e.g. [36, 146]), their effects at early times have not been clearly separated from their late-time effects. The missing analysis of early-time modifications and their impact on cosmological observables constitutes a gap in our current understanding of the gravitational processes at work and we lack a consistent quantitative analysis of the constraining power current (and future) cosmological surveys have over this regime of gravity. Generally, the assumption of GR at early times without a test against alternatives is a strong extrapolation from its exclusive validity in the late-time time Solar-System region (or even from late-time cosmology).

This investigation is also important to quantify the improvement on our current understanding of the cosmological model that can be expected with future surveys such as 21-cm intensity mapping (see, e.g., [124] for expected dark energy constraints), the use of gravitational waves as standard sirens at high redshifts, or constraints from surveys such as the Square Kilometer Array (SKA) on the horizon [190].

This chapter explores to what extent modifications of gravity that may arise after recombination and decay towards the present can be constrained with current cosmological observations that stem either from their impact on the late-time large scale-structure or changes in the imprint of early-time inhomogeneities on the cosmic microwave background. For this purpose, the decaying mode of a hybrid metric-Palatini gravity model is adopted, which enables to separate early- from late-time effects. This is introduced in Section 4.2, and the advantages of choosing a $f(\mathcal{R})$ theory over a $f(R)$ one that were described in sections 3.1 and 3.2 also apply for this study.. Afterwards, Sec. 4.3 describes the linear perturbations on this theory. In Sec. 4.6, the observational bounds obtained are discussed. These are then compared to future 21-cm intensity mapping and standard sirens in Sec. 4.6.3.

The results of the present chapter are included in a publication of the same name, which was co-authored with Nelson Lima and Lucas Lombriser [139]. Individual and collective contributions will be mentioned in the appropriate sections.

4.2 Designer $f(\mathcal{R})$ Model

While metric $f(R)$ theory, where the connection is not independent, is much more frequently adopted as toy model to study modifications of gravity, and also possesses a decaying mode [178], it naturally predicts a 4/3 enhancement of the effective gravitational coupling in unscreened observables at late times and small scales. There always exists a small enough object in a late-time, low-density environment that is not screened and hence exhibits a modified gravity effect that could potentially be used to constrain the modification, for instance, a dwarf galaxy in a void [109]. Similarly, an upweighting of low-density regions in statistical observations of the large-scale structure can be used to effectively unscreen the modifications [149]. Hybrid metric-Palatini gravity evades these constraints as the unscreened effective gravitational coupling itself tends to the Newtonian value at late times (this argument will be explained in more detail in Sec. 4.3.1).

The model adopted to describe the evolution of the decaying early modification of gravity is now presented. It was first introduced by Lima, 2014; henceforth, the results of Secs. 4.2- 4.3.2 reproduce the results of his work. Recalling Eq. 3.8 from the previous chapter, an effective equation of state can be defined as

$$w_{\mathrm{Eff}} = \frac{f(\mathcal{R}) - 2f_{\mathcal{R}}(\dot{H} + 3H^2) - 5H\dot{f}_{\mathcal{R}} - \ddot{f}_{\mathcal{R}}}{-f(\mathcal{R}) + 6f_{\mathcal{R}}(H^2 + \dot{H}) - 3\dot{f}_{\mathcal{R}}^{\,2}/f_{\mathcal{R}} + 3H\dot{f}_{\mathcal{R}} + 3\ddot{f}_{\mathcal{R}}}. \tag{4.1}$$

Taking $w_{\mathrm{eff}} = -1$, a non-linear second-order equation for $f_{\mathcal{R}}$ is obtained

$$f_{\mathcal{R}}'' + f_{\mathcal{R}}'\left(\frac{E'}{2E} - 1\right) + f_{\mathcal{R}}\frac{E'}{E} - \frac{3}{2}\frac{f_{\mathcal{R}}'^2}{f_{\mathcal{R}}} = 0\,, \tag{4.2}$$

where the primes represent a differentiation with respect to $\ln a$. The background evolution is fixed through $E\left(a\right) \equiv H^2/H_0^2 = \Omega_{\mathrm{M}}a^{-3} + \Omega_{\mathrm{r}}a^{-4} + \Omega_{\mathrm{Eff}}a^{3\int_a^1(1+w_{\mathrm{Eff}})d\ln a}$. In a flat Universe, $\Omega_{\mathrm{Eff}} = 1 - \Omega_{\mathrm{M}} - \Omega_{\mathrm{r}}$, the solution of Eq. (4.2) retrieves a family of $f(\mathcal{R})$ functions that produce a background evolution indistinguishable from ΛCDM.

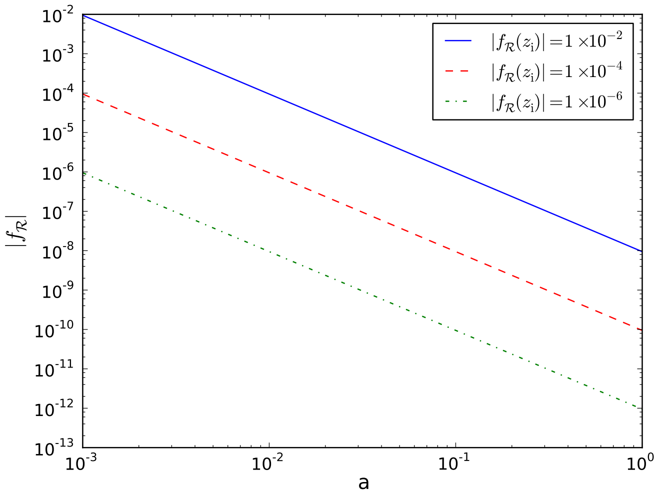

Figure 4.1 *Evolution of the absolute value of the additional scalar degree of freedom introduced in* $f(\mathcal{R})$ *theories,* $f_\mathcal{R}$*, as a function of the scale factor,* a*, with* $z_\mathrm{i} = 1000$*. The density parameter has been fixed to* $\Omega_\mathrm{m} = 0.30$*.*

The initial conditions for solving Eq. (4.2) are set at an initial scale factor, $a_\mathrm{i} = (1+z_\mathrm{i})^{-1} \ll 1$, by [138]

$$f_{\mathcal{R}\mathrm{i}} = C_1 a_\mathrm{i}^{-a_\mathrm{aux}} \left[\cosh\left(\frac{1}{2}\left[\ln a_\mathrm{i} + C_2\right]\sqrt{d}\right)\right]^{-2}, \tag{4.3}$$

$$f'_{\mathcal{R}\mathrm{i}} = -C_1 \frac{a_\mathrm{i}^{-a_\mathrm{aux}}}{\cosh\left(...\right)^2}\left[a_\mathrm{aux} + \sqrt{d}\tanh\left(...\right)\right], \tag{4.4}$$

where $d = a_\mathrm{aux}^2 - 2b$, $a_\mathrm{aux} = (5+6r_\mathrm{i})\,/\,(2+2r_\mathrm{i})$ and $b = (3+4r_\mathrm{i})\,/\,(1+r_\mathrm{i})$, with $r_\mathrm{i} = \Omega_\gamma\left(\Omega_\mathrm{M} a_\mathrm{i}\right)^{-1}$. The dotted argument of the hyperbolic tangent refers to the same argument as in the hyperbolic cosine. Throughout the chapter,the constant C_2 is defined large in order for the absolute value of the hyperbolic tangent to be close to unity. The constant C_1 is then fixed by choosing a value for $f_{\mathcal{R}\mathrm{i}} \equiv f_\mathcal{R}(z = z_\mathrm{i})$. Hence, one then just has to numerically evolve the model using Eq. (4.2), and make use of the background equations to recover further quantities of interest, such as $f(\mathcal{R})$, at each step of the iteration.

In Fig. 4.1 the evolution of the absolute value of $f_\mathcal{R}$ is plotted as a function of the scale factor for different initial values $f_{\mathcal{R}\mathrm{i}}$ set at a redshift $z_\mathrm{i} = 1000$. The scalar field $f_\mathcal{R}$ decays with time and is strongly suppressed as $a \to 1$.

As presented in Chapter 3, possible deviations at the background level from

ΛCDM have already been tested against observational data in Ref. [137] for other choices of the $f(\mathcal{R})$ function that do not recover the ΛCDM expansion history. Modifications introduced in the linear cosmological perturbations have not yet been tested for $f(\mathcal{R})$ gravity. Hence, the designer model discussed here suits this purpose, as it allows us to separate the modifications introduced between linear perturbations from background effects.

4.3 Linear Perturbations in $f(\mathcal{R})$ Gravity

It is necessary to present a review of the main aspects concerning the evolution of linear perturbations in the hybrid metric-Palatini theory. The full set of linearly perturbed Einstein and scalar field equations can be found in Ref. [138]. Typically for modified gravity theories (however, see [150, 152]), the hybrid metric-Palatini theory introduces a non-zero slip between the gravitational potentials in the Newtonian gauge, $\Phi = \delta g_{00}/2g_{00}$ and $\Psi = -\delta g_{\mathrm{ii}}/2g_{\mathrm{ii}}$.

Reference [46] introduces the perturbed Einstein equations in the Newtonian gauge. For this case the anisotropy equation is

$$\Phi - \Psi = \frac{\delta f_{\mathcal{R}}}{1 + f_{\mathcal{R}}}\,, \tag{4.5}$$

The evolution of $\delta f_{\mathcal{R}}$ is dictated by the linear perturbation of the scalar field equation of motion,

$$\begin{aligned} \delta \ddot{f}_{\mathcal{R}} + \delta \dot{f}_{\mathcal{R}} \left(2\mathcal{H} - \frac{\dot{f}_{\mathcal{R}}}{f_{\mathcal{R}}} \right) + \\ \delta f_{\mathcal{R}} \left(k^2 + \frac{\dot{f}_{\mathcal{R}}^{\,2}}{2 f_{\mathcal{R}}^{\,2}} + a^2 m^2_{f_{\mathcal{R}}} - \frac{\kappa^2}{3} a^2 T \right) + \\ \Psi \left(\frac{\dot{f}_{\mathcal{R}}^{\,2}}{f_{\mathcal{R}}} - 2\ddot{f}_{\mathcal{R}} - 4\dot{f}_{\mathcal{R}}\mathcal{H} \right) - \dot{f}_{\mathcal{R}} \left(3\dot{\Phi} + \dot{\Psi} \right) &= \frac{f_{\mathcal{R}}}{3} a^2 \kappa^2 \delta T, \end{aligned} \tag{4.6}$$

where δT denotes the linear perturbation of the trace of the stress-energy tensor, $T = -\rho + 3p$, and *for this equation only*, the overdots represent derivatives with respect to conformal time τ with $dt = a\, d\tau$, and $\mathcal{H} \equiv aH$.

It has been shown in Ref. [138] that the evolution of $\delta f_{\mathcal{R}}$ is characterised by quick oscillations around zero, which end up reflecting in the ratio between the Newtonian potentials, $\gamma \equiv \Phi/\Psi$. These fluctuations are scale dependent, moving faster and with larger amplitude at smaller scales. They can produce noticeable oscillations at near-horizon scales, depending on the initial value of the scalar field at early times that, for instance, have an impact on the Poisson equation. Due to the Hubble friction term in Eq. (4.6), these modifications eventually get damped as one approaches $a \approx 1$, becoming fairly negligible at the present with no signs of significant subhorizon changes.

The behavior of $\delta f_{\mathcal{R}}$ is explored further in Secs. 4.3.1 and 4.3.2, focusing on its subhorizon and early-time evolution behaviour, respectively, where accurate approximations for these regimes are developed. In order to test these approximations, Ref. [138] is followed and the exact numerical evolution of the gravitational potentials and $\delta f_{\mathcal{R}}$ is solved, using the linearly perturbed conservation equations for the stress-energy tensor and the first-order differential equations for the lensing potential, $\Phi_+ \equiv (\Phi + \Psi)/2$.

4.3.1 Subhorizon Approximation

The wavemodes that are deep within the Hubble radius with wavenumber $k \gg aH$ are considered first. To describe this limit, the quasistatic approximation is adopted, discarding time derivatives of perturbations when compared to their spatial variation. Generally, for Horndeski scalar-tensor theories, this is a good approximation on small scales [151]. In practice, this allows one to keep the terms proportional to k^2/a^2H^2 as well as those related to the matter perturbation $\delta\rho_{\rm m}$ and the scalar field effective mass $m^2_{f_{\mathcal{R}}}$. The latter sets a modified length scale that can be compared to that of the perturbations.

Applying the sub-horizon regime to Eq.(47) in Ref. [138],

$$\frac{k^2}{a^2}\Phi \approx \frac{1}{2\left(1+f_{\mathcal{R}}\right)}\left[\delta f_{\mathcal{R}}\left(\frac{k^2}{a^2}\right) - \kappa^2\delta\rho_{\rm M}\right] , \tag{4.7}$$

where $\delta\rho_{\rm M} \equiv \rho_{\rm M}\delta_{\rm M}$. Using this approximation in the anisotropy equation (4.5),

$$\frac{k^2}{a^2}\Psi \approx -\frac{1}{2\left(1+f_{\mathcal{R}}\right)}\left[\delta f_{\mathcal{R}}\left(\frac{k^2}{a^2}\right) + \kappa^2\delta\rho_{\rm M}\right] . \tag{4.8}$$

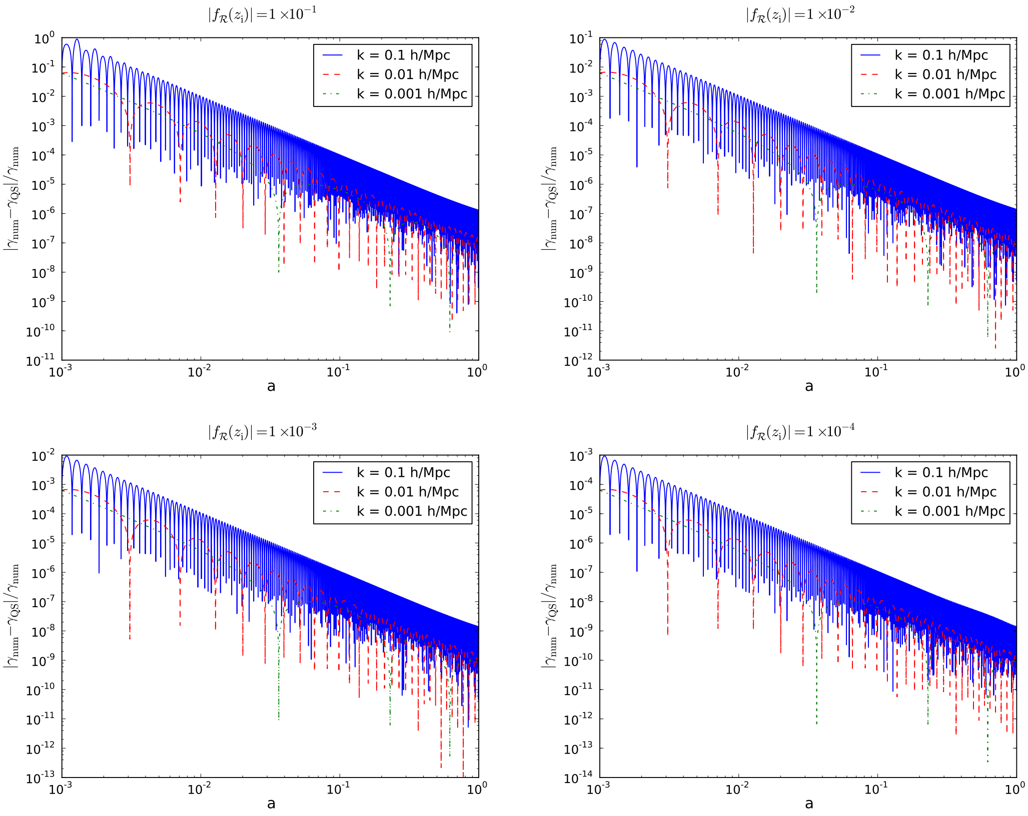

Figure 4.2 *Relative difference* $|\gamma_{\rm num} - \gamma_{\rm QS}|/\gamma_{\rm num}$ *between the numerical ratio* $\gamma \equiv \Phi/\Psi$ *and its quasistatic (QS) approximation given by Eq. (4.14). The redshift considered was* $z_{\rm i} = 1000$ *and the matter density parameter was fixed to* $\Omega_{\rm m} = 0.30$*.*

A similar approach can be calculated for $\delta f_{\mathcal{R}}$, from Eq. (4.6),

$$\delta f_{\mathcal{R}} \approx -\frac{H_0^2 E_{\rm M}}{k^2/a^2 + m_{f_{\mathcal{R}}}^2} f_{\mathcal{R}} \delta_{\rm M} \,, \tag{4.9}$$

which can be inserted back into Eqs. (4.7) and (4.8) such that

$$\frac{k^2}{a^2}\Phi \approx -\frac{H_0^2 E_{\rm M}\delta_{\rm M}}{2\left(1+f_{\mathcal{R}}\right)}\left[\frac{k^2/a^2\left(f_{\mathcal{R}}+3\right)+3m_{f_{\mathcal{R}}}^2}{k^2/a^2+m_{f_{\mathcal{R}}}^2}\right], \tag{4.10}$$

$$\frac{k^2}{a^2}\Psi \approx -\frac{H_0^2 E_{\rm M}\delta_{\rm M}}{2\left(1+f_{\mathcal{R}}\right)}\left[\frac{k^2/a^2\left(3-f_{\mathcal{R}}\right)+3m_{f_{\mathcal{R}}}^2}{k^2/a^2+m_{f_{\mathcal{R}}}^2}\right], \tag{4.11}$$

where $E_{\rm M} \equiv \Omega_{\rm M} a^{-3}$.

These approximations can, in turn, be used to obtain an expression for the lensing potential, Φ_+, in this regime:

$$\frac{k^2}{a^2}\Phi_+ \approx -\frac{3H_0^2 E_{\mathrm{M}}}{2\,(1+f_{\mathcal{R}})}\delta_{\mathrm{M}} \tag{4.12}$$

whereas the slip between the potentials, $\delta f_{\mathcal{R}}$, is given by

$$\delta f_{\mathcal{R}} \approx \frac{2}{3}\frac{k^2}{a^2}\frac{f_{\mathcal{R}}\Phi_+}{k^2/a^2 + m_{f_{\mathcal{R}}}^2}\,. \tag{4.13}$$

As mentioned in Sec. 3.1, the background value of the scalar field is required to be small in order for the metric-Palatini theory to avoid Solar-System tests. In these circumstances, the quasistatic modifications will be almost unnoticeable, even if the range of the modifications, given by the effective Compton wavelength $\lambda_{\mathrm{C}} = 2\pi/m_{f_{\mathcal{R}}}$, is relevant. For instance, note that for $f_{\mathcal{R}} \to 0$, $\delta f_{\mathcal{R}} \to 0$ since $\delta f_{\mathcal{R}}$ is proportional to the background value of the scalar field $f_{\mathcal{R}}$ in the quasistatic regime, as can be seen in Eq. (4.13).

The $f(\mathcal{R})$ models that have been analysed so far [137, 138] evolve towards smaller deviations from ΛCDM as the present approaches, with $f_{\mathcal{R}}$ tending to negligible values. This renders the modifications in the quasistatic regime subdominant, as was explicitly shown in Ref. [138] for the designer $f(\mathcal{R})$ model, with no mentionable enhancement of the perturbations in this regime when compared to ΛCDM.

In Fig. 4.2 the numerical evolution of the ratio between the Newtonian potentials, γ, is compared with its quasistatic approximation,

$$\gamma_{\mathrm{QS}} \equiv \frac{\Phi}{\Psi} = \frac{k^2/a^2\,(3+f_{\mathcal{R}}) + 3m_{f_{\mathcal{R}}}^2}{k^2/a^2\,(3-f_{\mathcal{R}}) + 3m_{f_{\mathcal{R}}}^2}\,. \tag{4.14}$$

The aforementioned figure shows that it is an accurate approximation at late times, as a consequence of large k/aH values. As the present time comes near, the subhorizon modifications of the model become suppressed, leading in turn to a very small difference between the compared values. This accuracy holds even when larger initial displacements for the scalar field $f_{\mathcal{R}\mathrm{i}}$ are considered.

However, the quasistatic approximation breaks down at earlier times, due to the oscillatory behavior of $\delta f_{\mathcal{R}}$ discussed in Sec. 4.3. This becomes more evident for the smaller scales, where the amplitude of the oscillations are larger. For large initial values of the scalar field the error can be of order unity and decreases as smaller values for the initial displacement are tested. Hence, for an accurate but computationally efficient description of the evolution of γ in the designer $f(\mathcal{R})$ model that is valid across a large range of redshifts and scales, some corrections must be applied to the subhorizon approximation (see Sec. 4.6.2).

These procedures will be explained in Sec. 4.4. Lastly, it is important to emphasise that in the hybrid metric-Palatini model, $f_{\mathcal{R}}$ and $\delta f_{\mathcal{R}}$ are strongly suppressed at the present, and $(G_{\text{eff}} - G)/G \ll 1$ at any scale, consistent with Solar-System tests. In contrast, in metric $f(R)$ gravity, for modes well within the Compton radius, we have $(G_{\text{eff}} - G)/G = 4/3$ at linear order, and the model needs to employ a nonlinear chameleon mechanism [37, 120, 147] to restore $G_{\text{eff}}/G \to 1$ at the small scales probed by Solar-System tests.

Unlike the chameleon mechanism, however, the suppression in the hybrid metric-Palatini model is independent of environment and cannot be tested by unscreened small objects in voids [109] or unscreened by environment-dependent statistical measurements of the large-scale structure [149]. It is for this aspect that we adopt the decaying early-time gravitational modification characterised by the hybrid metric-Palatini model rather than the decaying mode of metric $f(R)$ gravity, where an effective 4/3 enhancement of the gravitational coupling at late times would always be present at some level.

4.3.2 Early–Time Corrections

The dynamics of $\delta f_{\mathcal{R}}$ are dictated by Eq. (4.6), which is the equation of a damped harmonic oscillator with a driving force proportional to the matter perturbation. The frequency of the oscillation depends on the mode wavenumber k, while the damping term is dominated by the Hubble parameter at early times, and $\delta f_{\mathcal{R}}$ quickly becomes negligible towards late times, where the oscillations are no longer observable.

The driving term could deviate the equilibrium position of the oscillations. However, note that it is proportional to $f_{\mathcal{R}}$, which not only is fixed to a small value at early times as the focus of this study are small deviations from GR, but also evolves towards zero at late times, rendering the external force term almost negligible.

Hence, rewriting Eq. (4.6) to depend on $\ln a$, assuming $f_{\mathcal{R}}, \dot{f}_{\mathcal{R}} \ll 1$, but not neglecting terms proportional to $\dot{f_\mathcal{R}}/f_\mathcal{R}$, the resulting approximation is,

$$\delta f''_\mathcal{R} + \delta f_\mathcal{R}\left(\frac{k^2}{a^2H^2} + \frac{f'^2_\mathcal{R}}{2f^2_\mathcal{R}} + \frac{H_0^2\Omega_\mathrm{m}a^{-3}}{H^2}\right) + \delta f'_\mathcal{R}\left(3 + \frac{H'}{H} - \frac{f'_\mathcal{R}}{f_\mathcal{R}}\right) \approx 0\,, \quad (4.15)$$

for which a solution under the Wentzel–Kramers–Brillouin (WKB) approximation is given by

$$\delta f_\mathcal{R} \approx \frac{A}{\sqrt{2w}} a^{-\gamma_\mathrm{exp}} \cos\left(\int w\, d\ln a + \theta_0\right)\,. \quad (4.16)$$

The approximation is expected to be valid as long as the adiabatic condition $|\dot{w}| \ll w^2$ holds, where w^2 is the term multiplying $\delta f_\mathcal{R}$ in Eq. (4.15); and γ_exp is the quantity multiplying the $\delta f'_\mathcal{R}$ term in Eq. (4.15). The constants θ_0 and A can be fixed by imposing suitable initial conditions for $\delta f_\mathcal{R}$ and $\delta f'_\mathcal{R}$ at a chosen redshift.

For the $f(\mathcal{R})$ designer model, the ratio between $f'_\mathcal{R}$ and $f_\mathcal{R}$ can be easily calculated at early times using the initial conditions presented in Sec. 4.2. This yields

$$\frac{f'_\mathcal{R}}{f_\mathcal{R}} \approx \sqrt{d} - a_\mathrm{aux}\,, \quad (4.17)$$

Using Eq. (4.17), the w term of Eq. (4.16) can be simplified as

$$w \approx \left[\frac{k^2a^{-2}}{H_0^2E} + \frac{\left(a_\mathrm{aux} - \sqrt{d}\right)^2}{2} + \frac{\Omega_\mathrm{M}}{\Omega_\mathrm{M} + \Omega_\Lambda a^3}\right]^{1/2}\,, \quad (4.18)$$

where the presence of radiation has been neglected in the Hubble factor $H \equiv H_0\sqrt{E}$ since this approximation applies only for redshifts deep within the matter-dominated era. For $k \gg aH$, Eq. (4.18) can be further approximated by

$$w \approx \left(\frac{k^2}{a^2H_0^2E}\right)^{1/2}\left(1 + \frac{ba^2H_0^2E}{2k^2}\right)\,, \quad (4.19)$$

where

$$b = \left(a_\mathrm{aux} - \sqrt{d}\right)^2/2 + \Omega_\mathrm{M}/\left(\Omega_\mathrm{M} + \Omega_\Lambda a^3\right)\,, \quad (4.20)$$

which allows to perform an analytic integration of Eq. (4.16).

The result depends on hypergeometric functions that can, however, be approximated as unity. For simplicity, the result is presented without the presence of these functions:

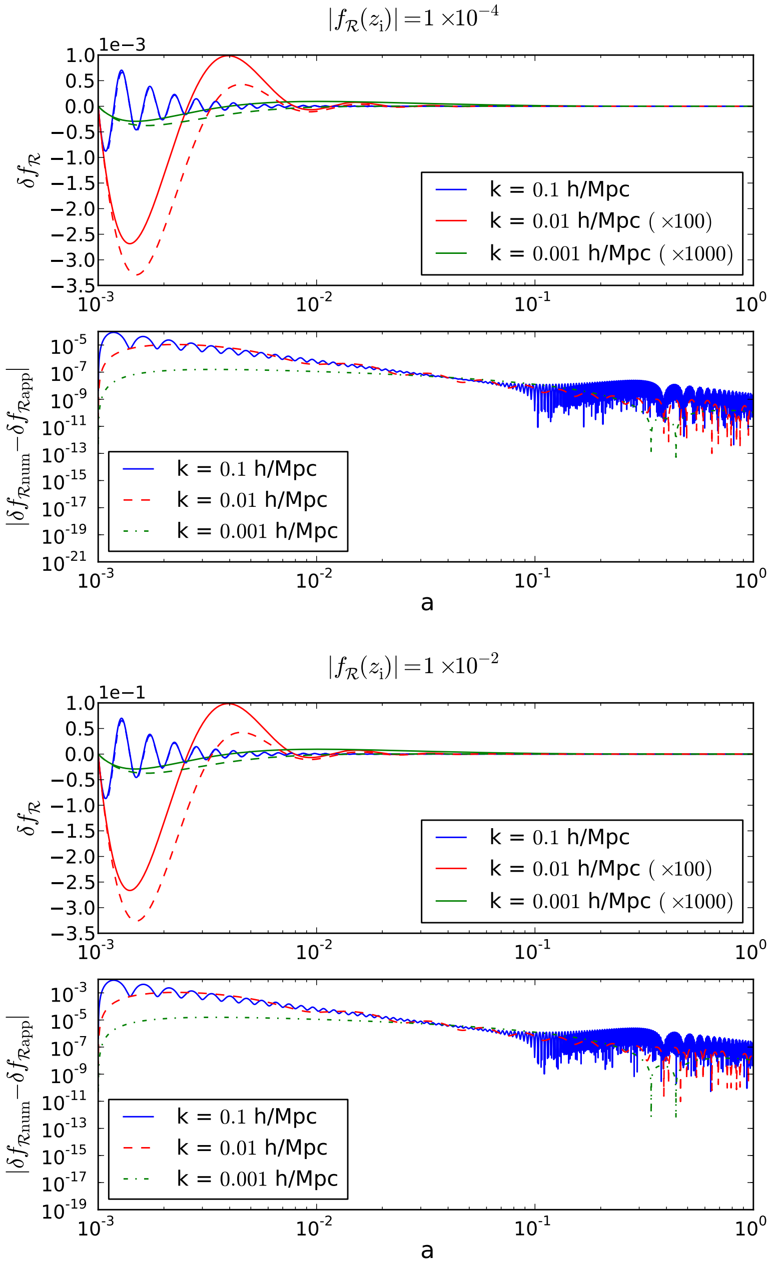

Figure 4.3 *The top panels show the numerical evolution (solid lines) of the perturbation* $\delta f_{\mathcal{R}}$ *against the evolution predicted by the analytical approximation (dashed lines) given by Eq. (4.16). The two largest scales have been enhanced by a factor of* 100 *and* 1000 *to be noticeable. The bottom panels show the absolute difference between the analytical approximation and the numerical results. The matter density parameter was fixed to* $\Omega_{\rm m} = 0.30$.

$$
\begin{aligned}
\int w d\ln a \;&\approx\; 2\left(\frac{k^2 a}{H_0^2\Omega_\mathrm{M}}\right)^{1/2} + \frac{\left[a_\mathrm{aux}-\sqrt{d}\right]^2}{4}\left(\frac{\Omega_\mathrm{M}H_0^2}{k^2 a}\right)^{1/2}\left(\sqrt{\frac{\Omega_\mathrm{M}}{\Omega_\Lambda}a^3+1}-3\right)\\
&-\; \Omega_\mathrm{M}\left(\frac{H_0^2}{k^2 a}\right)^{1/2} . \qquad (4.21)
\end{aligned}
$$

In the limit of $k \ll aH$, w can instead be approximated as

$$
w \approx \sqrt{b}\left(1+\frac{1}{2}\frac{k^2}{a^2H_0^2Eb}\right) . \qquad (4.22)
$$

To perform an analytic integration, the approximation $b \approx \left(a_\mathrm{aux}-\sqrt{d}\right)^2/2+1$ is used, which results in

$$
\int w d\ln a \approx \sqrt{b}+\frac{1}{2\sqrt{b}}\frac{k^2 a}{H_0^2\Omega_\mathrm{M}} . \qquad (4.23)
$$

The implementation of these approximations was compared in Eqs. (4.22) and (4.23) against numerical results in Fig. 4.3.

The initial conditions for $\delta f_\mathcal{R}$ are set by determining θ_0 such that $\delta f_\mathcal{R}$ is zero at the chosen initial redshift $z_\mathrm{i} = 1000$. This is a completely arbitrary choice, but not particularly relevant for the overall evolution of $\delta f_\mathcal{R}$ since it quickly oscillates around zero. Afterwards, Eq. (4.15) is differentiated with respect to $\ln a$ and the constant A is computed by calculating the numerical value of $\delta f'_\mathcal{R}$ using Eq. (67) of Ref. [138] at the same redshift.

It can be observed from Fig. 4.3 that the analytical approximation works remarkably well, considering the complexity of the equation describing the dynamics of $\delta f_\mathcal{R}$. Even though it may fail in predicting the exact amplitude of the oscillations, the relative difference to the numerical results is insignificantly small compared to the precision available with current experiments.

Also, it clearly encompasses the desired dependence on the scale of the modes of the perturbations, as for smaller scales (higher k) the amplitude and frequency of the oscillations grow higher.

Lastly, Fig. 4.3 serves as further confirmation of the viability of the subhorizon approximations derived in Sec. 4.3.1 at late times. As Eq. (4.13) dictates, $\delta f_\mathcal{R}$ should be strongly suppressed in the subhorizon regime following the behavior of the background scalar field value and with $k \gg aH$.

4.3.3 Embedding in Horndeski Gravity and Effective Field Theory

The hybrid metric-Palatini modification of gravity needs to decouple at high redshifts in order not to violate stringent high-curvature constraints from the CMB. However, the goal is to determine below which redshift $z_{\rm on}$ the modification can be introduced and to which degree a decaying early-time modification motivated by the evolution of hybrid metric-Palatini gravity at $z \leq z_{\rm on}$ can be constrained by the CMB radiation observed today.

In order to formulate an explicit realisation of the decaying early modified gravity model, the designer hybrid metric-Palatini scenario with high-redshift decoupling was embedded in the Horndeski scalar-tensor theory [101] using the effective field theory of cosmic acceleration, where the notation adopted is as in Ref. [25]. Reference [92] gives a very good review on EFT in this context. This calculation was performed and discussed by Lima, Lombriser and myself.

Given the ΛCDM background expansion history of the designer hybrid metric-Palatini model, its modifications are fully specified by the effective parameters characterising the linear perturbations,

$$\alpha_{\rm M} = \frac{f'_{\mathcal{R}}}{1+f_{\mathcal{R}}}, \qquad \alpha_{\rm K} = -\frac{3}{2}\frac{f'_{\mathcal{R}}}{f_{\mathcal{R}}}\alpha_{\rm M}, \qquad \alpha_{\rm B} = -\alpha_{\rm M}, \tag{4.24}$$

where $\alpha_{\rm M} \equiv (M_*^2)'/M_*^2$ describes the running of the Planck mass $\kappa^2 M_*^2 \equiv 1 + f_{\mathcal{R}}$; $\alpha_{\rm K}$ denotes the contribution of the kinetic energy of the scalar field; and $\alpha_{\rm B}$ determines the mixing of the kinetic contributions of the metric and scalar fields.

The decaying early modifications of gravity constrained here are therefore realised in a Horndeski scalar-tensor model with

$$\alpha_{\rm X,model} = \begin{cases} \alpha_{\rm X}, & z \leq z_{\rm on}, \\ 0, & z > z_{\rm on}, \end{cases} \tag{4.25}$$

where the $\alpha_{\rm X}$ are given by Eq. (4.24) according to hybrid metric–Palatini gravity. Note that $\alpha_{\rm X,model}(z > z_{\rm on}) = 0$ recovers a ΛCDM universe at high redshifts, avoiding the rigorous high-curvature bounds at very early times.

In the code, this translates as setting the variable $\chi = \delta f_{\mathcal{R}} = 0$, and allowing its evolution to commence after a given redshift. A question may be raised about the sensitivity of the solutions given their step function behaviour. To test for this, first the code was run with $z = 1000, 500, 100$. Upon running the three cases, for $z = 1000$ the transition was very smooth. For $z = 500$ and $z = 100$, the discontinuity existed, but it was very small. In all three attempts the program finished all calculations without breaking down. In order to smooth the transitions, tests were carried out using a hyperbolic tangent function instead of a step. For all three cases, the results were the same. Therefore, it was decided to drop the hyperbolic tangent case and continue without it.

Stability of the background solution of the Horndeski model with respect to the scalar mode requires [25]

$$Q_{\rm s} \equiv \frac{2M_*^2 D}{(2-\alpha_{\rm B})^2} > 0\,, \tag{4.26}$$

where

$$D \equiv \alpha_{\rm K} + \frac{3}{2}\alpha_{\rm B}^2 = -\frac{3f_{\mathcal{R}}'^2}{2f_{\mathcal{R}}(1+f_{\mathcal{R}})^2}\,. \tag{4.27}$$

With the evolution of $f_{\mathcal{R}}$ given by hybrid metric-Palatini theory, $Q_{\rm s}$ is

$$Q_{\rm s} = \begin{cases} < 0\,, & \text{for } f_{\mathcal{R}} > 0\,, \\ > 0\,, & \text{for } f_{\mathcal{R}} < 0\,. \end{cases} \tag{4.28}$$

Hence, $-1 < f_{\mathcal{R}} < 0$ is required to prevent ghost instabilities. To avoid a gradient instability or a superluminal sound speed $c_{\rm s}$ of the scalar field perturbation, it is required that $0 < c_{\rm s}^2 \leq 1$. To check this, $c_{\rm s}^2$ is computed in the hybrid metric-Palatini theory,

$$\begin{aligned} D \cdot c_{\rm s}^2 \;&=\; \frac{\kappa^2}{H^2(1+f_{\mathcal{R}})}\left(\frac{4}{3}\rho_{\rm r} + \rho_{\rm M}\right)\left(f_{\mathcal{R}} + \frac{f_{\mathcal{R}}'}{2}\right) \\ &\quad + \frac{\alpha_{\rm M}}{2}\left(\frac{f_{\mathcal{R}}' + 2(1+f_{\mathcal{R}})}{1+f_{\mathcal{R}}}\right) - \frac{f_{\mathcal{R}}'' - (f_{\mathcal{R}}')^2}{1+f_{\mathcal{R}}}\,. \end{aligned} \tag{4.29}$$

Furthermore, for the designer model used in this work

$$f_{\mathcal{R}}' = \begin{cases} > 0\,, & \text{for } f_{\mathcal{R}} < 0\,, \\ < 0\,, & \text{for } f_{\mathcal{R}} > 0\,, \end{cases} \tag{4.30}$$

and $|f_{\mathcal{R}}'| \gg |f_{\mathcal{R}}|$. Therefore, for $f_{\mathcal{R}} < 0$, $f_{\mathcal{R}} + f_{\mathcal{R}}'/2 > 0$. Also, $f_{\mathcal{R}}''$ will be negative-definite (as can be verified by differentiating Eq. (4.4)) for negative values of the scalar field. All of this, in conjunction with the fact that $\alpha_{\mathrm{M}} > 0$ and $D > 0$, ensures that $c_{\mathrm{s}}^2 > 0$ for $-1 < f_{\mathcal{R}} < 0$.

It has also been confirmed numerically that c_{s} is subluminal for the range of values considered for $f_{\mathcal{R}\mathrm{i}}$. Whereas the condition for avoiding ghost instabilities applies to all hybrid metric-Palatini gravity models and should be respected when designing any other $f(\mathcal{R})$ models, the condition for avoiding gradient instabilities may be model dependent and should be studied in more detail for other choices of $f(\mathcal{R})$.

For completeness, the stability of tensor modes [25] with $Q_{\mathrm{T}} \propto \kappa^2 M_\star^2 = 1 + f_{\mathcal{R}} > 0$ whenever $f_{\mathcal{R}} > -1$ was also verified. In $f(\mathcal{R})$ models, the propagation speed of gravitational waves equals the speed of light $c_{\mathrm{T}} = 1$.

4.4 Implementation in MGCAMB

In order to compute the CMB observables, the early decaying modified gravity model was implemented in the publicly available MGCAMB code [98], a modified version of the also public CAMB code [134] that allows one to study the effects of modified gravity models on the CMB through modifications of the linear equations describing the growth of perturbations. This code implementation was programmed by Lima and myself, and it was heavily based on the modules I developed for the study presented in Chapter 3.

MGCAMB works by parametrising the evolution of the gravitational potentials through two time- and scale-dependent functions: the ratio of the metric potentials $\gamma(a,k) \equiv \Phi/\Psi$ and the effective modified gravitational coupling in the Poisson equation, $\mu(a,k) = G_{\mathrm{Eff}}/G$. The framework of MGCAMB is general enough to include possible early-time effects, hence it is well-suited for testing the hybrid metric-Palatini theory. Moreover, MGCAMB accepts the use of the approximations described in Secs. 4.3.1 and 4.3.2 to improve computational efficiency without loss of accuracy.

The model was implemented by modifying both γ and μ in the code. For γ the subhorizon approximation described in Eq. (4.14) was used and an oscillatory term described by $\delta f_{\mathcal{R}}$ was added to account for the early-time oscillations. From

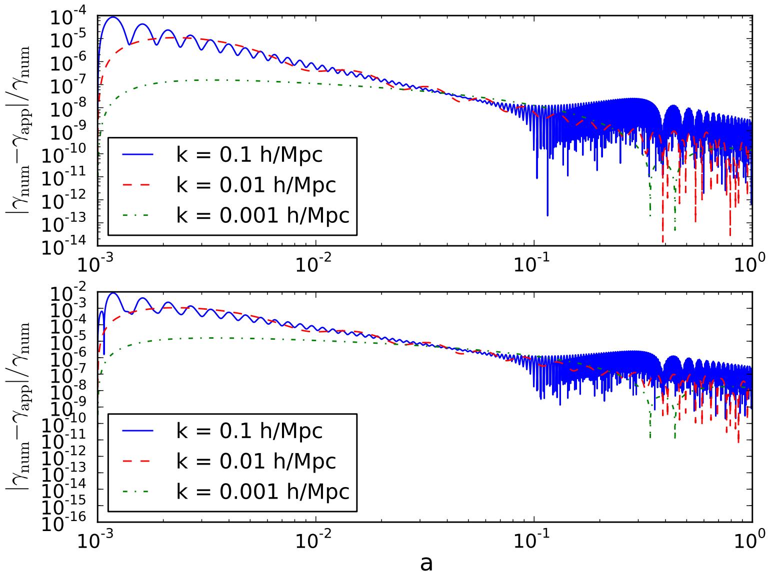

Figure 4.4 *Relative difference between the numerical evolution of* $\gamma \equiv \Phi/\Psi$ *and the approximation in Eq. (4.32). The top panel shows* $|f_{\mathcal{R}{\rm i}}| = 10^{-4}$ *and the lower panel shows* $|f_{\mathcal{R}{\rm i}}| = 10^{-2}$. *Once more, the matter density parameter was fixed to* $\Omega_{\rm M} = 0.30$.

Ref. [138] the gravitational potentials can be expressed as

$$\Phi = \Phi_+ + \frac{\delta f_\mathcal{R}}{2(1+f_\mathcal{R})}\,, \quad \Psi = \Phi_+ - \frac{\delta f_\mathcal{R}}{2(1+f_\mathcal{R})}\,, \tag{4.31}$$

which uses the observation that the early-time oscillations in $\delta f_\mathcal{R}$ do not affect the lensing potential Φ_+ for small-enough values of the amplitude of the oscillations.

The potential Φ_+ has an approximately constant value of unity throughout the matter dominated era. Therefore, with $\Phi_+ \gg \delta f_\mathcal{R}$ one can perform a Taylor expansion on the ratio between the potentials that results in

$$\gamma = \frac{\Phi}{\Psi} \approx 1 - \frac{\delta f_\mathcal{R}}{(1+f_\mathcal{R})}\,. \tag{4.32}$$

This approximation was compared against numerical results in Fig. 4.4, finding good agreement between the two, at an accuracy comparable to that observed in Fig. 4.3 for the slip between the metric potentials. Given this result, $\gamma_{\rm QS}$ is generalised with the simple modification

$$\gamma_{\rm MG} \approx \gamma_{\rm QS} + \frac{\delta f_\mathcal{R}}{1+f_\mathcal{R}}, \tag{4.33}$$

where $\gamma_{\rm QS}$ can be found in Eq. (4.14). Correspondingly, μ is modified to include the effect of the oscillations in the Poisson equation such that

$$\mu_{\rm MG} = \mu_{\rm QS} + \frac{\delta f_{\mathcal{R}}}{2(1+f_{\mathcal{R}})} , \tag{4.34}$$

where $\mu_{\rm QS}$ is given in Eq. (4.11). Finally, the initial conditions required to solve for the background evolution of the models were always set at the redshift $z_{\rm i} = 1000$.

As described in Sec. 4.3.3, through an embedding in the effective field theory of Horndeski gravity, the model is designed to behave as ΛCDM at the level of linear perturbations down to a redshift $z_{\rm on}$, at which point the modifications are introduced. At redshift $z_{\rm i}$, $\delta f_{\mathcal{R}} = 0$, with its subsequent evolution being determined by Eq. (4.16).

4.5 Cosmological Observables

After specifying a theoretically consistent decaying early modified gravity model in Sec. 4.2, the different probes used in this analysis are introduced. The results of Secs. 4.5- 4.6.2 were obtained by Lima and myself.

4.5.1 Geometric Probes

The comparison between the luminosity magnitudes of high-redshift to low-redshift supernovae Type Ia (SNe Ia) provides a relative distance measure affected by the Universe's expansion rate. Complementary absolute distance measures are obtained from measuring the local Hubble constant H_0 and the baryon acoustic oscillations (BAO) in the clustering of galaxies.

These probes constrain the cosmological background evolution and since the $f(\mathcal{R})$ models considered here are designed to match the ΛCDM expansion history, they only serve to constrain the standard cosmological parameters and prevent degeneracies with the effect of the additional scalar degree of freedom on the fluctuations.

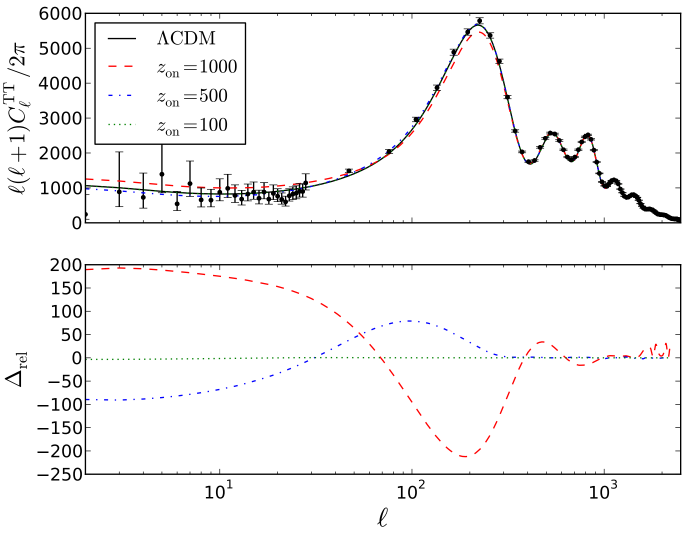

Figure 4.5 *The lensed CMB temperature anisotropy power spectrum predicted by the designer hybrid metric-Palatini model for* $|f_{\mathcal{R}}(z_{\mathrm{i}})| = 5 \times 10^{-2}$ *and different values of* z_{on} *as well as the prediction for the* Λ*CDM model (top panel). The lower panel shows the difference to* Λ*CDM,* $\Delta_{\mathrm{rel}} = \ell(\ell+1)\left(C_\ell^{TT,\mathrm{hybrid}} - C_\ell^{TT,\Lambda}\right)/(2\pi)$.

4.5.2 Cosmic Microwave Background

In addition to the geometric probes, the acoustic peaks in the CMB also contain information on the absolute distance to the last-scattering surface. These peaks are affected by early-time departures from GR at high curvature, i.e., in the case of $f(\mathcal{R})$ modifications, where z_{on} is sufficiently large. Gravitational modifications can generally further manifest themselves in the CMB temperature and polarisation via secondary anisotropies. Details on the numerical computation of these effects in the designer hybrid metric-Palatini model were covered in Sec. 4.4.

In Fig. 4.5, the predictions for the CMB temperature anisotropy power spectrum (TT) for three different choices of z_{on} are shown. Hence, the oscillations are introduced between the Newtonian potentials in distinct epochs of the cosmological evolution which in turn produces different effects in the observed power spectrum. The first immediate observation is that, the later these oscillations are introduced, the less significant is their impact on the TT power spectrum. This is mainly due to the fact that, at later epochs, the amplitude of the oscillations have already been considerably damped out, reducing their effect on the TT power spectrum.

The second noticeable modification of the spectrum is in the Sachs-Wolfe plateau, on scales around $\ell < 100$, where a shift towards higher or smaller values compared to ΛCDM is observed. A combination of gravitational redshift and intrinsic temperature fluctuations at angular last-scattering, can lead to a variation of the temperature power spectrum like: [16, 186]

$$\left.\frac{\delta T}{T}\right|_O = \left.\frac{\delta T}{T}\right|_E + e^{\mathrm{i}} v_{\mathrm{i}}|_O^E + \Psi_E + \int_E^O \left(\frac{\partial \Psi}{\partial \eta} - \frac{\partial \Phi}{\partial \eta} \right) d\eta, \tag{4.35}$$

where the first term on the r.h.s. is the intrinsic temperature fluctuation, the second is the Doppler shift, the third is the Sachs-Wolfe (SW) effect and the fourth is the integrated Sachs-Wolfe (ISW) effect. In general, the SW effect does not contribute much to dark energy models because at early times ρ_{DE} is mostly negligible. However, the ISW term is a line-of-sight term and does therefore contain potentially much information on the recent Universe. Moreover, the gravitational potential is constant for a matter-dominated Universe and therefore yields no ISW signal. This shows that the ISW effect is a direct diagnostic of something which is not ordinary pressureless matter: Dark Energy! [16]

The designer hybrid-metric Palatini model introduces modifications close to the surface of last-scattering. Therefore, depending on the redshift chosen to start the oscillations, the Newtonian potential Φ will be displaced toward larger or smaller values compared to ΛCDM, leading to the shift observed in the power spectrum. Then, at low ℓ, the traditional increase in power due to the ISW effect in the presence of late-time dark energy is seen. The designer model clearly mimics ΛCDM due to the fact that the background evolution is fixed to match the standard cosmological scenario, even if the power can be deviated toward lower or smaller values due to the ISW effect discussed before.

Finally, when the oscillations are introduced at $z_{\mathrm{on}} = 1000$, a significant decrease in the amplitude of the first peak becomes noticeable. Traditionally, at early times, the non-negligible presence of radiation after the epoch of last-scattering can cause a decay of the gravitational potentials before these become constant, contributing to an early ISW effect that can influence the amplitude and position of the peaks. Therefore, if modified gravity is allowed to be relevant close to the epoch of recombination, not only is this decay modified, but it also causes an additional variation, influencing the acoustic phenomenology of the CMB. Of course, as lower values of z_{on} are tested, this effect becomes increasingly negligible.

4.6 Cosmological Constraints

Before presenting the current cosmological constraints on decaying early modified gravity, the astrophysical datasets used in this analysis are briefly described. Later on, the constraints are presented. Finally, an outlook on constraints that can be obtained with 21 cm surveys and gravitational wave observations is analysed.

4.6.1 Datasets

For the SN Ia luminosity-redshift relation, the dataset compiled in the Joint Lightcurve Analysis (JLA) [29] was used. This includes records from the full three years of the Sloan Digital Sky Survey (SDSS) survey plus the “C11 compilation” assembled by Conley et al. (2011); comprising supernovae from the Supernovae Legacy Survey (SNLS), the Hubble Space Telescope (HST) and several nearby experiments. This whole sample consists of 740 SNe Ia.

For H_0, the information provided by the Wide Field Camera 3 (WFC3) on HST was included. The objective of this project was to determine the Hubble constant from optical and infrared observations of over 600 Cepheid variables in the host galaxies of 8 SNe Ia, which provide the calibration for a magnitude-redshift relation based on 240 SNe Ia [184]. Hence, the Gaussian prior of $H_0 = 73.8 \pm 2.4$ km s^{-1} Mpc^{-1} was used.

BAO observations were also included. These were the 6dF Galaxy Redshift Survey (6dFGRS) at low redshift $z_{\text{Eff}} = 0.106$ [30], as well as DR7 MGS from SDSS at $z_{\text{Eff}} = 0.15$, from the value-added galaxy catalogs hosted by NYU (NYU-VAGC) [185] and the BAO signal from the Baryon Oscillation Spectroscopic Survey (BOSS) DR11 at $z_{\text{eff}} = 0.57$ [19].

Lastly, the Planck 2015 data for the CMB was added. The Planck temperature and polarisation and Planck lensing likelihood codes may be found in the Planck Legacy Archive [5].

$z_{\rm on}$	$\mathrm{sgn}(f_{\mathcal{R}})$	$\lvert f_{\mathcal{R}\mathrm{i}}\rvert \equiv \lvert f_{\mathcal{R}}(z_{\rm i})\rvert$	$\lvert f_{\mathcal{R}}(z_{\rm on})\rvert$	$\lvert f_{\mathcal{R}}(z=0)\rvert$
1000	$\pm$	$< 1.3 \times 10^{-2}$	$< 1.3 \times 10^{-2}$	$< 1.3 \times 10^{-8}$
500	$\pm$	$< 4.7 \times 10^{-2}$	$< 1.2 \times 10^{-2}$	$< 4.7 \times 10^{-8}$
100	$\pm$	—	—	—
1000	$-$	$< 1.1 \times 10^{-2}$	$< 1.1 \times 10^{-2}$	$< 1.1 \times 10^{-8}$
500	$-$	$< 4.8 \times 10^{-2}$	$< 1.2 \times 10^{-2}$	$< 4.8 \times 10^{-8}$
100	$-$	—	—	—

Table 4.1: Current constraints (95% C.L.) on $f_{\mathcal{R}}(z_{\rm i} = 1000)$ from the combination of surveys discussed in Sec. 4.6.1. Note that models with a positive sign of $f_{\mathcal{R}}$ suffer from a ghost instability (see Sec. 4.3.3) and models with $z_{\rm on} = 100$ cannot be constrained within the prior $|f_{\mathcal{R}\mathrm{i}}| < 0.1$ required for the viability of the approximations performed in Sec. 4.3.2. However, a constraint of $|f_{\mathcal{R}\mathrm{i}}| \lesssim 10^{-3}$ on all models will be achievable with 21 cm intensity mapping (see Sec. 4.6.3). We also present constraints on the value of $f_{\mathcal{R}}$ at the redshift of decoupling, $z_{\rm on}$, and at the present time, $z = 0$.

4.6.2 Constraints

Using the datasets described above, an MCMC parameter estimation analysis was conducted with COSMOMC [133], with the approximations described in Sec. 4.4. The constraints are summarised on the early-time decaying modified gravity model in Table 4.1. It is easily noticeable that the constraining power of the data over the model changes significantly the later the oscillations between the Newtonian potentials ($z \leq z_{\rm on}$) are introduced.

For $z_{\rm on} = 1000$, allowing both signs for $f_{\mathcal{R}\mathrm{i}} \equiv f_{\mathcal{R}}(z_{\rm i} = 1000)$, a 1D-marginalised constraint of $|f_{\mathcal{R}\mathrm{i}}| < 1.3 \times 10^{-2}$ (95% C.L.) is inferred, where a flat symmetric prior $f_{\mathcal{R}\mathrm{i}} \in [-0.1, 0.1]$ was adopted. However, positive values of $f_{\mathcal{R}\mathrm{i}}$ are affected by the ghost instability discussed in Sec. 4.3.3. Considering the stable branch only with a negative flat prior, it is found that $|f_{\mathcal{R}\mathrm{i}}| < 1.1 \times 10^{-2}$.

These values are comparable to the constraints obtained in Ref. [137] on $f(\mathcal{R})$ models that deviate from the ΛCDM expansion history, using background data alone. Although these constraints have been inferred for initial modifications at much higher redshift. ΛCDM is clearly the favored model and no evidence for early-time modifications in the observations was found.

The constraints derived are mostly driven by two prominent effects on the CMB that were observed in Sec. 4.5.2: a modification of the Sachs-Wolfe plateau and of the amplitude of the first peak. However, there is also a non-negligible contribution of CMB lensing, which is sensitive to percent-level modifications at high ℓ [43] and can constrain the effects of $z_{\rm on} = 1000$ shown in Fig. 4.5. Also, the present absolute value of the scalar field, $|f_{\mathcal{R}0}| \equiv |f_{\mathcal{R}}(z = 0)|$, is very small and of order 10^{-8}. This implies that modifications are strongly suppressed at the smallest scales, where these are proportional to the background value of the scalar field [96], as was discussed in Sec. 4.3.

Finally, decreasing $z_{\rm on}$ leads to a considerable weakening of the constraints on the early-time deviation from GR. With $z_{\rm on} = 500$, constraints on the scalar field value at equal redshift weaken by a factor of approximately 4. For $z_{\rm on} = 100$, the scalar field value within the prior $|f_{\mathcal{R}\rm i}| < 0.1$ can no longer be constrained. This is due to the oscillations on the slip between the gravitational potentials being significantly damped out by $z = 100$, hence only introducing very small deviations from GR.

4.6.3 Outlook: 21 cm and Gravitational Waves

Finally, rough estimates on future constraints on early decaying modified gravity are provided. These will be achievable with 21 cm intensity mapping [38, 95, 160] and standard sirens [100, 152, 195] using gravitational waves emitted by events at cosmological distances. These constraints were derived by Lombriser.

To estimate constraints obtainable with 21 cm surveys, the deviations in the matter power spectrum between the model and ΛCDM are compared to bounds on modified gravity reported in Ref. [38] at $z = 11$ and Ref. [95] at $z = 2.5$. It was found that $|f_{\mathcal{R}\rm i}| \lesssim 10^{-3}$ and $|f_{\mathcal{R}\rm i}| \lesssim 5 \times 10^{-2}$ for $z_{\rm on} = 1000$, which is competitive with the CMB constraints in Table 4.1.

Standard sirens will constrain the luminosity distance at $z \sim (1-2)$ at the $\sim 1\%$ level, and at the $\sim 10\%$ level for $z \sim 7$ [64, 217]. In modified gravity models, this constraint can be used to set a bound on the evolution of the Planck mass [152], which for the present model corresponds to a constraint of $|f_{\mathcal{R}\rm i}| \lesssim 10^{3}$, which will not be competitive with the constraints in Table 4.1.

4.7 Conclusions

This chapter explored the current cosmological constraints that can be inferred on modifications of gravity which may become significant at early times after recombination and decay towards the present.

The designer hybrid metric-Palatini model was chosen as a specific example of an early-time modification of gravity. Fixing the background evolution to exactly match ΛCDM, allows one to separate background constraints from constraints inferred from the modified dynamics of linear perturbations due to the impact that these have on the CMB.

It is also described how this model can be realised in the more general context of the effective field theory formalism of Horndeski gravity, including a study of its stability. The outcome shows that the model is stable as long as the additional scalar degree of freedom introduced by the hybrid metric-Palatini theory remains negative with an amplitude smaller than unity, which implies an effective enhancement of the gravitational coupling.

In order to perform efficient numerical computations, an approximation for the evolution of the slip between the Newtonian potentials has been developed. This extension is valid beyond the standard quasistatic subhorizon approximation, and becomes important at high redshifts, where it is shown that a quasistatic approach alone breaks down due to the known oscillations of the linear perturbations of the model [138].

Using a combination of observational data on the background evolution and of the CMB anisotropies, constraints on the allowed early-time deviations from GR were inferred. The results obtained are dependent on the redshift at which the oscillations are introduced in the slip between the gravitational potentials. If these are set at $z_{\rm on} = 1000$, the absolute deviation from GR at $z_{\rm on}$ can be constrained to $\lesssim 10^{-2}$ at the 95% confidence level. This result is comparable to the constraints obtained from background data alone in Ref. [137] for $f(\mathcal{R})$ models that depart from the ΛCDM expansion history.

The constraints achieved at this redshift can be attributed to noticeable effects on the CMB power spectrum. A substantial shift in the Sachs-Wolfe plateau is observed due to a modification of the Newtonian potential Φ at a time close to recombination. There is also a significant suppression of the first peak due to complementary variation of the gravitational potentials close to the epoch of recombination that, together with the non-negligible presence of radiation, contributes to an early integrated Sachs-Wolfe effect that can alter the amplitude and position of the peaks. Smaller contributions to the constraints can be attributed to CMB lensing which is sensitive to the percent-level modifications observed at high ℓ. Finally, it is found that the future 21 cm survey data will significantly improve upon the CMB constraints, whereas using gravitational wave events as standard sirens will not provide competitive bounds.

Chapter 5

Constraints on the field-roll during inflation

5.1 Introduction

The present chapter, in the same manner as the ones before, describes a project based on data analysis. However, in contrast to the late-time acceleration characterisations of the previous pages, it is centred around the theory of inflation.

The spatial flatness of the Universe, and its density perturbation before cosmological scales enter the horizon, strongly point to a period of almost exponential inflation as its initial condition. This could have begun much earlier than the time when the observable Universe leaves the horizon and it most likely lasted for at least 50-60 e-folds.

Inflation is also expected to have generated tensor perturbations, also known as gravitational waves. A detection of the latter would be compelling evidence of the existence of inflation. In terms of the standard parametrisation used in cosmology, this can be achieved by measuring the ratio of tensor to scalar perturbations, r [103].

One of the most attractive inflation frameworks is the slow-roll mechanism. In it, the energy density is dominated by the almost constant inflaton potential $V(\phi)$. This guarantees that the inflaton field ϕ rolls very slowly [34].

As mentioned in Section (1.3.2), slow-roll inflation is identified with two parameters, ϵ and η. During inflation $\epsilon < 1$, and this period ends when $\epsilon = 1$. The tensor to scalar ratio r is only dependent on ϵ [103]. If ϵ is assumed to increase monotonically (as is the case with many inflationary models) then it is possible to derive a connection between r and the change in the inflaton field value $\Delta\phi$, over a range of e-folds ΔN. This relationship places an upper limit on the value of r,

$$r \sim 0.0032 \left(\frac{50}{\Delta N}\right)^2 \left(\frac{\Delta\phi}{M_{\rm Pl}}\right)^2 . \tag{5.1}$$

This is known as the Lyth bound [156]. Moreover, from an observational point of view, the idea that ϵ is increasing during inflation is favoured, as the evidence shows that for a certain number of e-folds, the scalar power spectrum is tilted to red. Nonetheless, the application of the Lyth bound is difficult for two reasons:

1. It is not known for how many e-folds ϵ is increasing.
2. In many theories (e.g. supergravity), quantum corrections to a potential are expected to be of the form $(\phi/M_{\rm Pl})^n$. As such, the value that the bound on the tensor to scalar ratio r imposes on $\Delta\phi$ can have different effects:
    - $\phi \ll M_{\rm Pl}$: no changes. The corrections to the potential can be ignored.
    - $\phi < M_{\rm Pl}$: still solvable. The corrections to the potential can be included, or a symmetry can be found for them that excludes them for low values of n.
    - $\phi \geq M_{\rm Pl}$: no solution. The quantum corrections would lead to a non-flat inflationary potential.

Some of the attempts to apply the Lyth bound have assumed that ϵ increases during the whole duration of the inflationary epoch. An example of this is “hilltop inflation” [34]. However, the tensor fraction achieved with this model is so tiny ($r \lesssim 0.002$), that the data will never tell us if this model is visible or not.

On the other hand, there exists a variety of potentials of phenomenological nature where ϵ can increase for an e-fold period, and decrease rapidly outside of the range where the scalar power spectrum is observed. This behaviour weakens the restrictiveness of the Lyth bound, because for most of the inflationary period ϵ can be very small, and therefore the scalar field rolls very little, avoiding the dangers of quantum corrections for such potentials.

At the time of the detection of primordial curl patterns (first interpreted as due to tensors) by the Bicep2 experiment [6] (later proved erroneous) the development of these kind of theories achieved a peak, with many of them claiming to have found a model that fitted the observations [26, 58, 168, 182, 197].

Unfortunately, such models tend to be tested by comparing the amplitude $\mathcal{A}_{\mathrm{s}}$ and spectral index n_{s} at the pivot scale given by *Planck*. This is insufficient proof that these theories fit the observations, because the constraints given by *Planck* are obtained by assuming a power law shape of the initial power spectrum $P(k)$. In contrast, the tested models have a power spectrum that is necessarily different from a power law, in order for ϵ to decrease unusually rapidly outside the range of visible multipoles, or even within the observable range of scales, in some cases.

In fact, for these cases, $\mathcal{P}_{\mathrm{s}}(k)$ changes dramatically outside of the observation span. It would then be most desirable to have a test of the initial power spectrum for every model, which can be used to verify if the model matches the CMB's range, or not. But doing this in a rigorous manner is very hard, because, as mentioned before, it is not known exactly up to which scale the red-tilted power spectrum behaviour of the scalar power spectrum ends. [102].

Instead of focusing on specific models, the purpose of this project is to measure the minimum rolling of the field $\Delta\phi$ that can still fit the CMB temperature data, given a certain value of the tensor to scalar ratio r. If, in the future, a detection of r occurs, it will provide information about the tensor modes, which, joined with the scalar ones, can be used to obtain the acceleration trajectory of inflation. The latter can then be employed to get $\phi(k)$ given an initial ϕ_{i}.

The upper limit of $\Delta\phi$ is not interesting, because ϵ, which is always positive, could become so large that $\Delta\phi \gg 1$ is always a possibility. However, the lower limit $\Delta\phi$ found in this project will provide a restriction that, for a hopefully detected constraint on r, every viable model will have to reproduce.

This chapter is an ongoing piece of research conducted in collaboration with Shaun Hotchkiss, Sam Young, Christian Byrnes and Andrew Liddle. The individual and joint contributions to this work will be highlighted in each segment.

5.2 The shape of the acceleration during the inflationary epoch

The first step towards achieving a constraint on $\Delta\phi$ is to have a suitable parametrisation of the Universe's acceleration history during inflation. In order to characterise this, the formalism described in Contaldi 2014 [61] has been set up in the July 2015 version of CAMB/COSMOMC [133, 134], introducing changes in the methodology equations plus a different choice of prior, parametrisation and dataset combination. The backbone of this project, is, however, heavily based on the work depicted in Ref. [61].

Assuming a Friedmann-Robertson-Walker background with scale factor $a(t)$, the quantity ϵ measures the acceleration in the scale factor a

$$\epsilon = -\frac{\dot{H}}{H^2}, \tag{5.2}$$

where $H = \dot{a}/a$ is the Hubble rate and overdots represent derivatives with respect to time t.

Assuming single field inflation, as described in Section (1.3.2), Eq. (1.39) describing the motion of the inflaton can be combined with Hubble Eq. (1.40), to relate the acceleration parameter ϵ_{acc} to the time derivative of the inflaton

$$\epsilon = \frac{1}{2M_{\mathrm{Pl}}^2}\left(\frac{\dot{\phi}}{H}\right)^2. \tag{5.3}$$

Substituting the above into Eq. (1.40), a relationship is obtained between ϵ_{acc}, H and the scalar potential

$$V[\epsilon_{\mathrm{acc}}(N)] = 3M_{\mathrm{Pl}}^2 H^2(N)\left[1 - \frac{\epsilon_{\mathrm{acc}}(N)}{3}\right], \tag{5.4}$$

where quantities have been expressed in terms of e-folds defined as $N = \ln(a/a_0)$.

In turn, ϕ can be related to ϵ_{acc} by Eq. (5.3)

$$\frac{\phi - \phi_0}{M_{\mathrm{Pl}}} = \frac{\Delta\phi}{M_{\mathrm{Pl}}} = \sqrt{2}\int_0^N \sqrt{\epsilon_{\mathrm{acc}}(N')}dN'. \tag{5.5}$$

The integration of ϵ_{acc} results in an expression for the Hubble rate valid at every

e-fold N

$$\ln(H) - \ln(H_0) = -\int_0^N \epsilon_{\rm acc}(N')dN'. \tag{5.6}$$

And using $k = aH$, the scale of the mode exiting the horizon at each e-fold N is

$$\ln k(N) - \ln k_0 = N - \int_0^N \epsilon_{\rm acc}(N')dN'. \tag{5.7}$$

To first order in slow-roll expansion [213], the primordial curvature and tensor spectra are

$$\Delta_{\rm s}^2 = \frac{k^3}{2\pi^2}\mathcal{P}_{\rm s}(N) = \mathcal{A}_{\rm s}\frac{H^2(N)}{H^2(N_{\rm p})}\frac{\epsilon_{\rm acc}(N_{\rm p})}{\epsilon_{\rm acc}(N)} \tag{5.8}$$

and

$$\Delta_{\rm t}^2 = \frac{k^3}{2\pi^2}\mathcal{P}_{\rm t}(N) = 16\mathcal{A}_{\rm s}\epsilon_{\rm acc}(N_{\rm p})\frac{H^2(N)}{H^2(N_{\rm p})}, \tag{5.9}$$

where $N_{\rm p}$ is the e-fold at which the mode corresponding to Fourier wavenumber k exits the horizon and $\mathcal{A}_{\rm s}$ is the primordial normalisation of the perturbations at the scale $k_{\rm p}$.

The tensor to scalar ratio is calculated as

$$r(N) \equiv \frac{\Delta_{\rm t}^2}{\Delta_{\rm s}^2} = 16\epsilon_{\rm acc}(N). \tag{5.10}$$

The Lyth bound comes from combining the latter Eq. (5.10) with Eq. (5.5); plus assuming $\epsilon_{\rm acc}$ and r have some lower bound for some range of e-folds. Finally, the scalar and tensor spectral index are defined as

$$n_{\rm s} \equiv 1 + \frac{d\ln\Delta_{\rm s}^2}{d\ln k} = 1 - 4\epsilon_{\rm acc} + 2\eta_{\rm acc}, \tag{5.11}$$

$$n_{\rm t} \equiv \frac{d\ln\Delta_{\rm t}^2}{d\ln k} = -2\epsilon_{\rm acc}, \tag{5.12}$$

$$\eta_{\rm acc} = \epsilon_{\rm acc} + \frac{1}{2}\frac{d\ln\epsilon_{\rm acc}}{dN}, \tag{5.13}$$

where the notation is taken as in Ref. [61]. These parameters complete the model independent analysis that aims to find a minimum constraint in $\Delta\phi$ given a bound in r. For small $\epsilon_{\rm acc}$, Eq. (5.11) can be approximated as

$$n_{\rm s} \approx 1 + \frac{d\ln\epsilon_{\rm acc}}{dN}. \tag{5.14}$$

Equation (5.14) can in turn be used to relate $\epsilon_{\rm acc}$ values separated by a certain range of e-foldings,

$$\ln \epsilon_{\rm acc}^{\rm i+1} \approx \ln \epsilon_{\rm acc}^{\rm i} + \Delta N(n_{\rm s} - 1). \tag{5.15}$$

The latter approximation is an important point of reference to develop the numerical analysis to sample the inflationary trajectories later on.

5.3 The acceleration sampling

Instead of varying the usual primordial parameters $n_{\rm s}$, r, $n_{\rm t}$, $n_{\rm s}'$ and so on, the method implemented here utilises a functional space $\epsilon_{\rm acc}(N)$ as the core of the MCMC exploration of the parameter space. This is sampled using random amplitudes in $\ln \epsilon_{\rm i}$ at equally spaced e-folds $N_{\rm i}$ which are then splined over using Fortran's cubic spline and splint routines.

A logarithmic definition of the parameters is favoured as a way of guaranteeing that all points of the trajectory will be positive after the splining result is converted to linear scale. Because at some stages the spline routine needs to interpolate between rapidly oscillating points, in linear scale this can lead to inconsistencies in the algorithm, and getting a less accurate calculation as a result. This piece of code was implemented with contributions from all five collaborators.

Reference [61] implemented this method and tested the Monte Carlo exploration with different numbers of $\ln \epsilon_{\rm i}$ parameters ranging from 4 to 7. Whilst the case with four ϵ's did not converge due to under sampling of the boundary point at low e-folds N, it was found that the model with 5 amplitudes worked the best, as it achieved a description of the data with minimum information.

Version six worked similarly to number five; number seven was disfavoured because of having too many parameters to reproduce the inflationary trajectory, causing an oversampling of the interpolation method which relies on so much complex structure that it was disfavoured by the data. Hence, for this project it was decided to attempt the parametrisation using five amplitudes $\ln \epsilon_{\rm i}$. All the results were first carefully performed with two splines, comparable to a slow-roll model. These were in excellent agreement to the power-law case.

As usual, the main parts of the implementation occur in CAMB. The spline point amplitudes $\ln \epsilon_{\rm i}$ were positioned evenly between e-folds $0 < N < 14$. It is worth noting that in here, $N = 0$ does not corresponds to the beginning of inflation, but to the time when the current horizon left the horizon during inflation.

This range was chosen to match the largest wavelength k required by CAMB to the largest value of $\epsilon_{\rm acc}$ allowed by the prior distribution. As seen in Eq. (5.7), the mode k that corresponds to every e-fold N is dependent on the integration of the acceleration trajectory. The range of the CMB power spectrum observations is $2 \leq l \leq 2500$ corresponding to $\mathcal{O}(10^{-5}) \leq k \leq \mathcal{O}(10^{-1})$, which is smaller than the span of the scales computed by the software, $\mathcal{O}(10^{-6}) \leq k \leq \mathcal{O}(10^{0})$, where k is in units of Mpc^{-1}.

However, CAMB needs this range to compute the radiation transfer functions accurately. This means the spacing used is not the most logical choice with respect to the data, but it avoids extrapolating the functions beyond the splining region. Figure 5.1 illustrates the (k,N) relationship for the best-fit model of the posterior distribution analysis.

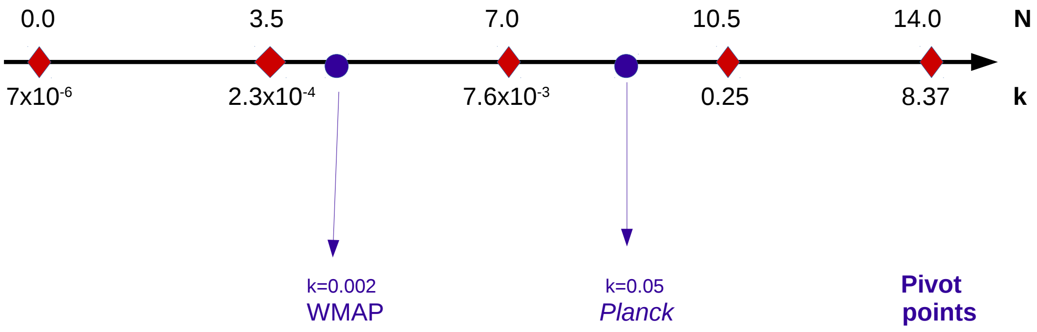

Figure 5.1 *One-to-one correspondence between the wavenumber k required by* CAMB *and the e-fold N where each of the amplitudes $\ln\epsilon_{\rm i}$ is positioned for the best-fit model found in the MCMC sampling presented in Section 5.4. The approximate positions of the multipoles plus the pivot scales for Planck and WMAP are also labelled.*

The parametrisation was chosen considering the constraining range of the CMB data. At first, the analysis was performed giving each of the five $\epsilon_{\rm acc}$ amplitudes the same prior. However, because of the high correlation that exists between adjacent points, the sampling was extremely inefficient, as the allowed models lie in a narrow linear curve that every jump of the MCMC exploration would have a hard time to emulate.

Instead, it was decided to allow a wide range of variation of ϵ_3 and make the rest of the amplitudes dependent on this parameter whilst still allowing them to vary using a shift $\delta_{\rm i}$. This means the MCMC search is performed from parameter definitions

$$\begin{aligned}
\delta_1 &= \ln\epsilon_1 - \ln\epsilon_3 \qquad (5.16)\\
\delta_2 &= \ln\epsilon_2 - \ln\epsilon_3\\
\delta_4 &= \ln\epsilon_4 - \ln\epsilon_3\\
\delta_5 &= \ln\epsilon_5 - \ln\epsilon_3
\end{aligned}$$

Table 5.1 lists the prior distributions. These were chosen centred in the value predicted by Eq. (5.15) by considering a likely $n_{\rm s}$ and the e-fold separation ΔN. However, after COSMOMC chooses to try a selected set of parameters, before these are sent to compute the scalar and tensor power spectrum, they are re-defined as

$$\begin{aligned}
\ln\epsilon_1 &= \delta_1 + \ln\epsilon_3 \qquad (5.17)\\
\ln\epsilon_2 &= \delta_2 + \ln\epsilon_3\\
\ln\epsilon_4 &= \delta_4 + \ln\epsilon_3\\
\ln\epsilon_5 &= \delta_5 + \ln\epsilon_3
\end{aligned}$$

These are then sent to CAMB to perform the $\mathcal{C}_l$ predictions. Most of the information is contained in:

- **equations.f90:** This file receives the $\ln\epsilon_{\rm i}$ values from COSMOMC and uses them to build a table containing all the information needed for the calculation of the initial scalar and tensor power spectrum. First, the full function $\ln\epsilon(N)$ is constructed using a cubic spline. This is the most efficient manner to proceed because this calculation can later be used to compute the rest of the equations without needing to spline anything else. Afterwards, Eq. (5.7) is integrated in order to obtain a relationship between the e-folds N and the wavenumber k. The table is completed by calculating

Parameter	Prior range
δ_1	[-0.5, 0.5]
δ_2	[-0.3, 0.3]
ϵ_3	[-10, -3]
δ_4	[-0.3, 0.3]
δ_5	[-0.5, 0.5]
$\Omega_{\mathrm{b}}h^2$	[0.005, 0.1]
$\Omega_{\mathrm{c}}h^2$	[0.001, 0.99]
τ	[0.01, 0.8]
$100\theta_{\mathrm{MC}}$	[0.5, 10]
$\ln(10^{10}A_{\mathrm{s}})$	[2, 4]
$n_{\mathrm{s,k=0.05}}$	$\cdots$
$n_{\mathrm{s,k=0.05}}$	$\cdots$
$r_{\mathrm{k=0.002}}$	$\cdots$
$n_{\mathrm{t,k=0.05}}$	$\cdots$

Table 5.1: Prior ranges for amplitudes $\ln \epsilon_{\mathrm{i}}$ and baseline parameters. The meaning of the cosmological parameters is as in the *Planck* collaboration papers [8, 11]. The final four parameters listed are derived from the others.

Eqs. (5.6)-(5.9). Finally, the tensor-to-scalar ratio r, the spectral index n_{s} and the tensor spectral index n_{t} are calculated at the pivot scale $k = 0.002$ or $k = 0.05$ Mpc^{-1} by using Eqs. (5.10)-(5.12). This procedure is performed once for every choice of parameters tested by COSMOMC.

- **power tilt.f90:** The table calculated in equations.f90 is utilised by this file. The functions ScalarPower and TensorPower usually calculate the initial scalar power spectrum and tensor power spectrum, respectively with a power law, by receiving the amplitude $\mathcal{A}_{\mathrm{s}}$ and wavenumber k from COSMOMC. In this case, instead of the power law, the wavenumber k received by CAMB is positioned in the table and the $\mathcal{P}_{\mathrm{s}}$ and $\mathcal{P}_{\mathrm{t}}$ are obtained by interpolating between the two closest nearby points.

The calculations later proceed as usual and the MCMC is continued until a R-1 convergence statistic [17] of order 10^{-2} has been reached. From comparing the left and right hand sides of Fig 5.2 it can be observed that a considerable number of trajectories are eliminated by the data combination on the upper end of the prior, however the best-fit case (red points) is made of very small ϵ values. The figure on the left was made of 100 ϵ trajectories taken from random prior values, whereas the values for the plot on the right were evenly chosen from the posterior distribution using the same burn-in of 0.5, as in the rest of the results.

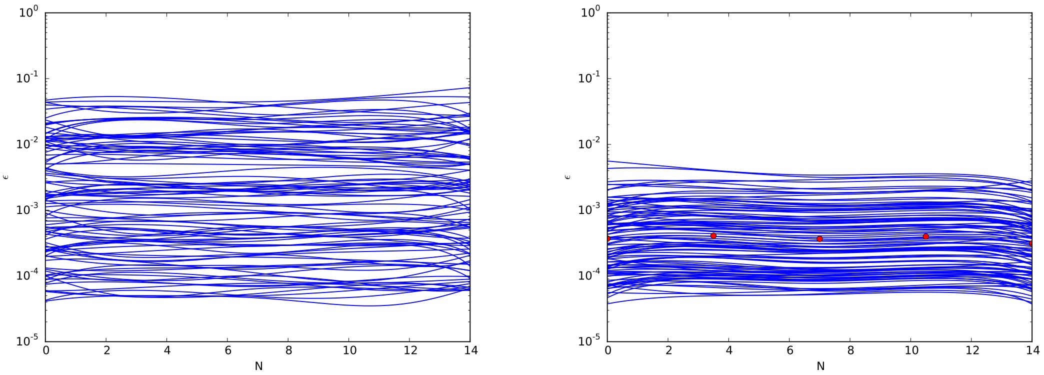

Figure 5.2 *Density plots for a random sample of the prior distribution of $(\delta_1, \delta_2, \epsilon_3, \delta_4, \delta_5)$ on the left. Similar plot with chosen values of the posterior distribution on the right. The best fit* $\ln \epsilon_i = (-7.90, -7.80, -7.91, -7.82, -8.07)$ *are depicted in red points.*

5.4 Cosmological Constraints

In this section, the data combination and probability distributions obtained from the MCMC exploration previously described are introduced. The results of this segment were obtained by myself, however I received generous feedback and advice from all members of the project. The descriptions of the results are heavily based on the insight from Hotchkiss, Byrnes and Liddle.

5.4.1 Datasets

Planck likelihood

The Planck best-fit CMB temperature power spectrum provides the main constraints in this project. Two files were used: TT, which covers the wide range multipoles $l = 2 - 2508$ and TEB, which allows for the computation of the CMB joint TT,EE, BB and TE likelihood in the range $l = 2 - 29$ [8, 10].

BAO data

Baryon acoustic oscillations (BAO) are the counterpart in the late time matter power spectrum of the acoustic oscillations seen in the CMB multipole spectrum [74]. Here the combination of 6dFGRS data [30] and the SDSS-MGS data [185] were used.

5.4.2 Acceleration trajectories

We start by looking at the 1-D marginalised posterior distributions for the baseline parameters and the derived ones depicted in Fig. 5.3. All the cosmological parameters are in good agreement with ΛCDM. Notice that the spectral index has been calculated at two scales: $k = 0.002$, corresponding to WMAP's pivot point [214]; and $k = 0.05$, which is *Planck*'s choice [8]. Whilst the latter is centered in $n_{\mathrm{s}(k=0.05)} \sim 0.96$, in agreement with the usual constraint, it can be observed that $n_{\mathrm{s}(k=0.002)} > 1.0$ for most of the probability.

Comparing this observation to the bound found by WMAP when the running $n_{\mathrm{s}'}$ is allowed to vary, it was shown that for non power law behavior the best fit of the spectral index lies above 1. However, in Planck's pivot scale case, for both power law and non power law, the constraint stays centered at 0.96. This is a subtle difference that our parametrisation is able to reproduce.

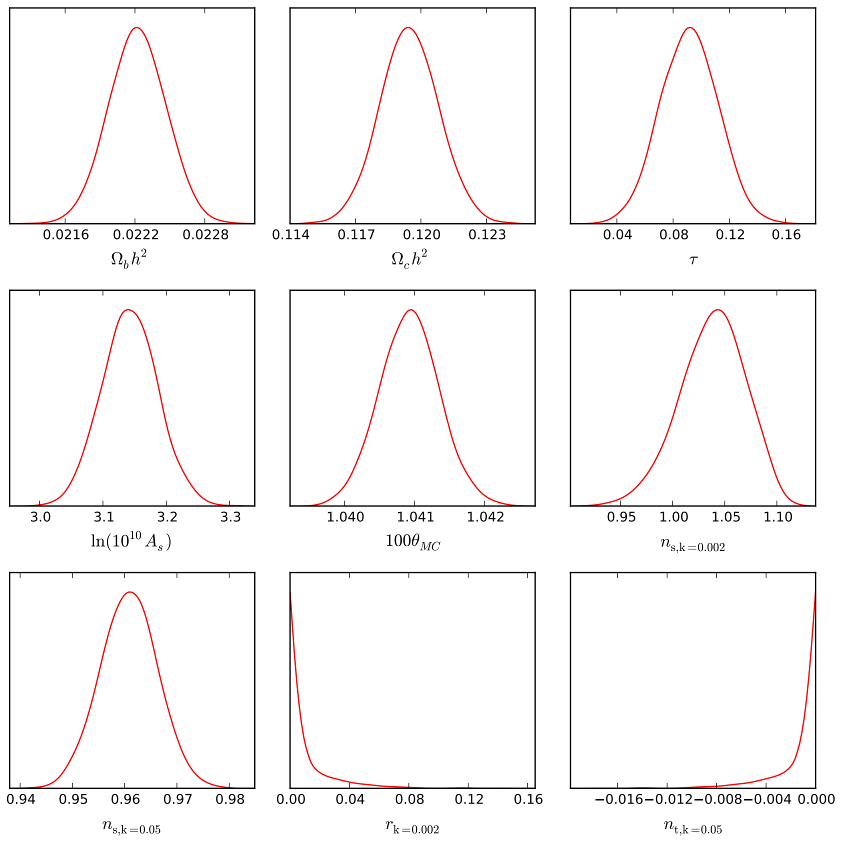

Figure 5.3 *1D marginalised posterior distributions for the baseline cosmological and derived parameters with priors given in Table 5.1 for data combination Planck + BAO.*

The causes for the n_{s} behaviour become more apparent in the triangular Fig. 5.4. Because of its positioning at the largest scale, δ_1 appears unbounded by the data. The centered value for δ_4, when re-defined to ϵ_4 is larger than ϵ_3. This means the power spectrum is blue shifted near $N \sim 7$, which corresponds to $k \sim 10^{-3}$ and goes back to be red tilted shortly afterwards; in accordance to $n_{\mathrm{s}(k=0.002)} \geq 1$ and $n_{\mathrm{s}(k=0.05)} \sim 0.96$.

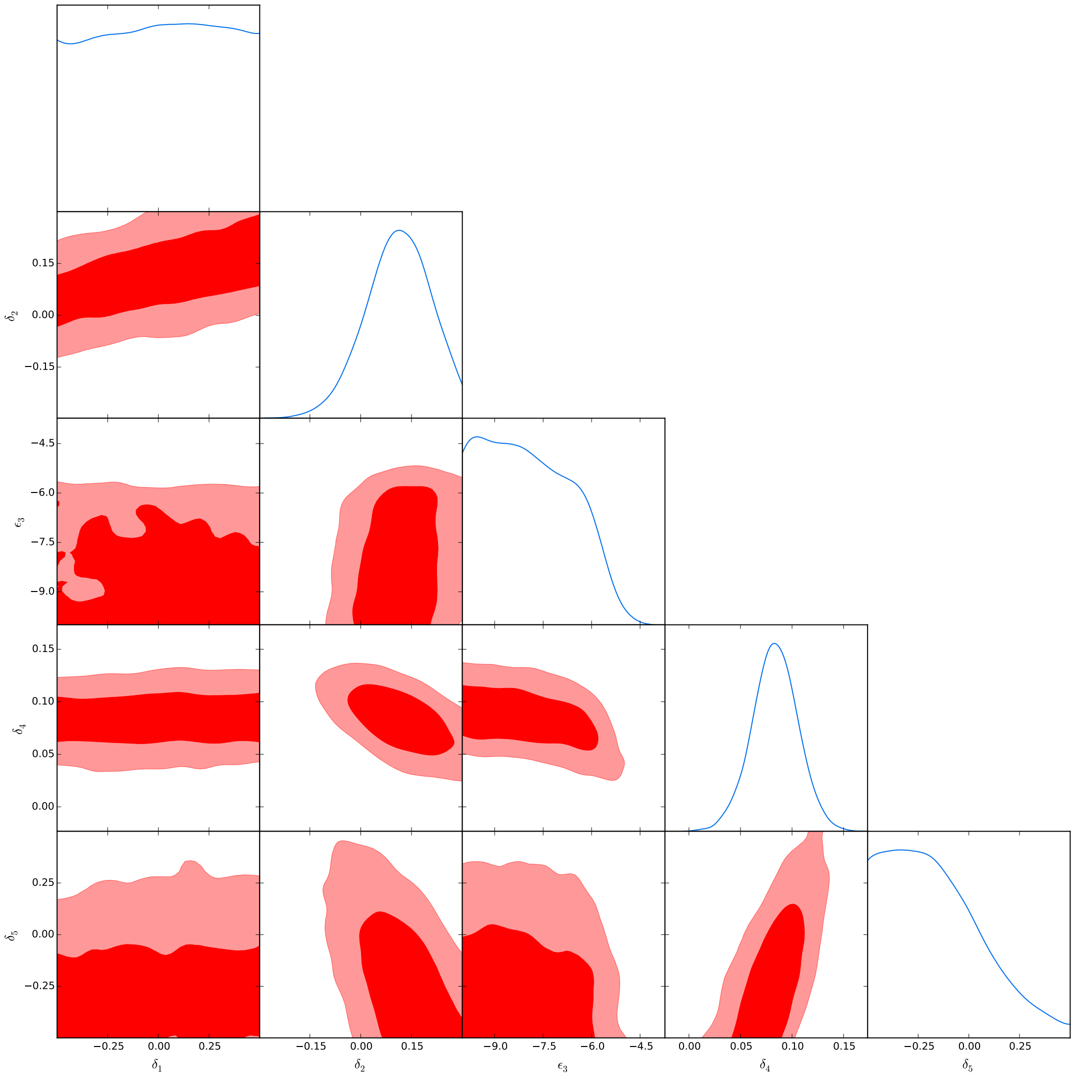

Figure 5.4 *The 68% and 95% 2D confidence contours depicting the* $(\delta_1, \delta_2, \epsilon_3, \delta_4, \delta_5)$ *parameter definitions analysed directly from the* GETDIST *software chains.*

The last parameter δ_5 slightly prefers smaller values, although it lies very far away from the CMB multipole span and is therefore largely unconstrained, which means not very meaningful conclusions can be obtained from it. The height in the constraint power is appreciated in the $(\delta_2, \epsilon_3, \delta_4)$ region. It can be observed that the data do not discriminate from the prior at the upper end of δ_2 which encourages a widening of the values allowed for this parameter for the next stage of the results.

Re-defining the parametrisation as in Eq. (5.17), Fig. 5.5 depicts the correlations between spline point amplitudes for the ϵ run. This is a schematic representation that should be observed with caution. In reality the contours of this figure are much narrower than they appear, but the smoothing features of the GETDIST program make them look wider than they are. However, the strength of the data in comparison to other regions can be observed in the (δ_2, δ_4) duplet, which is thinner than the rest of the contours.

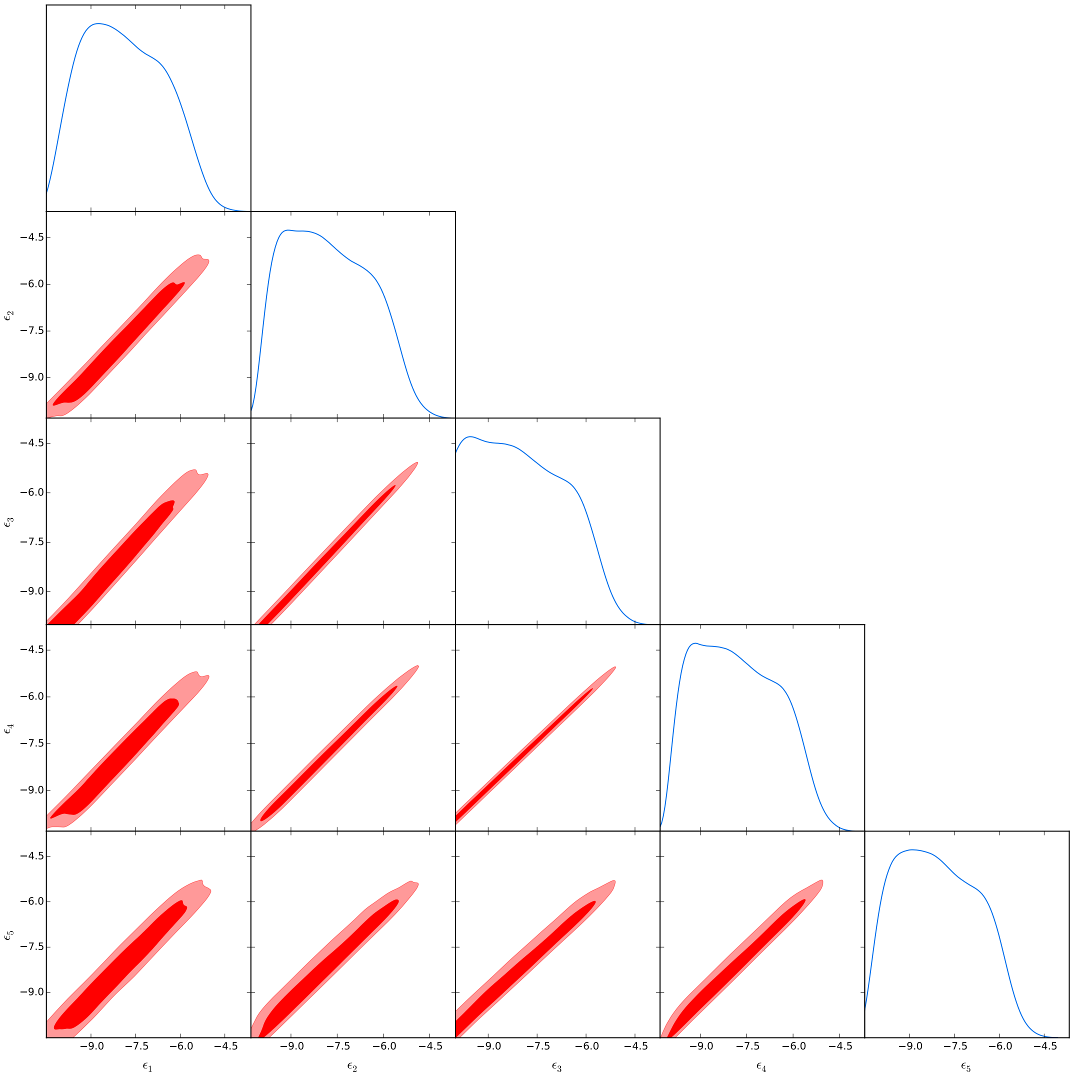

Figure 5.5 *The 2D contours of the splined points* $\ln \epsilon_\mathrm{i}$ *as re-defined by Eqs. (5.17) taken from the original values in Fig. 5.4.*

5.4.3 The rolling of the scalar field $\Delta\phi$

With the chains resulting from the MCMC analysis described in the previous sections it is now possible to determine the rolling of the scalar field during the acceleration trajectory. This is performed by calculating Eq. (5.5) for each of the chain elements produced by the MCMC search and evaluating the resulting column as a new derived parameter. This result is depicted in Figure 5.6. It can be observed that the shape of the posterior distribution mimics a quadratic type of behavior, in accordance with the expectation from the Lyth bound, Eq. (5.1), applied for $\Delta N = 14$ rather than 50.

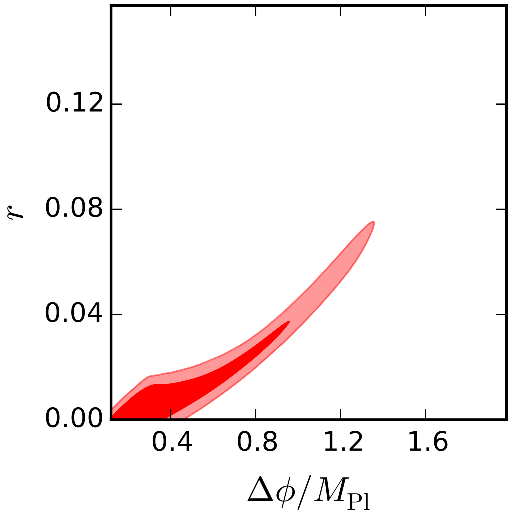

Figure 5.6 *The 68% and 95% confidence contour for the tensor-to-scalar ratio* r *and the rolling of the scalar field* $\Delta\phi$ *for the same models as in Fig. 5.4.*

In general, such an assumption is not valid (the usual Lyth bound assumes that epsilon is monotonically increasing towards the end of inflation), but it is acceptable in our circumstances because we are interested in the lower bound of r and the values of $\epsilon_{\rm acc}$ are being forced towards a dramatically small number (which we show is observationally allowed). Hence even if we were considering the ΔN=50 case the measurement of $\Delta\phi$ would not change significantly. Moreover, this analysis allows one to make a schematic measurement of the relationship between the rolling of the field $\Delta\phi$ and the tensor-to-scalar ratio by separating r into eight compartments to give a histogram for each of the ranges of r, between the smallest found of 7.06×10^{-4} to the largest 0.1565 as seen in Fig. 5.7.

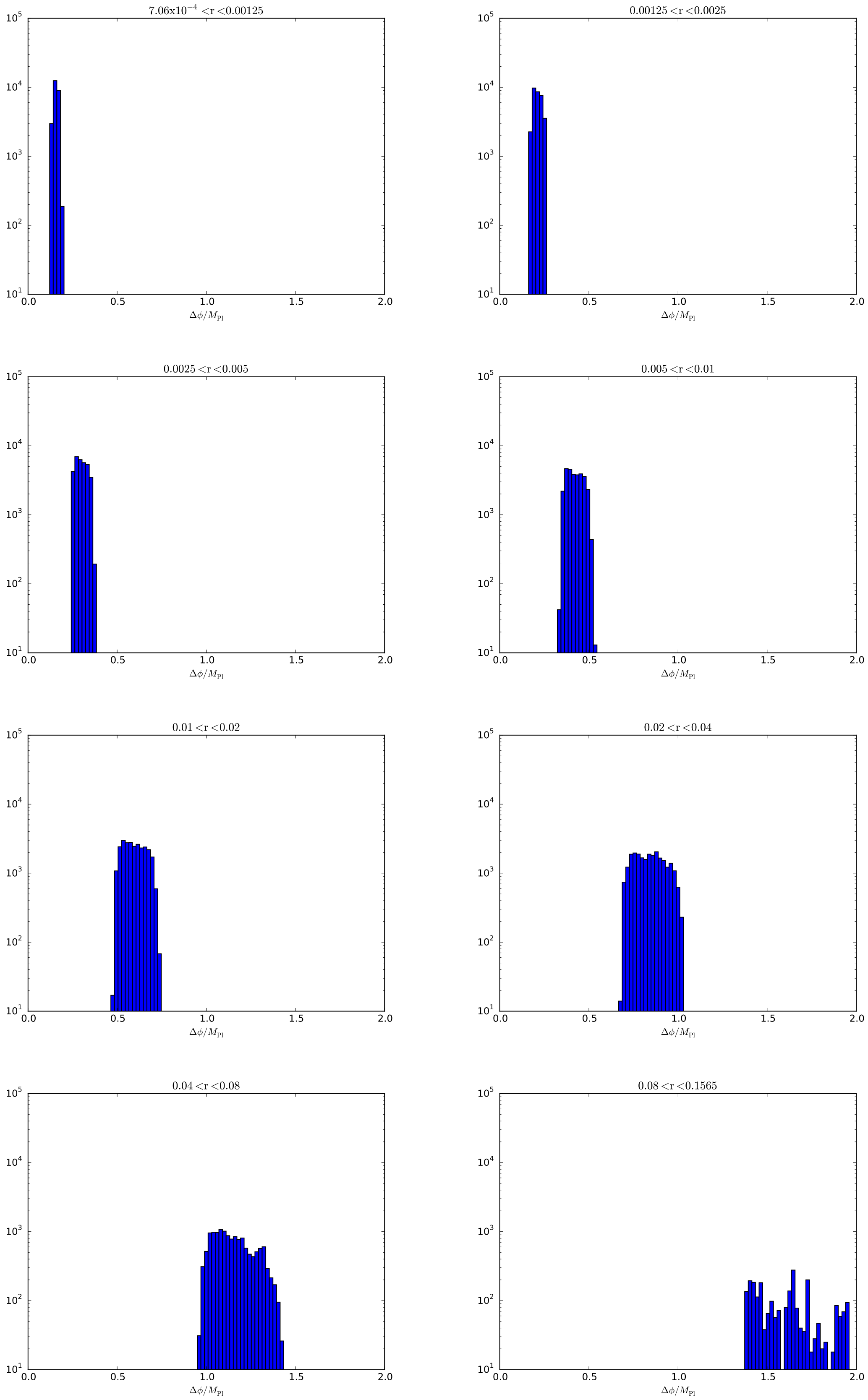

Figure 5.7 *Histogram representation of the relationship between the tensor-to-scalar ratio* r *and the rolling of the scalar field* $\Delta\phi$ *from the smallest to the largest values obtained in the posterior distribution.*

The histograms take into consideration the sample weight, or number of iterations staying at a certain parameter array values for each chain element. With our logarithmic prior, 99% of the samples lie below $r < 0.11$, which is *Planck's* constraint at 95% [8]. This discrepancy is expected because of the different prior used (*Planck's* is linear).

5.5 Discussion

The models are more copious in the first histogram of Fig. 5.7, corresponding to ($7.06 \times 10^{-4} < r < 0.00125$). This is relevant because studies of the limit on the detectability of the energy scale of inflation have demonstrated that, for a detector of sensitivity s uniformly observing the entire sky for time t [121]

$$r_{\text{lim}} = 10^{-2} \left(\frac{s}{\mu K \sqrt{\text{sec}}} \right)^2 \left(\frac{t}{1\,\text{year}} \right)^{-1} . \tag{5.18}$$

However, Eq. (5.18) [116] does not consider certain contamination effects from the lensing of the E mode [227]. Taking those into account, the detectability limit is set at $r_{\text{lim}} = 6 \times 10^{-4}$ [121, 135]. Stage 3 of the Dark Energy Task Force (DETF) [13] CMB experiments commencing in 2017 will already improve the constraint given by *Planck* to $r \leq 0.01$; and by 2021 the 500,000 detectors of CMB-S4 will reach $r \leq 0.001$ [1].

The histogram scheme predicts that for a 5 point spline representation, the rolling of the scalar field $\Delta\phi$ has to be of the order predicted by the Lyth bound. Figure. 5.8 presents the smallest $\Delta\phi$ for each of the eight histograms. The blue line corresponds to the prediction of Eq. (5.1) for 14 e-folds,

$$r \sim 0.0408 \left(\frac{\Delta\phi}{M_{\text{Pl}}} \right)^2 . \tag{5.19}$$

The closeness between Lyth's prediction and the minimum $\Delta\phi$ displacements found by the MCMC exploration is evident. This is an important finding as it shows that the data favour a value of $\Delta\phi$ that corresponds to Eq. (5.1). However, this result does not only assume that five points are sufficient to describe the acceleration trajectory, but its also due to the limited impact of the priors, which significantly restrict the increase of ϵ_{acc}.

Widening the priors would permit us to draw comparisons with the numerous

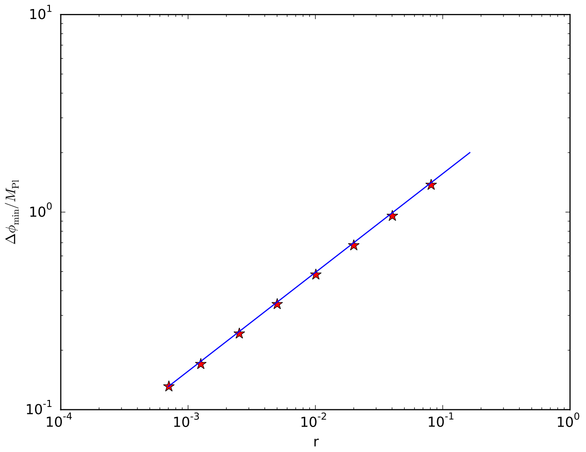

Figure 5.8 *The minimum (r,$\Delta\phi$) for each of the 8 bins described in Fig. 5.7. The blue line is the Lyth bound prediction Eq. (5.5). This is the chapter's main result.*

papers [26, 58, 168, 182, 197] published post-BICEP2 presenting a model able to achieve a substantially smaller $\Delta\phi$ than the one predicted by Lyth's postulate. Nonetheless, the latter could not be needed for cases where the proposed framework gives a $\delta\phi$ over 50 e-folds that is smaller than the lower bound found from just 14, because the integrand is always positive.

Moreover, a finer version of Figs. 5.7 and 5.8 can be used for reference when new datasets provide a tighter constraint on r, hence influencing future model selection.

5.6 Conclusions

This chapter introduced a question about the plausibility of publications that present an inflationary model able to avoid quantum corrections and alleviate the Lyth bound. Nonetheless, the studies that argue this restrict their measurements to *Planck's* pivot points.

In order to prove whether or not their results were appropriate, it is necessary first to investigate the behaviour the full CMB power spectrum data permit for the acceleration trajectory during inflation. A mechanism to explore this was implemented in COSMOMC where a MCMC search was performed based on 5 $\ln\epsilon_{\rm acc}$ parameters. The posterior distributions of the free parameters in this slow-roll approximation were analysed. Then, the study was extended to include a calculation of the rolling of the scalar field $\Delta\phi$ for each of the allowed chain elements.

This allowed us to visualise the array of values of $\Delta\phi$ that are possible for a certain range of r. The minimum $\Delta\phi$ found on each histogram is the main result of this chapter, and it has the potential to be a helpful point of reference in the future when more powerful surveys achieve a tighter constraint on the tensor-to-scalar ratio r. However, it must be noted that the analysis here considered an observable range that allows very small variation between the $\ln\epsilon$ amplitudes.

The reproduction of the Lyth bound by the chains shows the results are correct for the restricted δ range, and it will be very exciting to run with increased priors on $\delta_{1,2,4,5}$. Then it will be possible to make more robust statements on the absolute minimum $\Delta\phi$ allowed.

Another step to add strength to this study would consist of adding more $\ln\epsilon$ amplitudes. This would allow us to measure the maximum deviations the data permit on the power spectrum more accurately, hence answering one of the original questions of the project: for how many e-folds is ϵ_{acc} increasing?

In this sense, one helpful factor will be the addition of primordial black hole (PBH) [50] and ultra compact mini halo (UCMH) [40] constraints, which affect the smaller scales and provide upper bounds on the power spectrum of order 10^{-2}. Nonetheless this effect is quite restrictive and would seriously affect $\Delta\phi$, so it would be most convenient to draw a comparison both with its inclusion and without it.

Chapter 6

Conclusions

During the history of the Cosmos there are two distinguishable periods in which gravity acts in a repulsive manner. The first one occurs very early on, before the radiation domination epoch and is named inflation. This paradigm solves the flatness and horizon problems mentioned in Section 1.2 and generates density perturbations that became the seeds for the anisotropies in the primordial radiation and the inhomogeneous distribution of galaxies on large scales. Close observation of the CMB temperature and polarisation fluctuations provide information about cosmic inflation.

Some 10 billion years later, the Universe is again undergoing an accelerated expansion induced by dark energy, the component of mysterious origin that dominates the Cosmos at present. Theories that deviate from ΛCDM by means of proposing new matter sources or modifications to gravity are regularly being put forward to try to explain this phenomenon using the latest observations available. Moreover, numerous international collaborations continue to take place with the aim of achieving ever more complete sky explorations that will give further information about the dynamics of cosmic expansion.

Right now, 13.8 billion years after inflation (if ΛCDM is correct), this thesis explores the cosmological consequences of: a model described by a quintessence scalar field as an alternative to dark energy; the background and perturbative implications of a hybrid $f(\mathcal{R})$ modified theory of gravity; and the acceleration history under slow roll assumptions during inflation. With the use of MCMC techniques it was possible to place estimates on the range of parameters of these models. In turn, this information was used to answer important questions about the viability of these theories to describe the Universe and their contribution to the discussion of the problems faced by the standard model of cosmology.

Thawing quintessence was studied first. This family of theories offers a slightly more natural alternative to Λ [193] in the sense that it provides a trajectory of the energy density different from a constant, alleviating the cosmic coincidence issue mentioned in Section 1.2.4.

In addition, the thawing cases are preferred over the tracking type given that the latter arguably require a sharp change in the curvature of the potential at present. This effect worsens the cosmic coincidence issue, as it not only has to explain the similarity between the energy densities ρ_{DM} and ρ_{DE} but also why the field is entering such a special region of the potential at the same time [33].

In Chapter 2 the pseudo-Nambu-Goldstone-Boson (PNGB) potential, which is of cosine shape and thawing nature, was utilised to describe a scalar field that substitutes the cosmological constant Λ as the source of dark energy. This corresponds to a scenario where the equation of state w_{DE} is always ≥ -1.

The *Planck* CMB anisotropy temperatures along with BAO and Supernovae observations were used to improve the existing constraints on the amplitude M^4, the initial field slope ϕ_{i}/f and the width f/M_{Pl} of the PNGB potential, as well as the baseline cosmological parameters. The constraints reproduce the ΛCDM case at the edge of the posterior distribution. Furthermore, the present equation of state for this framework was restricted to be $w_0 < -0.88$ for 95% of the models.

Comparing these results to the semi-analytical equation of state for thawing quintessence [55], the application of the PNGB potential achieves much tighter bounds on the curvature parameter K as described in Eq. (2.38). After examining different dataset combinations and parameter choices from f/M_{Pl} to $1/f$, it was observed that the data are tightly linked to the choice of parametrisation. The quintessence code used to obtain these results could be extended to include k-essence models.

It is important to be aware of the constraining power that future surveys will have on this model. According to the Dark Energy Task Force (DETF) report [13], the most stringent constraints on DE are placed by the observational techniques Baryon Acoustic Oscillations (BAO), Galaxy Cluster (CL), Weak Lensing (WL) and Supernovae (SN), of which the latter is the most important. The Dark Energy Survey (DES), which started observing in 2013 and will continue until 2018, uses the latest technologies that increase the accuracy of these four probes [179].

When Stage 4 of the DETF methodology is achieved, it is possible that several quintessence models will be eliminated [23]. In fact, Abrahamse et al. [4] published a forecast study of PNGB quintessence for Stages 2 to 4 of the DETF; when the predicted Stage 4 data arrive, this debate will be revived

Moving on from modifications of matter to explain cosmic acceleration, the next two chapters of this thesis focused on the theory of hybrid-metric Palatini gravity. The phenomenology of $f(R)$ gravity has been extensively studied in order to attain cosmic acceleration. Both the metric and Palatini versions have been considered; however, the two manifest severe downsides.

Moreover, hybrid $f(R)$ avoids many of the drawbacks of its precursor models and most possibly, does not need to invoke a screening mechanism. Nonetheless, this has not been considered in depth yet and hence is worth noting as a possible further area of development. The theoretical strength of this theory, and its novelty make it a very interesting investigative prospect.

Authors Capozziello, Harko, Koivisto, Lobo and Olmo provided a complete description of the cosmological formalism of this theory. Chapter 3 of this thesis builds on their work to study two specific models of hybrid-metric Palatini gravity characterised by a quadratic and exponential function $f(\mathcal{R})$ that modifies the standard Einstein-Hilbert action 1.16.

Their background history is predicted, showing that it does not deviate much from ΛCDM. However, this is because the deviation from the gravitational constant G in the high-redshift regime is set to be small. Later on, the models' free parameters are constrained applying a Metropolis-Hastings MCMC algorithm using background observables only: the shift parameter of the CMB, baryon acoustic oscillations and the supernovae luminosity-redshift function.

The Starobinsky case is in close proximity to Λ. For the exponential scenario a 10^{-2} limit on $f_R(z_\mathrm{i})$ was found, which marks the maximum possible deviation from the gravitational constant G at 1%, in accordance to early-time constraints on scalar-tensor theories of gravity from BBN and CMB [87, 219]. This demonstrates that $f_R(z_\mathrm{i})$ is an appropriate parametrisation for these theories.

Whilst studies of modified gravity have focused on the search for alternative explanations for the late-time accelerated expansion or on testing gravity at large scales [15, 111, 175, 183], early-time modifications have mostly been ignored [36, 146]. This means there is a lack of understanding of high-redshift MG effects on cosmic observables and the constraining power that current data have on them.

Chapter 4 uses a phenomenological model introduced in Ref. [138] to study early time modifications of gravity. This designer model has the same background evolution as ΛCDM, but inserts a decaying correction early on. This constitutes an advantage to probe modifications of gravity introduced after recombination and their effects on the CMB features.

The analysis was performed using the MGCAMB code. This software parametrises deviations from the linear perturbations using the function of time μ, that appears in the modified Poisson equation; and γ, that defines the ratio between the Newtonian potentials. Lima developed an analytic approximation to describe the evolution of the slip between the potentials to reproduce the oscillatory behaviour observed in the ratio between the gravitational potentials at early times [139].

It was observed that there is a strong correlation between the redshift at which the modifications are introduced and the bounds obtained. The higher the redshift, the stronger the constraints on the initial displacement of the scalar field will be. For instance, at redshift $z = 1000$, $f_R(z_{\rm i}) \approx 10^{-2}$. This constraint is linked to strong effects on the CMB power spectrum such as a shift in the Sachs-Wolfe plateau because of the modification of the Newtonian potential close to the recombination epoch.

Furthermore, the first peak is considerably suppressed, an effect caused by a variation of the gravitational potentials near the decoupling time that, joined to the radiation energy density of that age, adds on an early integrated Sachs-Wolfe effect that alters the amplitude and position of the CMB peaks. Forecasts of observations using 21 cm survey data and standard sirens were also investigated. The first will improve the present constraints considerably, while the latter will not be useful in this regard.

Even if hybrid $f(R)$ is a compelling theory to study, it is lacking in the same aspect as the rest of the MG models in the literature. That is, they are all plagued with additional problems to achieve self-acceleration or are in need of a cosmological constant or a potential playing the role of the former. Two routes can be followed here: either MG theories continue to be developed with the purpose of testing gravity at different scales or new models are created that can achieve self acceleration by their own modifications, without the need for extra sources.

Finally, chapter 5 focuses on constraining the parameters that describe the very early Universe. This study was motivated by the controversy surrounding the BICEP2 experiment, when a number of authors [26, 58, 168, 182, 197] put forward a model capable of both alleviating the Lyth bound and fitting the observations. However, we would argue that these investigations had been tested in an incomplete manner, as they only took into consideration the amplitude $\mathcal{A}_\mathrm{s}$ and the spectral index n_s at *Planck's* pivot scale, instead of analysing the behaviour of their model for the whole of the CMB power spectrum.

In Chapter 5, a slow-roll based parametrisation of the acceleration trajectory ϵ was explored with the aim of finding the rolling of the scalar field $\Delta\phi$ that an inflationary theory must reproduce in accordance with a specific value of the tensor-to-scalar ratio r. This was performed using *Planck's* cosmological data and baryonic acoustic oscillations. Several features of the inflationary paths were analysed and later, the posterior distributions were altered to obtain bounds on (Δ_ϕ,r), a histogram representation of inflaton values according to potential r measurements and the minimum displacement allowed for each of them.

It was found that the (Δ_ϕ,r) correspondence is in very good agreement with the Lyth bound, a reassuring fact that shows the methodology implemented in CAMB is working properly. In the near future, this study is to be extended to calculate the ϵ trajectories for at least 50-60 e-folds, which is the lower bound prediction for the duration of inflation. The behaviour of the acceleration history will also be extended by the inclusion of more amplitudes, hence allowing the measurement of changes more accurately.

This will enable the team to draw comparisons with the values of $(r, \Delta\phi)$ for models that claim to evade the Lyth bound and fit the observations. The addition of PBH [50] and UCMH [40] likelihoods could improve the precision of the power spectrum prediction.

Thanks to international projects such as the Dark Energy Survey (DES) [3], the extended Baryon Oscillation Spectroscopic Survey (eBOSS) [65] and Euclid [132], the knowledge of the cosmological structure will continue to be refined in the coming decades. This will enrich the research carried out in dark energy and inflation, helping to unravel complexities in the nature of the Universe.

The research on cosmological models included in this thesis has provided me with experience in the study of theory, data analysis and extraction of information about the viability of inflation, dark energy and modified gravity frameworks. However, the amount of gravity modifications one can come up with is large, and investigating one by one is an almost infinitely time consuming task.

Due to this, I am interested in constraining theories of gravity through general frameworks, in particular: Parametrised Post-Friedmann (PPF) [21], links between Parametrised Post-Newtonian (PPN) and cosmology [189], and Effective Field Theory (EFT) [25, 93]. For instance, the implementation of EFTCAMB [104] allows to test late-time acceleration in a model independent way that includes most DE/MG gravity models of cosmological interest.

In this regard, the analysis of theories where dark energy is coupled to dark matter is attractive too, given the ability of such models to alter the background evolution of the involved cosmological components, and possibly provide a natural solution for the coincidence problem.

On one side, a general parametrisation of dark energy models coupled to dark matter has been added to the PPF formalism [204]. On the other, this prescription for dark energy perturbations has already been implemented in CAMB [105]. It would be desirable to constrain scalar field theories coupled to dark matter by implementing the necessary free functions in the PPF code. This would be an important step towards a complete understanding of the capabilities of the aforementioned models, under the PPF formalism.

Bibliography

[1] Abazajian, K. N., et al. "CMB-S4 Science Book, First Edition.", arXiv e-prints (2016), arXiv: 1610.02743.

[2] Abbott, B. P., et al. "Observation of Gravitational Waves from a Binary Black Hole Merger." *Phys. Rev. Lett.* 116, 6: (2016) 061 102.

[3] Abbott, T., et al. "The dark energy survey.", arXiv e-prints (2005), arXiv: 0510346.

[4] Abrahamse, A., A. Albrecht, M. Barnard, and B. Bozek. "Exploring parameter constraints on quintessential dark energy: The pseudo-Nambu-Goldstone-boson model." *Phys. Rev.* D77: (2008) 103 503.

[5] Adam, R., et al. "Planck 2015 results. I. Overview of products and scientific results." *Astron. Astrophys.* 594: (2016) A1.

[6] Ade, P. A. R., et al. "Detection of B-Mode Polarization at Degree Angular Scales by BICEP2." *Phys. Rev. Lett.* 112, 24: (2014) 241 101.

[7] ———. "Planck 2013 results. XVI. Cosmological parameters." *A&A* 571: (2014) A16.

[8] ———. "Planck 2015 results. XIII. Cosmological parameters." *A&A* 594: (2016) A13.

[9] ———. "Planck 2015 results. XIV. Dark energy and modified gravity." *A&A* 594: (2016) A14.

[10] ———. "Planck 2015 results. XX. Constraints on inflation." *A&A*. 594: (2016) A20.

[11] Aghanim, N., et al. "Planck 2015 results. XI. CMB power spectra, likelihoods, and robustness of parameters." *A&A* 594: (2016) A11.

[12] Albrecht, A., and P. J. Steinhardt. "Cosmology for Grand Unified Theories with Radiatively Induced Symmetry Breaking." *Phys. Rev. Lett.* 48: (1982) 1220–1223.

[13] Albrecht, A., et al. "Report of the Dark Energy Task Force.", arXiv e-prints (2006), arXiv: 0609591.

[14] Alpher, R. A. “A Neutron-Capture Theory of the Formation and Relative Abundance of the Elements.” *Physical Review* 74: (1948) 1577–1589.

[15] Amanullah, R., et al. “Spectra and Light Curves of Six Type Ia Supernovae at $0.511 < z < 1.12$ and the Union2 Compilation.” *Astrophys. J.* 716: (2010) 712–738.

[16] Amendola, L., and S. Tsujikawa. *Dark Energy: Theory and Observations.* Cambridge University Press, Cambridge, U.K., 2010.

[17] An, L., S. Brooks, and A. Gelman. “Stephen Brooks and Andrew Gelman.” *Journal of Computational and Graphical Statistics* 7: (1998) 434–455.

[18] Anderson, L., et al. “The clustering of galaxies in the SDSS-III Baryon Oscillation Spectroscopic Survey: Baryon Acoustic Oscillations in the Data Release 9 Spectroscopic Galaxy Sample.” *MNRAS* 427, 4: (2013) 3435–3467.

[19] ———. “The clustering of galaxies in the SDSS-III Baryon Oscillation Spectroscopic Survey: baryon acoustic oscillations in the Data Releases 10 and 11 Galaxy samples.” *MNRAS* 441, 1: (2014) 24–62.

[20] Armendariz-Picon, C., V. F. Mukhanov, and P. J. Steinhardt. “Essentials of k essence.” *Phys. Rev.* D63: (2001) 103 510.

[21] Baker, T., P. G. Ferreira, and C. Skordis. “The Parameterized Post-Friedmann framework for theories of modified gravity: concepts, formalism and examples.” *Phys. Rev.* D87, 2: (2013) 024 015.

[22] Banks, T., M. Dine, P. J. Fox, and E. Gorbatov. “On the possibility of large axion decay constants.” *JCAP* 0306: (2003) 001.

[23] Barnard, M., A. Abrahamse, A. Albrecht, B. Bozek, and M. Yashar. “A measure of the impact of future dark energy experiments based on discriminating power among quintessence models.” *Phys. Rev.* D78: (2008) 043 528.

[24] Barreiro, T., E. J. Copeland, and N. J. Nunes. “Quintessence arising from exponential potentials.” *Phys. Rev.* D61: (2000) 127 301.

[25] Bellini, E., and I. Sawicki. “Maximal freedom at minimum cost: linear large-scale structure in general modifications of gravity.” *JCAP* 1407: (2014) 050.

[26] Ben-Dayan, I., and R. Brustein. “Cosmic Microwave Background Observables of Small Field Models of Inflation.” *JCAP* 1009: (2010) 007.

[27] Bennett, C. L., et al. “Nine-Year Wilkinson Microwave Anisotropy Probe (WMAP) Observations: Final Maps and Results.” *Astrophys. J. Suppl.* 208: (2013) 20.

[28] Bertotti, I. L. T. P., B. "A test of general relativity using radio links with the Cassini spacecraft." *Nature* 425: (2003) 425–374.

[29] Betoule, M., et al. "Improved cosmological constraints from a joint analysis of the SDSS-II and SNLS supernova samples." *Astron. Astrophys.* 568: (2014) A22.

[30] Beutler, F., et al. "The 6dF Galaxy Survey: Baryon Acoustic Oscillations and the Local Hubble Constant." *MNRAS* 416: (2011) 3017–3032.

[31] Blake, C. "Statistics notes." *Centre for Astrophysics and Computing, Swinburne University of Technology* `http://astronomy.swin.edu.au/~cblake/statsnotes.pdf`.

[32] Blei, D. M., M. I. Jordan, et al. "Variational inference for Dirichlet process mixtures." *Bayesian analysis* 1, 1: (2006) 121–143.

[33] Bludman, S. "Tracking quintessence would require two cosmic coincidences." *Phys. Rev. D.* 69, 12: 122002.

[34] Boubekeur, L., and D. Lyth. "Hilltop inflation." *JCAP* 0507: (2005) 010.

[35] Brans, C., and R. H. Dicke. "Mach's Principle and a Relativistic Theory of Gravitation." *Physical Review* 124: (1961) 925–935.

[36] Brax, P., C. van de Bruck, S. Clesse, A.-C. Davis, and G. Sculthorpe. "Early Modified Gravity: Implications for Cosmology." *Phys. Rev.* D89, 12: (2014) 123 507.

[37] Brax, P., C. van de Bruck, A.-C. Davis, and D. J. Shaw. "f(R) Gravity and Chameleon Theories." *Phys. Rev.* D78: (2008) 104,021.

[38] Brax, P., S. Clesse, and A.-C. Davis. "Signatures of Modified Gravity on the 21-cm Power Spectrum at Reionisation." *JCAP* 1301: (2013) 003.

[39] Brent, R. P. *Algorithms for Minimization without Derivatives.* Prentice-Hall, 1972.

[40] Bringmann, T., P. Scott, and Y. Akrami. "Improved constraints on the primordial power spectrum at small scales from ultracompact minihalos." *Phys. Rev.* D85: (2012) 125 027.

[41] Brooks, S., A. Gelman, G. Jones, and X.-L. Meng. *Handbook of Markov Chain Monte Carlo.* CRC press, 2011. `https://scholar.google.de/scholar.bib?q=info:A4xlUax02S0J:scholar.google.com/&output=citation&hl=de&ct=citation&cd=0`.

[42] Buchdahl, H. A. "Non-linear Lagrangians and cosmological theory." *MNRAS* 150: (1970) 1.

[43] Calabrese, E., et al. "CMB Lensing Constraints on Dark Energy and Modified Gravity Scenarios." *Phys. Rev.* D80: (2009) 103 516.

[44] Caldwell, R. R., R. Dave, and P. J. Steinhardt. “Cosmological Imprint of an Energy Component with General Equation of State.” *Phys. Rev. Lett.* 80: (1998) 1582–1585.

[45] Caldwell, R. R., and M. Kamionkowski. “The Physics of Cosmic Acceleration.” *Ann. Rev. Nucl. Part. Sci.* 59: (2009) 397–429.

[46] Capozziello, S., T. Harko, T. S. Koivisto, F. S. N. Lobo, and G. J. Olmo. “Cosmology of hybrid metric-Palatini f(X)-gravity.” *JCAP* 1304: (2013) 011.

[47] ———. “The virial theorem and the dark matter problem in hybrid metric-Palatini gravity.” *JCAP* 1307: (2013) 024.

[48] ———. “Hybrid metric-Palatini gravity.” *Universe* 1, 2: (2015) 199–238.

[49] Capozziello, S., T. Harko, F. S. N. Lobo, and G. J. Olmo. “Hybrid modified gravity unifying local tests, galactic dynamics and late-time cosmic acceleration.” *Int. J. Mod. Phys.* D22: (2013) 1342 006.

[50] Carr, B. J., K. Kohri, Y. Sendouda, and J. Yokoyama. “Constraints on primordial black holes from the Galactic gamma-ray background.” *Phys. Rev.* D94, 4: (2016) 044 029.

[51] Carroll, S. M. *Spacetime and geometry: An introduction to general relativity.* 2004. `http://www.slac.stanford.edu/spires/find/books/www?cl=QC6:C37:2004`.

[52] Charmousis, C., E. J. Copeland, A. Padilla, and P. M. Saffin. “General second order scalar-tensor theory, self tuning, and the Fab Four.” *Phys. Rev. Lett.* 108: (2012) 051 101.

[53] Chiba, T. “Slow-Roll Thawing Quintessence.” *Phys. Rev.* D79: (2009) 083 517.

[54] ———. “The Equation of State of Tracker Fields.” *Phys. Rev.* D81: (2010) 023 515.

[55] Chiba, T., A. De Felice, and S. Tsujikawa. “Observational constraints on quintessence: thawing, tracker, and scaling models.” *Phys. Rev.* D87, 8: (2013) 083 505.

[56] Chiba, T., T. Okabe, and M. Yamaguchi. “Kinetically driven quintessence.” *Phys. Rev.* D62: (2000) 023 511.

[57] Chiba, T., N. Sugiyama, and T. Nakamura. “Cosmology with x matter.” *MNRAS* 289: (1997) L5–L9.

[58] Civiletti, M., M. U. Rehman, Q. Shafi, and J. R. Wickman. “Red Spectral Tilt and Observable Gravity Waves in Shifted Hybrid Inflation.” *Phys. Rev.* D84: (2011) 103 505.

[59] Clemence, G. M. “The Relativity Effect in Planetary Motions.” *Rev. Mod. Phys.* 19: (1947) 361–364.

[60] Clifton, T., P. G. Ferreira, A. Padilla, and C. Skordis. “Modified Gravity and Cosmology.” *Phys. Rept.* 513: (2012) 1–189.

[61] Contaldi, C. R. “BICEP’s acceleration.” *JCAP* 1410, 10: (2014) 072.

[62] Copeland, E. J., A. R. Liddle, and D. Wands. “Exponential potentials and cosmological scaling solutions.” *Phys. Rev.* D57: (1998) 4686–4690.

[63] Copeland, E. J., M. Sami, and S. Tsujikawa. “Dynamics of dark energy.” *Int. J. Mod. Phys.* D15: (2006) 1753–1936.

[64] Cutler, C., and D. E. Holz. “Ultra-high precision cosmology from gravitational waves.” *Phys. Rev.* D80: (2009) 104 009.

[65] Dawson, K. S., et al. “The SDSS-IV extended Baryon Oscillation Spectroscopic Survey: Overview and Early Data.” *Astron. J.* 151: (2016) 44.

[66] De Felice, A., and S. Tsujikawa. “f(R) theories.” *Living Rev. Rel.* 13: (2010) 3.

[67] Deffayet, C., S. Deser, and G. Esposito-Farese. “Generalized Galileons: All scalar models whose curved background extensions maintain second-order field equations and stress-tensors.” *Phys. Rev.* D80: (2009) 064 015.

[68] Diez-Tejedor, A., and D. J. E. Marsh. “Cosmological production of ultralight dark matter axions.” .

[69] Dimastrogiovanni, E., L. M. Krauss, and J. Chluba. “Constraints on Gravitino Decay and the Scale of Inflation using CMB spectral distortions.” *Phys. Rev.* D94, 2: (2016) 023.

[70] Dine, M. “Dark matter and dark energy: a physicist’s perspective.” *This page intentionally left blank* 183.

[71] Dodelson, S. *Modern Cosmology.* Academic Press, 2003.

[72] Dutta, K., and L. Sorbo. “Confronting pNGB quintessence with data.” *Phys. Rev.* D75: (2007) 063 514.

[73] Dutta, S., and R. J. Scherrer. “Hilltop Quintessence.” *Phys. Rev.* D78: (2008) 123 525.

[74] Eisenstein, D. J., et al. “Detection of the baryon acoustic peak in the large-scale correlation function of SDSS luminous red galaxies.” *Astrophys. J.* 633: (2005) 560–574.

[75] Elizalde, E., S. Nojiri, and S. D. Odintsov. "Late-time cosmology in (phantom) scalar-tensor theory: Dark energy and the cosmic speed-up." *Phys. Rev.* D70: (2004) 043 539.

[76] Feroz, F., and M. Hobson. "Multimodal nested sampling: an efficient and robust alternative to Markov Chain Monte Carlo methods for astronomical data analyses." *Monthly Notices of the Royal Astronomical Society* 384, 2: (2008) 449–463.

[77] Ferreira, P. G., and M. Joyce. "Structure Formation with a Self-Tuning Scalar Field." *Phys. Rev. Lett.* 79: (1997) 4740–4743.

[78] Ferreira, P. G., and M. Joyce. "Cosmology with a primordial scaling field." *Phys. Rev.* D58: (1998) 023,503.

[79] Flanagan, E. E. "The Conformal frame freedom in theories of gravitation." *Class. Quant. Grav.* 21: (2004) 3817.

[80] Ford, L. H. "Cosmological-constant damping by unstable scalar fields." *Phys. Rev. D* 35: (1987) 2339–2344.

[81] Freese, K., J. A. Frieman, and A. V. Olinto. "Natural inflation with pseudo Nambu-Goldstone bosons." *Phys. Rev. Lett.* 65: (1990) 3233–3236. `https://link.aps.org/doi/10.1103/PhysRevLett.65.3233`.

[82] Freese, K., and W. H. Kinney. "Natural Inflation: Consistency with Cosmic Microwave Background Observations of Planck and BICEP2." *JCAP* 1503: (2015) 044.

[83] Friedman, A. "On the Curvature of Space." *General Relativity and Gravitation* 31, 12: (1999) 1991–2000. `http://dx.doi.org/10.1023/A:1026751225741`.

[84] Friedman, A. "On the Possibility of a World wih Constant Negative Curvature of Space." *General Relativity and Gravitation* 31: (1999) 31–2009.

[85] Frieman, J. A., C. T. Hill, A. Stebbins, and I. Waga. "Cosmology with ultralight pseudo Nambu-Goldstone bosons." *Phys. Rev. Lett.* 75: (1995) 2077–2080.

[86] Fujii, Y. "Origin of the gravitational constant and particle masses in a scale-invariant scalar-tensor theory." *Phys. Rev. D* 26: (1982) 2580–2588.

[87] Galli, S., A. Melchiorri, G. F. Smoot, and O. Zahn. "From Cavendish to PLANCK: Constraining Newton's Gravitational Constant with CMB Temperature and Polarization Anisotropy." *Phys. Rev.* D80: (2009) 023 508.

[88] Gelfand, A. E., and A. F. Smith. "Sampling-based approaches to calculating marginal densities." *Journal of the American statistical association* 85, 410: (1990) 398–409.

[89] Gerke, B. F., and G. Efstathiou. "Probing quintessence: Reconstruction and parameter estimation from supernovae." *MNRAS* 335: (2002) 33.

[90] GhahraIllani, Z., and M. J. Beal. "Propagation algorithms for variational Bayesian learning." .

[91] Giostri, R., et al. "From cosmic deceleration to acceleration: new constraints from SN Ia and BAO/CMB." *JCAP* 3: 027.

[92] Gleyzes, J., D. Langlois, and F. Vernizzi. "A unifying description of dark energy." *Int. J. Mod. Phys.* D23: (2014) 3010.

[93] Gubitosi, G., F. Piazza, and F. Vernizzi. "The Effective Field Theory of Dark Energy." *JCAP* 1302: (2013) 032.

[94] Guth, A. H. "Inflationary universe: A possible solution to the horizon and flatness problems." *Phys. Rev. D* 23: (1981) 347–356.

[95] Hall, A., C. Bonvin, and A. Challinor. "Testing General Relativity with 21-cm intensity mapping." *Phys. Rev.* D87, 6: (2013) 064 026.

[96] Harko, T., T. S. Koivisto, F. S. N. Lobo, and G. J. Olmo. "Metric-Palatini gravity unifying local constraints and late-time cosmic acceleration." *Phys. Rev.* D85: (2012) 084 016.

[97] Hlozek, R., D. Grin, D. J. E. Marsh, and P. G. Ferreira. "A search for ultralight axions using precision cosmological data." *Phys. Rev.* D91, 10: (2015) 103 512.

[98] Hojjati, A., L. Pogosian, and G.-B. Zhao. "Testing gravity with CAMB and CosmoMC." *JCAP* 1108: (2011) 005.

[99] Holmes, C. "Markov Chain Monte Carlo and Applied Bayesian Statistics: a short course." *Oxford Centre for Gene Function (2008)* `http://www.stats.ox.ac.uk/~cholmes/Courses/BDA/bda_mcmc.pdf`.

[100] Holz, D. E., and S. A. Hughes. "Using gravitational-wave standard sirens." *Astrophys. J.* 629: (2005) 15–22.

[101] Horndeski, G. W. "Second-order scalar-tensor field equations in a four-dimensional space." *Int. J. Theor. Phys.* 10: (1974) 363–384.

[102] Hotchkiss, S. "Private communication.", (2016).

[103] Hotchkiss, S., A. Mazumdar, and S. Nadathur. "Observable gravitational waves from inflation with small field excursions." *JCAP* 1202: (2012) 008.

[104] Hu, B., M. Raveri, N. Frusciante, and A. Silvestri. "EFTCAMB/EFTCosmoMC: Numerical Notes v2.0.", arXiv e-prints (2014), arXiv: 1405.3590.

[105] Hu, W., and I. Sawicki. "A Parameterized Post-Friedmann Framework for Modified Gravity." *Phys. Rev.* D76: (2007) 104,043.

[106] Hu, W., and N. Sugiyama. "Small scale cosmological perturbations: An Analytic approach." *Astrophys. J.* 471: (1996) 542–570.

[107] Hubble, E. "A relation between distance and radial velocity among extra-galactic nebulae." *Proc. Natl. Acad. Sci. USA* 15: (1929) 168–173.

[108] Jaime, L., M. Salgado, and L. Patino. "Cosmology in {(R) exponential gravity." *Springer Proc. Phys.* 157: (2014) 363–371.

[109] Jain, B., and J. VanderPlas. "Tests of Modified Gravity with Dwarf Galaxies." *JCAP* 1110: (2011) 032.

[110] Jha, S. "Ph.D. thesis, Harvard Univ. CAMBRIDGE, MA.", (2002).

[111] Jha, S., A. G. Riess, and R. P. Kirshner. "Improved Distances to Type Ia Supernovae with Multicolor Light Curve Shapes: MLCS2k2." *Astrophys. J.* 659: (2007) 122–148.

[112] Jordan, M. I., Z. Ghahramani, T. S. Jaakkola, and L. K. Saul. "An introduction to variational methods for graphical models." *Machine learning* 37, 2: (1999) 183–233.

[113] Joyce, A., L. Lombriser, and F. Schmidt. "Dark Energy vs. Modified Gravity." *Ann. Rev. Nucl. Part. Sci.* 66: (2016) 95–122.

[114] Kachru, S., R. Kallosh, A. D. Linde, and S. P. Trivedi. "De Sitter vacua in string theory." *Phys. Rev.* D68: (2003) 046 005.

[115] Kalirai, J. S., et al. "Ultra-Deep Hubble Space Telescope Imaging of the Small Magellanic Cloud: The Initial Mass Function of Stars with M < 1 Msun." *Astrophys. J.* 763: (2013) 110.

[116] Kamionkowski, M., and A. Kosowsky. "Detectability of inflationary gravitational waves with microwave background polarization." *Phys. Rev. D* 57: (1998) 685–691.

[117] Kawasaki, M., T. Moroi, and T. Takahashi. "Cosmic microwave background anisotropy with cosine type quintessence." *Phys. Rev.* D64: (2001) 083 009.

[118] Kazanas, D. "Dynamics of the Universe and Spontaneous Symmetry Breaking." *Astrophys. J.* 241: (1980) L59–L63.

[119] Khoury, J., and A. Weltman. "Chameleon cosmology." *Physical Review D* 69, 4: 044026.

[120] ———. “Chameleon Fields: Awaiting Surprises for Tests of Gravity in Space.” *Physical Review Letters* 93, 17: 171104.

[121] Knox, L., and Y.-S. Song. “A Limit on the detectability of the energy scale of inflation.” *Phys. Rev. Lett.* 89: (2002) 011 303.

[122] Kofman, L., A. D. Linde, and A. A. Starobinsky. “Reheating after inflation.” *Phys. Rev. Lett.* 73: (1994) 3195–3198.

[123] Kofman, L. A. “The Origin of matter in the universe: Reheating after inflation.” 1996. `http://alice.cern.ch/format/showfull?sysnb=0225922`.

[124] Kohri, K., Y. Oyama, T. Sekiguchi, and T. Takahashi. “Elucidating Dark Energy with Future 21 cm Observations.”, arXiv e-prints (2016), arXiv: 1608.01601.

[125] Koivisto, T. S., and N. Tamanini. “Ghosts in pure and hybrid formalisms of gravity theories: A unified analysis.” *Phys. Rev.* D87, 10: (2013) 104 030.

[126] Koksma, J. F., and T. Prokopec. “The Cosmological Constant and Lorentz Invariance of the Vacuum State.” *ArXiv e-prints* .

[127] Komatsu, E., et al. “Five-Year Wilkinson Microwave Anisotropy Probe (WMAP) Observations: Cosmological Interpretation.” *The Astrophysical Journal Supplement* 180: (2009) 330–376.

[128] ———. “Seven-year Wilkinson Microwave Anisotropy Probe (WMAP) Observations: Cosmological Interpretation.” *The Astrophysical Journal Supplement* 192: 18.

[129] Koyama, K. “Cosmological Tests of Modified Gravity.” *Rept. Prog. Phys.* 79, 4: (2016) 046 902.

[130] Krisciunas, K. “The Usefulness of Type Ia Supernovae for Cosmology - A Personal Review.” *Journal of the American Association of Variable Star Observers (JAAVSO)* 40: (2012) 334.

[131] Labini, F. S., N. L. Vasilyev, L. Pietronero, and Y. V. Baryshev. “Absence of self-averaging and of homogeneity in the large scale galaxy distribution.” *Europhys. Lett.* 86, 4: (2009) 49 001.

[132] Laureijs, R., et al. “Euclid Definition Study Report.”, arXiv e-prints (2011), arXiv: 1110.3193.

[133] Lewis, A., and S. Bridle. “Cosmological parameters from CMB and other data: A Monte Carlo approach.” *Phys. Rev.* D66: (2002) 103 511.

[134] Lewis, A., A. Challinor, and A. Lasenby. “Efficient computation of CMB anisotropies in closed FRW models.” *Astrophys. J.* 538: (2000) 473–476.

[135] Lewis, A., A. Challinor, and N. Turok. "Detecting magnetic CMB polarization on an incomplete sky." .

[136] Liddle, A. R., P. Parsons, and J. D. Barrow. "Formalizing the slow roll approximation in inflation." *Phys. Rev.* D50: (1994) 7222–7232.

[137] Lima, N. A., and V. S. Barreto. "Constraints on Hybrid Metric-palatini Gravity from Background Evolution." *Astrophys. J.* 818, 2: (2016) 186.

[138] Lima, N. A. "Dynamics of Linear Perturbations in the hybrid metric-Palatini gravity." *Phys. Rev.* D89, 8: (2014) 083 527.

[139] Lima, N. A., V. Smer-Barreto, and L. Lombriser. "Constraints on decaying early modified gravity from cosmological observations." *Phys. Rev.* D94, 8: (2016) 083 507.

[140] Linde, A. "A new inflationary universe scenario: A possible solution of the horizon, flatness, homogeneity, isotropy and primordial monopole problems." *Physics Letters B* 108, 6: (1982) 389 – 393.

[141] ———. "Eternally existing self-reproducing chaotic inflanationary universe." *Physics Letters B* 175, 4: (1986) 395 – 400.

[142] Linde, A. D. "Recent progress in inflationary cosmology." In *Cosmological constant and the evolution of the universe. Proceedings, 1st RESCEU International Symposium, Tokyo, Japan, November 7-10, 1995.* 1995, 133–148.

[143] Linder, E. V., and D. Huterer. "How many dark energy parameters?" *Phys. Rev.* D72: (2005) 043 509.

[144] Link, W. A., and M. J. Eaton. "On thinning of chains in MCMC." *Methods in Ecology and Evolution* 3, 1: (2012) 112–115. `http://dx.doi.org/10.1111/j.2041-210X.2011.00131.x`.

[145] Lobo, F. S. N. "The Dark side of gravity: Modified theories of gravity." 173-204: (2009) Research Signpost, ISBN 978–81–308–0341–8.

[146] Lombriser, L. "Consistency check of ΛCDM phenomenology." *Phys. Rev.* D83: (2011) 063 519.

[147] ———. "Constraining chameleon models with cosmology." *Annalen Phys.* 526: (2014) 259–282.

[148] Lombriser, L., and N. A. Lima. "Challenges to Self-Acceleration in Modified Gravity.", arXiv e-prints (2016), arXiv: 1602.07670.

[149] Lombriser, L., F. Simpson, and A. Mead. "Unscreening Modified Gravity in the Matter Power Spectrum." *Phys. Rev. Lett.* 114, 25: (2015) 251 101.

[150] Lombriser, L., and A. Taylor. "Classifying Linearly Shielded Modified Gravity Models in Effective Field Theory." *Phys. Rev. Lett.* 114, 3: (2015) 031101.

[151] ———. "Semi-dynamical perturbations of unified dark energy." *JCAP* 1511, 11: (2015) 040.

[152] ———. "Breaking a dark degeneracy with gravitational waves." *JCAP* 1603: (2016) 031.

[153] Lovelock, D. "The Einstein tensor and its generalizations." *J. Math. Phys.* 12: (1971) 498–501.

[154] ———. "The four-dimensionality of space and the einstein tensor." *J. Math. Phys.* 13: (1972) 874–876.

[155] Lyth, D., and A. Liddle. *The primordial density perturbation.* Cambridge University Press, Cambridge, U.K., 2009.

[156] Lyth, D. H. "What would we learn by detecting a gravitational wave signal in the cosmic microwave background anisotropy?" *Phys. Rev. Lett.* 78: (1997) 1861–1863.

[157] ———. "The gravitino abundance in supersymmetric 'new' inflation models." *Physics Letters B* 488, 34: (2000) 417 – 422.

[158] Ma, C.-P., and E. Bertschinger. "Cosmological Perturbation Theory in the Synchronous vs. Conformal Newtonian Gauge." *ArXiv Astrophysics e-prints* .

[159] MacKay, D. J. C. *Information Theory, Inference & Learning Algorithms.* New York, NY, USA: Cambridge University Press, 2002.

[160] Madau, P., A. Meiksin, and M. J. Rees. "21 Centimeter Tomography of the Intergalactic Medium at High Redshift." *ApJ* 475: (1997) 429–444.

[161] Mather, J. C., et al. "A preliminary measurement of the cosmic microwave background spectrum by the Cosmic Background Explorer (COBE) satellite." *Astrophysical Journal, Part 2 - Letters* 354: (1990) L37–L40.

[162] Minh, D. D. L., D. Le, and Minh. "Understanding the Hastings Algorithm.", arXiv e-prints (2014), arXiv: 1408.4438.

[163] Minka, T. P. "Expectation propagation for approximate Bayesian inference." In *Proceedings of the Seventeenth conference on Uncertainty in artificial intelligence.* Morgan Kaufmann Publishers Inc., 2001, 362–369.

[164] Mukherjee, P., D. Parkinson, and A. R. Liddle. "A nested sampling algorithm for cosmological model selection." *The Astrophysical Journal Letters* 638, 2: (2006) L51.

[165] Ng, S. C. C., and D. L. Wiltshire. “Properties of cosmologies with dynamical pseudo Nambu-Goldstone bosons.” *Phys. Rev.* D63: (2001) 023 503.

[166] Nicolis, A., R. Rattazzi, and E. Trincherini. “The Galileon as a local modification of gravity.” *Phys. Rev.* D79: (2009) 064 036.

[167] Nojiri, S., and S. D. Odintsov. “Dark energy, inflation and dark matter from modified F(R) gravity.” *TSPU Bulletin* N8(110): (2011) 7–19.

[168] Okada, N., M. U. Rehman, and Q. Shafi. “Non-Minimal B-L Inflation with Observable Gravity Waves.” *Phys. Lett.* B701: (2011) 520–525.

[169] Olmo, G. J. “Post-Newtonian constraints on f(R) cosmologies in Palatini formalism.” *ArXiv General Relativity and Quantum Cosmology e-prints* .

[170] Opper, M., and D. Saad. *Advanced mean field methods: Theory and practice.* MIT press, 2001.

[171] Padmanabhan, N., et al. “A 2 per cent distance to z = 0.35 by reconstructing baryon acoustic oscillations - I. Methods and application to the Sloan Digital Sky Survey.” *MNRAS* 427: (2012) 2132–2145.

[172] Penzias, A. A., and R. W. Wilson. “A Measurement of Excess Antenna Temperature at 4080 Mc/s.” *ApJ* 142: (1965) 419–421.

[173] Percival, W. J., et al. “Baryon acoustic oscillations in the Sloan Digital Sky Survey Data Release 7 galaxy sample.” *MNRAS* 401: (2010) 2148–2168.

[174] Perivolaropoulos, L. “PPN Parameter gamma and Solar System Constraints of Massive Brans-Dicke Theories.” *Phys. Rev.* D81: (2010) 047,501.

[175] Perlmutter, S., et al. “Measurements of Omega and Lambda from 42 high redshift supernovae.” *Astrophys. J.* 517: (1999) 565–586.

[176] Phillips, M. M. “The absolute magnitudes of Type IA supernovae.” *Astrophysical Journal* 413: (1993) L105–L108.

[177] ———. “Near-Infrared Properties of Type Ia Supernovae.” *PASA* 29: (2012) 434–446.

[178] Pogosian, L., and A. Silvestri. “The pattern of growth in viable f(R) cosmologies.” *Phys. Rev.* D77: (2008) 023 503.

[179] Prat, J., et al. “Galaxy bias from galaxy-galaxy lensing in the DES Science Verification Data.”, arXiv e-prints (2016), arXiv: 1609.08167.

[180] Rakhi, R., and K. Indulekha. “Dark Energy and Tracker Solution-A Review.” *arXiv preprint arXiv:0910.5406* .

[181] Ratra, B., and P. J. E. Peebles. “Cosmological consequences of a rolling homogeneous scalar field.” *Phys. Rev. D* 37: (1988) 3406–3427.

[182] Rehman, M. U., Q. Shafi, and J. R. Wickman. "Observable Gravity Waves from Supersymmetric Hybrid Inflation II." *Phys. Rev.* D83: (2011) 067 304.

[183] Riess, A. G., et al. "Observational evidence from supernovae for an accelerating universe and a cosmological constant." *Astron. J.* 116: (1998) 1009–1038.

[184] ———. "A 3% Solution: Determination of the Hubble Constant with the Hubble Space Telescope and Wide Field Camera 3." *Astrophys. J.* 730: (2011) 119.

[185] Ross, A. J., et al. "The clustering of the SDSS DR7 main Galaxy sample I. A 4 per cent distance measure at $z = 0.15$." *MNRAS* 449, 1: (2015) 835–847.

[186] Sachs, R. K., and A. M. Wolfe. "Perturbations of a cosmological model and angular variations of the microwave background." *Astrophys. J.* 147: (1967) 73–90.

[187] Sahni, V., and Y. Shtanov. "Brane world models of dark energy." *JCAP* 0311: (2003) 014.

[188] Sami, M. "A Primer on problems and prospects of dark energy." *Curr. Sci.* 97: (2009) 887.

[189] Sanghai, V. A. A., and T. Clifton. "Parameterized Post-Newtonian Cosmology.", arXiv e-prints (2016), arXiv: 1610.08039.

[190] Santos, M. G., et al. "Cosmology with a SKA HI intensity mapping survey." .

[191] Sato, K. "First-order phase transition of a vacuum and the expansion of the Universe." *MNRAS* 195: (1981) 467–479.

[192] Sato, K. "Cosmological baryon-number domain structure and the first order phase transition of a vacuum." *Physics Letters B* 99, 1: (1981) 66 – 70.

[193] Scherrer, R. J., and A. A. Sen. "Thawing quintessence with a nearly flat potential." *Phys. Rev.* D77: (2008) 083 515.

[194] Schmidt, H.-J. "Fourth order gravity: Equations, history, and applications to cosmology." *eConf* C0602061: (2006) 12.

[195] Schutz, B. F. "Determining the Hubble Constant from Gravitational Wave Observations." *Nature* 323: (1986) 310–311.

[196] Scrimgeour, M., et al. "The WiggleZ Dark Energy Survey: the transition to large-scale cosmic homogeneity." *MNRAS* 425: (2012) 116–134.

[197] Shafi, Q., and J. R. Wickman. "Observable Gravity Waves From Supersymmetric Hybrid Inflation." *Phys. Lett.* B696: (2011) 438–446.

[198] Shapiro, I. I. “Fourth Test of General Relativity.” *Phys. Rev. Lett.* 13: (1964) 789–791.

[199] Shapiro, S. S., J. L. Davis, D. E. Lebach, and J. S. Gregory. “Measurement of the Solar gravitational Deflection of Radio Waves using Geodetic Very-Long-Baseline Interferometry Data, 1979˘1999.” *Phys. Rev. Lett.* 92: (2004) 121 101.

[200] Shaw, J. R., M. Bridges, and M. P. Hobson. “Efficient Bayesian inference for multimodal problems in cosmology.” *Monthly Notices of the Royal Astronomical Society* 378, 4: (2007) 1365–1370. `http://dx.doi.org/10.1111/j.1365-2966.2007.11871.x`.

[201] Shtanov, Y., J. H. Traschen, and R. H. Brandenberger. “Universe reheating after inflation.” *Phys. Rev.* D51: (1995) 5438–5455.

[202] de Sitter, W. “On Einstein’s Theory of Gravitation and its Astronomical Consequences. Third Paper.” *Monthly Notices of the Royal Astronomical Society* 78, 1: (1917) 3–28.

[203] Skilling, J., et al. “Nested sampling for general Bayesian computation.” *Bayesian analysis* 1, 4: (2006) 833–859.

[204] Skordis, C., A. Pourtsidou, and E. J. Copeland. “Parametrized post-Friedmannian framework for interacting dark energy theories.” *Phys. Rev. D* 91: (2015) 083 537.

[205] Smer-Barreto, V., and A. R. Liddle. “Planck Satellite Constraints on Pseudo-Nambu–Goldstone Boson Quintessence.” *JCAP* 1701, 01: (2017) 023.

[206] Sotiriou, T. P. “The Significance of matter coupling in f(R) gravity.” In *Recent developments in theoretical and experimental general relativity, gravitation and relativistic field theories. Proceedings, 11th Marcel Grossmann Meeting, MG11, Berlin, Germany, July 23-29, 2006. Pt. A-C.* 2006, 1223–1225.

[207] Sotiriou, T. P., and V. Faraoni. “f(R) Theories Of Gravity.” *Rev. Mod. Phys.* 82: (2010) 451–497.

[208] Spergel, D. N., et al. “First-Year Wilkinson Microwave Anisotropy Probe (WMAP) Observations: Determination of Cosmological Parameters.” *The Astrophysical Journal Supplement* 148: (2003) 175–194.

[209] ———. “Three-Year Wilkinson Microwave Anisotropy Probe (WMAP) Observations: Implications for Cosmology.” *The Astrophysical Journal Supplement* 170: (2007) 377–408.

[210] Starobinsky, A. A. “A New Type of Isotropic Cosmological Models Without Singularity.” *Phys. Lett.* B91: (1980) 99–102.

[211] ———. “Disappearing cosmological constant in f(R) gravity.” *JETP Lett.* 86: (2007) 157–163.

[212] Steinhardt, P. J., L.-M. Wang, and I. Zlatev. “Cosmological tracking solutions.” *Phys. Rev.* D59: (1999) 123 504.

[213] Stewart, E. D., and D. H. Lyth. “A More accurate analytic calculation of the spectrum of cosmological perturbations produced during inflation.” *Phys. Lett.* B302: (1993) 171–175.

[214] Sullivan, M., et al. “SNLS3: Constraints on Dark Energy Combining the Supernova Legacy Survey Three-year Data with Other Probes.” *ApJ* 737: 102.

[215] Susskind, L. “The Anthropic landscape of string theory.”, arXiv e-prints (2003), arXiv: 0302219.

[216] Suzuki, N., et al. “The Hubble Space Telescope Cluster Supernova Survey. V. Improving the Dark-energy Constraints above $z > 1$ and Building an Early-type-hosted Supernova Sample.” *ApJ* 746: 85.

[217] Tamanini, N., et al. “Science with the space-based interferometer eLISA. III: Probing the expansion of the Universe using gravitational wave standard sirens.” *JCAP* 1604, 04: (2016) 002.

[218] Tsujikawa, S. “Quintessence: A Review.” *Class. Quant. Grav.* 30: (2013) 214 003.

[219] Umezu, K.-i., K. Ichiki, and M. Yahiro. “Cosmological constraints on Newton’s constant.” *Phys. Rev.* D72: (2005) 044 010.

[220] Wainwright, M., and M. Jordan. “Graphical models, exponential families, and variational inference. UC Berkeley, Dept.” Technical report, of Statistics, Technical Report 649, 2003.

[221] Wang, P.-Y., C.-W. Chen, and P. Chen. “Confronting tracker field quintessence with data.” *JCAP* 2012, 02: (2012) 016.

[222] Wang, Y., and P. Mukherjee. “Observational Constraints on Dark Energy and Cosmic Curvature.” *Phys. Rev.* D76: (2007) 103 533.

[223] Wang, Y., and S. Wang. “Distance Priors from Planck and Dark Energy Constraints from Current Data.” *Phys. Rev.* D88, 4: (2013) 043 522.

[224] Wetterich, C. “Cosmology and the fate of dilatation symmetry.” *Nuclear Physics B* 302, 4: (1988) 668 – 696.

[225] Wiegerinck, W. “Variational approximations between mean field theory and the junction tree algorithm.” In *Proceedings of the Sixteenth conference on Uncertainty in artificial intelligence.* Morgan Kaufmann Publishers Inc., 2000, 626–633.

[226] York, D. G., et al. "The Sloan Digital Sky Survey: Technical Summary." *Astron. J.* 120: (2000) 1579–1587.

[227] Zaldarriaga, M., and U. c. v. Seljak. "Gravitational lensing effect on cosmic microwave background polarization." *Phys. Rev.* D58: (1998) 023 003.

[228] Zlatev, I., L. Wang, and P. J. Steinhardt. "Quintessence, Cosmic Coincidence, and the Cosmological Constant." *Phys. Rev. Lett.* 82: (1999) 896–899.